Università degli Studi di Milano - Bicocca
Facoltà di Scienze Matematiche, Fisiche e Naturali
Corso di dottorato di Ricerca in Fisica e Astronomia

XXIII Ciclo, A.A. 2008 – 2010

A Thesis submitted for the degree of
Dottore di Ricerca in Fisica

Development of cryogenic detectors for rare event searches

Luca Gironi
Matricola 033675

Advisor
Prof. Oliviero Cremonesi

School Coordinator
Prof. Claudio Destri

Contents

To Magda

Introduction

The experimental evidence of neutrino oscillations clearly showed that the neutrino is a finite-mass particle. Anyway, two big questions concerning the neutrino are still unsolved: its nature (Dirac or Majorana) and the absolute value of its mass. The Double Beta Decay without emission of neutrinos (0νDBD) is at present the most sensitive method to answer the two questions. Bolometers, together with germanium diodes, have provided so far the best results within this kind of research. The choice of the so-called calorimetric approach, where the detector is made of the 0νDBD material, allows the study of large quantities of isotope with an excellent energy resolution (around 0.2-0.3 %). Both features are crucial to disentangle the searched peak from background. The Cuoricino experiment, in which 62 detectors of tellurium dioxide (TeO_2) were involved, was carried out in hall A at Laboratori Nazionali del Gran Sasso (LNGS), and represented the bolometric experiment with the best sensitivity concerning the study on the 0νDBD decay. The knowledge achieved in the bolometric technique and its excellent results on 0νDBD led to the development of new experiments to study rare events with bolometric technique. The CUORE (Cryogenic Underground Observatory for Rare Events) experiment, composed by 988 bolometric detectors of TeO_2, is under construction and foresees a sensitivity on neutrino mass of the order of about 50 meV. This high sensitivity requires excellent energetic resolutions, low number of spurious counts within the region of interest and high quantity of the 0νDBD active isotope. The reduction of the background in the energetic window where the 0νDBD for the isotope ^{130}Te is expected ($Q_{\beta\beta} = 2527$ keV) plays a primary role.

In this context, the activities I have done are focused primarily on the analysis of the different contributions to the background of CUORE and the optimization of methods for its reduction. This work has been done both through measurements performed in the hall C of LNGS and with Monte Carlo simulations that allowed data interpretation and assessment of the resulting sensitivity. For example, through a series of simulations performed with GEANT4 code it is possible to extrapolate the background induced by muons in CUORE. The results of simulations were then validated through the installation of a muon veto above Cuoricino which allowed a direct comparison with experimental measurement.

For what concerns the reduction of the bolometers specific background I have also

done some measurements for the development, characterization and optimization of some scintillating bolometers. These detectors, thanks to double read-out of thermal and scintillation signals, allow to discriminate different ionizing particles (β/γ, α and neutrons). This allows a significant reduction of the unwanted background in the region of interest and would therefore allow to approach the condition of 'zero background' experiments. Indeed, thanks to the wide choice for the absorber material that allows to study practically all 0νDBD candidate isotopes, it is possible to choose an isotope with a transition energy above 2615 keV and then remove, in practice, all the background due to γ rays. The 2615 keV γ line corresponds in fact to the highest energy γ-ray line from natural radioactivity and is due to ^{208}Tl. Above this energy there are only extremely rare high energy γ's. Once γ-rays are no more a worrisome source of background, what is left on the side of radioactivity are α emissions. Indeed α surface contaminations are already recognized as the most relevant background source in the bolometric experiment Cuoricino. However, thanks to the double read-out of scintillating bolometers, this source of background can be removed too. During my PhD I have tested a number of different crystals and with some of them ($CdWO_4$, ZnSe and some molybdates) I have obtained excellent results both from the point of view of the detector performance and the reduction of the background contributions. Thanks to these results it was possible to evaluate the discrimination power (i.e. the capability to recognize and reject unwanted events) of this technique and extrapolate the sensitivity of a large mass experiment for 0νDBD based on the hybrid heat plus scintillation technique.

Moreover, during the analysis of the data collected with the scintillating bolometers, I recognized for the first time, a dependence of the pulse shapes (both on the scintillation and heat channels) on the interacting particle nature. I proposed then to exploit such wonderful feature to discriminate the interacting particles without relying on the much more complicated measurement of both (light and heat) signals. This feature is very promising because it allows to greatly reduce the background in bolometers without getting complicated the assembly of the experiment. In fact in the case of the double read-out of temperature and scintillation both light detectors and reflecting sheet (used to properly collect the scintillation light) are needed in addition to the low temperature calorimeter.

Finally, I have proposed a further use of the scintillating bolometer for diagnostic purposes, i.e. the possibility to study surface contaminations with high sensitivity. One of the main limitations in our understanding of the background due to surface contaminations is in fact related to the limited sensitivity of the available standard techniques. Traditionally the devices used in this field are Si surface barrier detectors with an active area of about 10 cm^2, a typical energy resolution of about 25-30 keV FWHM, and counting rates of the order 0.05 count/h/cm^2 between 3 and 8 MeV. A Cuoricino-like bolometer can easily reach a much larger active area (150 cm^2) and, thanks to the absence of a dead layer can reach resolution on surface α particles of 10 keV. Moreover a background counting rate in the 3-8

MeV region as low as 0.001 count/h/cm^2 was already reached with this technique. This considerations allow to plan measurements with sensitivities order of magnitude better than standard devices.

However, in order to use scintillating bolometer to study surface contaminations, they have not to be surrounded by a reflecting sheet. For these reason it is necessary to use crystals with a very high light yield or crystals that are able to recognize particle from the shape of the thermal pulses (i.e. without any need of collecting the scintillation light). Since this last feature is a very recent discovery and some works have still to be performed before the technique can be considered actually at hand, I have proposed to use a BGO crystal ($Bi_4Ge_3O_{12}$), which is characterized by a very high light yield, to study surface contaminations. Preliminary tests with an array of 4 'small' crystals (2x2x2 cm^3) have shown how this possibility could be fulfilled. However this measurement showed a very slow cooling down and an high counting rate due to ^{207}Bi. Therefore, before using the crystal to study surface contamination, a new measurement was carried out with a larger crystal (5x5x5 cm^3). The measurement was successful and showed that the slow cool down and the high counting rate are not intrinsic problems of these crystals. This first test gave excellent results on surface studies and, as supplementary results, a measurement of the rare α decay of ^{209}Bi with a high statistical significance was performed.

Part I

Theoretical Overview

Chapter 1

The massive neutrino

Since the first evidence in the 1960's, many experiments have provided compelling evidence for neutrino oscillations from one flavour to another in neutrinos originating from different sources like the sun, the atmosphere, nuclear reactors and particle accelerators [1]. Neutrino oscillations imply that neutrinos have mass, and prompted by this discovery, the question of whether neutrinos are Dirac or Majorana particles has become one of the issues at the forefront of particle and nuclear physics. At present, neutrinoless Double Beta Decay (0νDBD) is the most sensitive method to answer this question and to evaluate the absolute value of its mass.

In this chapter, after a short overview of oscillation results, direct measurements of neutrino masses and a possible mechanism for the generation of neutrino masses will be presented. 0νDBD will be presented in detail in Chapter 2.

1.1 Neutrino history

The existence of an electrically neutral half-spin particle was postulated by W. Pauli in 1930, as a "desperate remedy" to save the principle of energy conservation in beta decay. It was E. Fermi in 1934 [2] who named this particle 'neutrino', within the formulation of his theory for beta decay. In 1959 neutrinos were detected for the first time by F. Reines and C. Cowan [3], observing the inverse beta decay produced by anti-neutrino interactions. In 1962 muon neutrinos were discovered by L.M. Lederman, M. Schwartz and collaborators at Brookhaven National Laboratories [4]. The first direct detection of the tau neutrino was obtained by the DONUT experiment in 2000 [5].

As electrically neutral leptons, neutrinos only participate in the weak interactions. Compared to other known particles they have a much smaller probability of interacting

with matter. For this reason neutrino detection has always been a challenging task. Despite the experimental difficulties, neutrino physics has attracted growing attention. Indeed, through the study of this particle it is possible to obtain plenty of information in different research fields.

Great interest in neutrino physics was raised by the discovery of lepton flavor non conservation. The first hints for this phenomenon date back to the late 1960's, when a deficit in the solar neutrino flux was observed [6]. It took about thirty years to completely understand the problem. At present many experimental checks have lead to the conclusion that this phenomenon can be described by neutrino oscillations, initially proposed by Bruno Pontecorvo in 1957.

1.2 Neutrino oscillations

If neutrino has a nonzero rest mass, mass eigenstates and weak interactions eigenstates do not necessarily have to coincide. In practice, the flavor eigenstates (ν_e, ν_μ, ν_τ) are related to mass eigenstates (ν_1, ν_2, ν_3) by

$$\nu_l = \sum_i U_{li}\nu_i \qquad\qquad l = e, \mu, \tau \quad i = 1, 2, 3 \tag{1.1}$$

where the matrix U_{li} is called Pontecorvo-Maki-Nakagawa-Sakata (PMNS) matrix [7], a mixing matrix analogue of the Cabibbo-Kobayashi-Maskawa (CKM) matrix for quarks. By treating the simplest case with mixing of only two neutrinos (ν_α, ν_β) and (ν_1, ν_2) the relationship between neutrino states is described by a single mixing angle θ and the unitary matrix U_{li} can be parameterized as follows:

$$U = \begin{pmatrix} \cos\theta & \sin\theta \\ -\sin\theta & \cos\theta \end{pmatrix} \tag{1.2}$$

In this case the probability of a transition between the flavour α and the flavour β at a distance L from the point at which the α flavour neutrino was produced is:

$$P_{\nu_\alpha \longrightarrow \nu_\beta}(L, E) = \sin^2 2\theta \ \ \sin^2\left(\frac{\Delta m^2_{12}\ L}{4\ E}\right) \tag{1.3}$$

where E is the energy of the neutrino and $\Delta m^2_{12} = m^2_2 - m^2_1$. From this formula we see explicitly that oscillations can only occur if θ is not zero and masses are different from each other ($\Delta m^2_{12} \neq 0$).

In the more complex case with three neutrinos the PMNS matrix is usually indicated by the Chau and Keung parametrization [8]

$$\begin{pmatrix} \nu_e \\ \nu_\mu \\ \nu_\tau \end{pmatrix} = U\ V \begin{pmatrix} \nu_1 \\ \nu_2 \\ \nu_3 \end{pmatrix} =$$

$$\begin{pmatrix} c_{12}c_{13} & s_{12}c_{13} & s_{13}e^{-i\delta} \\ -s_{12}c_{23} - c_{12}s_{23}s_{13}e^{i\delta} & c_{12}c_{23} - s_{12}s_{23}s_{13}e^{i\delta} & s_{23}c_{13} \\ s_{12}s_{23} - c_{12}c_{23}s_{13}e^{i\delta} & -c_{12}s_{23} - s_{12}c_{23}s_{13}e^{i\delta} & c_{23}c_{13} \end{pmatrix} \times \tag{1.4}$$

$$\times \begin{pmatrix} 1 & 0 & 0 \\ 0 & e^{i\phi_2/2} & 0 \\ 0 & 0 & e^{i(\phi_3/2+\delta)} \end{pmatrix} \begin{pmatrix} \nu_1 \\ \nu_2 \\ \nu_3 \end{pmatrix}$$

where $c_{ij} \equiv \cos\theta_{ij}$ and $s_{ij} \equiv \sin\theta_{ij}$, θ_{ij} is the mixing angle, δ is the Dirac phase and V is a diagonal matrix containing the Majorana phases (ϕ_2 and ϕ_3) which does not affect the probability of oscillations.

Neutrino oscillations, observed for the first time in measurements of the solar [9] and atmospheric [10] neutrino fluxes showed the existence of two different mass scales. However, from these measurements no information on the absolute value of neutrino masses can be extracted because of the dependence of the oscillation probability from Δm^2. The measurement of the solar neutrino fluxes has determined that the difference between the masses of the two involved mass eigenstates must be of the order of 10^{-5} eV and usually the notation $\Delta m^2_{SUN} = \Delta m^2_{12}$ is used. The study of atmospheric neutrinos has instead highlighted the existence of a mass scale two orders of magnitude larger ($\Delta m^2_{ATM} = \Delta m^2_{23}$). The most recent values [1] of the mixing matrix parameters and the values of Δm^2 are given in table 1.1. They were obtained not only by considering atmospheric (SuperKamiokande and MACRO) and solar (SuperKamiokande, SNO and GALLEX/GNO) experiments but also the reactors (KamLAND and CHOOZ) and accelerators (K2K and NUMI) experiments.

Oscillation parameter	
Solar mass splitting	$\Delta m^2_{12} = (7.58 \pm 0.21)\, 10^{-5} eV^2$
Atmospheric mass splitting	$\lvert\Delta m^2_{23}\rvert = (2.4 \pm 0.15)\ \ 10^{-3}\mathrm{eV}^2$
Solar mixing angle	$\tan^2\theta_{12} = 0.484 \pm 0.048$
atmospheric mixing angle	$\sin^2 2\theta_{23} = 1.02 \pm 0.04$
'CHOOZ' mixing angle	$\sin^2 2\theta_{13} = 0.07 \pm 0.04$

Table 1.1: Summary of current information on neutrino masses and mixing parameters from oscillations data.

The presently available experimental values are compatible with three possible scenarios for the hierarchy of masses:

1. *Normal Hierarchy (NH)*: $\Delta m^2_{23} > 0$, $m_1 < m_2 < m_3$

$$\Delta m^2_{12} \simeq \Delta m^2_{\rm sun} \simeq m_2^2 \quad \Delta m^2_{23} \simeq |\Delta m^2_{\rm atm}| \simeq m_3^2 \tag{1.5}$$

2. *Inverted Hierarchy (IH)*: $\Delta m^2_{23} < 0$, $m_3 < m_1 < m_2$

$$\Delta m^2_{12} \simeq \Delta m^2_{\rm sun} \quad \Delta m^2_{23} \simeq -|\Delta m^2_{\rm atm}| \simeq -\, m_1^2 \tag{1.6}$$

3. *Quasi-Degenerated Hierarchy*: the mass eigenvalues are much larger than the differences among them. In other words, percentage mass differences are negligible

$$|\Delta m^2_{ij}| \ll m_1^2 \simeq m_2^2 \simeq m_3^2 \tag{1.7}$$

Figure 1.1 shows the three possible scenarios for the hierarchy of the masses.

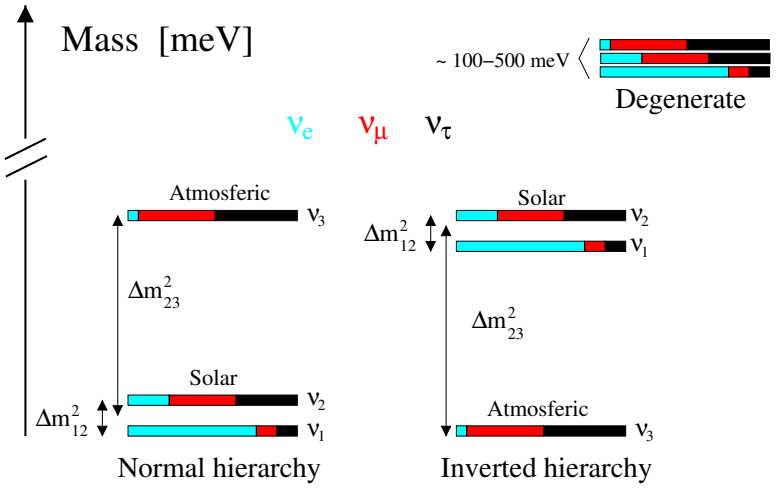

Figure 1.1: Possible configurations for the neutrino mass with the assumption $\Delta m^2_{12} \ll \Delta m^2_{23}$. Colors represent flavor abundances in mass eigenstates.

Thanks to the data from solar, atmospheric, reactor and accelerator experiments, our understanding of neutrino oscillations has incredibly improved in the recent years. However, in order to obtain informations about absolute neutrino masses several non-oscillations experiments were carried out and others are under construction.

1.3 Absolute measurement of neutrino mass

Limits on absolute neutrino masses come from cosmological constraints and from non-oscillation experiments studying single and double beta decay. The discussion here will be limited to cosmological constraints and to single beta decay. 0νDBD will be widely discussed in Chapter 2.

Direct neutrino mass measurements are based on the analysis of the kinematics of charged particles emitted together with neutrinos in weak decays. The most sensitive measurements, involving electron neutrinos, are based on the study of the shape of the β spectrum end-point. β-decay experiments are sensitive to an incoherent combination of the mass eigenvalues, called effective electron neutrino mass m_β and defined as

$$m_\beta^2 = \sum_{i=1}^{3} |U_{ei}|^2 m_i^2 \tag{1.8}$$

The best limits on m_β come from the Mainz [11] and Troitsk [12] tritium β-decay experiments: $m_\beta \lesssim 2.1$ eV. Next generation experiments plain to further constrain m_β in the sub-eV range, using the β-decay of tritium (KATRIN [13]) and ^{187}Re (MARE [14], [15]).

Cosmological constraints on neutrino masses come from the observation of the Cosmic Microwave Background anisotropies and from the study of large scale structures. These observations are sensitive to the sum of the three neutrino masses

$$\sum = m_1 + m_2 + m_3 \tag{1.9}$$

Limits on neutrino masses range from few eV to few hundreds of meV, depending on the data sets that are being considered. However, these constraints are less trustworthy if compared with those obtained in laboratory experiments, as they depend on cosmological models.

1.4 Dirac and Majorana neutrinos

Oscillation experiments and direct search for neutrino mass are not affected by the nature of neutrino. The physics involved in these kinds of measurements is the same, regardless of whether neutrinos are Dirac or Majorana. The most promising approach to discriminate between these two possibilities is to search for neutrinoless Double Beta Decay (0νDBD). One of the key properties of this decay is to contradict the predictions of the Standard Model.

Formulated in the 60's, the Standard Model provides a quantitative description for the weak and electromagnetic interactions of elementary particles and had numerous experimental confirmation of its accuracy. The Standard Model of electroweak interactions describes neutrinos as the left-handed massless particles associated with the three charged leptons (e, μ, τ). While charged leptons are clearly distinct from their antiparticles because they posses opposite electric charge, for neutral particles, the distinction between particles and their antiparticles is not so obvious. In 1937, for the first time the concept of fermions that do not differ from their antiparticles was introduced by Majorana. Because

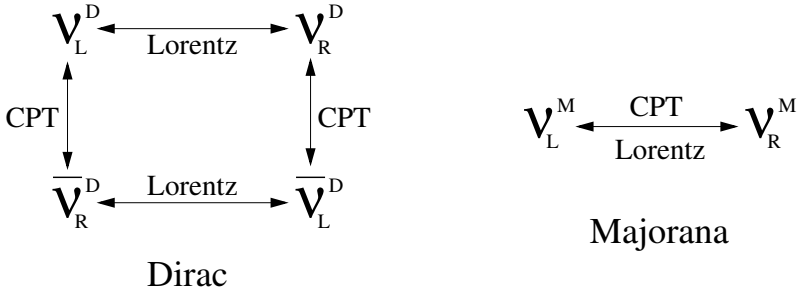

Figure 1.2: Transformation properties for the Dirac and Majorana neutrinos.

of its properties (in particular for having no other conserved charge than lepton number), the neutrino turns out to be the best candidate to be a Majorana particle.

In the Standard Model, Dirac particles are described by a wave function with four independent components (spinors of Dirac) that satisfy the Dirac equation. The four components of the wave function correspond to the particle and its antiparticle, each with two possible helicity. In this scenario, the massive Dirac neutrino then has four different states. If we assume the existence of a massive left-handed neutrino (negative helicity) ν_L and the CPT theorem holds, then there will be also the CPT transform state: a right-handed antineutrino $\overline{\nu_R}$ (see Figure 1.2).

Since we are dealing with the case of massive neutrinos, their speed will be lower than light, and then there will always be a reference system in which the helicity changes sign. Thus if the neutrino has a charge (lepton number) and a mass, it must consists of four different states called a Dirac neutrino. If, on the contrary, the neutrino does not have a charge, only the two helicity states are defined; this is called a Majorana neutrino. Following the V-A structure of the Standard Model, right-handed neutrinos are sterile. Thus, in the Majorana case, only two neutrinos are able to interact. The difference is that in the Standard Model their interaction follows from their charge conservation while in the Majorana case the interaction is governed by the helicity.

The possibility that the neutrino is a Majorana particle is also supported by the theoretical point of view. Indeed, the Dirac theory can't explain why neutrinos and their charged leptons of the same weak doublet have masses that differ by at least five orders of magnitude. This feature is explained rather naturally through the "see-saw mechanism" [16]. In the Majorana case, the neutrino mass (m_ν) naturally satisfies the relation

$$m_\nu M \approx M_{q,\,l}^2 \tag{1.10}$$

where $M_{q,\,l}$ represents the mass of a lepton or a quark, and M is a very large mass. So this model produces a light neutrino for each of the three known neutrino flavors, and a very heavy, undiscovered sterile neutrino.

Chapter 2

Neutrinoless Double Beta Decay

Understanding the nature of the neutrino mass is one of the key topics at the frontier of fundamental physics. Neutrinoless Double Beta Decay (0νDBD) is a powerful tool to investigate the nature of the neutrino (Dirac or Majorana), the absolute value of its mass [17] and possible extensions of the Standard Model.

Since 1950 many experiments have been realized using different techniques and different 0νDBD candidate nuclei. Among them the most promising are those with an active source approach in which the 0νDBD source is part of the detector material (source=detector).

A high-resolution germanium diode was used for the first time to search 0νDBD of ^{76}Ge by Fiorini and colleagues [18] in 1967. They were able to assign a limit to the ^{76}Ge 0νDBD decay mode of $T_{1/2} > 2 \cdot 10^{20}$ years. Many years later part of the Heidelberg-Moscow collaboration claimed a $4.2\,\sigma$ positive hint for the 0νDBD of ^{76}Ge, with $T^{0\nu}_{1/2} = 1.19 \cdot 10^{25}$y. Experiments based on the bolometric technique would confirm or deny this claim searching 0νDBD in other candidates nuclei.

In this chapter I will describe double beta decay processes, isotope features needed to be a good candidate for the 0νDBD and I will conclude with a brief overview on the techniques used to study this process.

2.1 Double Beta Decay

The two-neutrino double beta decay mode (2νDBD) was first proposed in 1935 by Goeppert-Mayer [19]. It is expected to occur in the Standard Model as a second order effect of the well known beta decay Hamiltonian, and it imposes no special requirements on neutrino properties. It will occur irrespective of whether the neutrino is a Majorana or a Dirac particle and irrespective of whether it has a mass or not. The possible 2ν decay modes are:

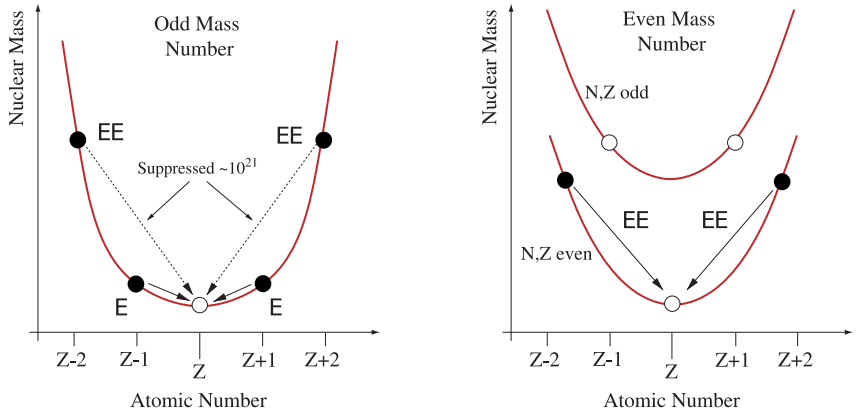

Figure 2.1: Schematic picture of the atomic mass as a function of Z for isobar multiplets with odd A (left) and even A (right).

$$\begin{aligned}
&(A,Z) \rightarrow (A,Z+2) + 2e + 2\overline{\nu}_e && \beta\beta^- \\
&(A,Z) \rightarrow (A,Z-2) + 2e^+ + 2\nu_e && \beta\beta^+ \\
&(A,Z) + 2e^- \rightarrow (A,Z-2) + 2\nu_e && ECEC \\
&(A,Z) + e^- \rightarrow (A,Z-2) + e^+ + 2\nu_e && EC\beta^+
\end{aligned} \tag{2.1}$$

Nuclear transitions accompanied by positron emission or electron capture processes are, however, characterized by poorer experimental sensitivities and will not be discussed in the following. The first process of Equation 2.1 represents the analogue of the single beta decay mediated by the weak current in which a d quark transforms into an u with the emission of an e^- and an $\overline{\nu}_e$. Using simple dimensional arguments it is straightforward to demonstrate that, in first approximation, the 2νDBD is $\sim 10^{21}$ times slower with respect to the single beta decay, resulting in half lives of the order of 10^{18} - 10^{22} years. The experimental observation of 2νDBD is therefore possible only if the single beta decay is forbidden by energy conservation or, at least, strongly hindered by small transition energy or by large change of angular momentum. This condition happens with several nuclei in nature thanks to the pairing interaction [20] in the Von Weizsäker formula which is an excellent parametrization of the binding energies of nuclei in their ground state:

$$M\left(Z,A\right) = a_v A - a_s A^{2/3} - a_c \frac{Z(Z-1)}{A^{1/3}} - a_a \frac{(a-2Z)^2}{A} + \delta(Z,A) \tag{2.2}$$

where the a_i parameters with i=v,s,c,a (volume, surface, Coulomb repulsion and asymmetry) are determined empirically and $\delta(Z,A)$ is the pairing term

$$\delta(Z,A) \propto \begin{cases} +a_p A^{-\frac{1}{2}} & \text{Z,N even (A even)} \\ 0 & \text{A odd} \\ -a_p A^{-\frac{1}{2}} & \text{Z,N odd (A even)} \end{cases}$$

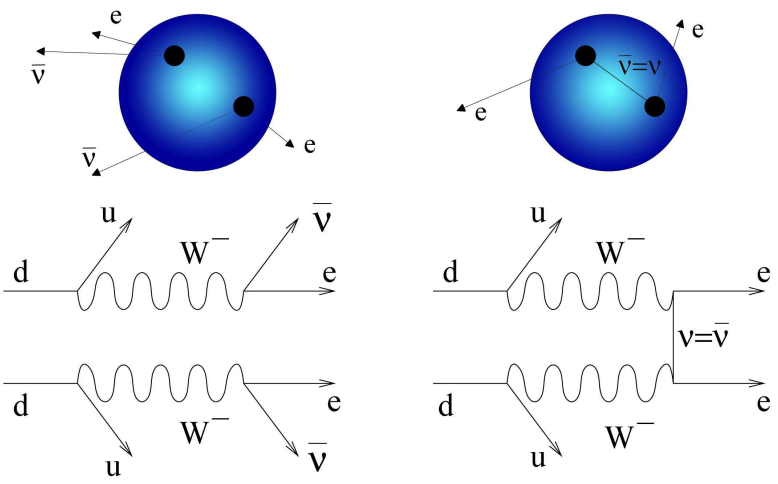

Figure 2.2: Feynman diagram for 2νDBD (left) and 0νDBD (right).

The pairing term is a correction that arises from the tendency of proton pairs and neutron pairs to occur. For a given value of A the nuclear masses follows a parabolic behavior (Figure 2.1). For odd-A the binding energy follows a parabola in Z and only one stable nucleus results. For even-A, both even-even and odd-odd occur so two parabolas, shifted by 2δ, are implied by the mass equation. These are cases where double beta decay can be more easily studied because the single beta decay is forbidden.

The first direct observation of the 2νDBD was obtained in 1987 [21] and is now observed in more than ten nuclei [22], [23].

More interesting from a Particle Physics point of view is neutrinoless Double Beta Decay (0νDBD), first proposed by Furry [24] in 1939. In this case there is maximum lepton number violation (ΔL=2) and the decay is, therefore, not allowed by the Standard Model. The 0νDBD can occur only if two requirements are satisfied:

- the neutrino has to be a Majorana particle
- the neutrino has to have a mass or the neutral current has to have a right handed (V+A) component

The second condition is needed because of the helicity mismatch in the neutrino propagator. Due to the V-A nature of the weak interaction, the neutrino emitted in the first vertex (see Figure 2.2) is right handed, while in order to be absorbed in the second one, it needs to change its helicity. Thanks to the finite mass this is possible with a probability $\sim m_\nu/E_\nu$ and the amplitude of the decay is proportional to m_ν. Disregarding more unconventional contributions (SUSY or left-right symmetric models), the 0νDBD rate is usually expressed as:

$$\frac{1}{T^{0\nu}_{1/2}} = \frac{|m_{\beta\beta}|^2}{m_e^2} G^{0\nu} |M^{0\nu}|^2 = \frac{|m_{\beta\beta}|^2}{m_e^2} F_N^{0\nu} \tag{2.3}$$

Here $T^{0\nu}_{1/2}$ is the decay half life, m_e is the electron mass, $G^{0\nu}$ is the two-body phase-space factor, and $M^{0\nu}$ is the 0νDBD Nuclear Matrix Element (NME). The product $F_N^{0\nu} = G^{0\nu}|M^{0\nu}|^2$ is referred to as *nuclear factor of merit*. While $G^{0\nu}$ can be calculated with reasonable accuracy, the NME value is strongly dependent on the nuclear model used for its evaluation. This problem, discussed in more detail in section 2.1.1, translates in considerable uncertainties in the evaluation of $m_{\beta\beta}$ from the experimentally measured decay half-life.

The effective Majorana mass is the most relevant parameter and is given explicitly by a coherent sum over the contributions of the different ν_i to the electron flavor:

$$|m_{\beta\beta}| \equiv |\sum_i U_{ei}^2 m_i| = |U_{e1}|^2 m_1 + e^{i\alpha_2}|U_{e2}|^2 m_2 + e^{i\alpha_3}|U_{e3}|^2 m_3 \tag{2.4}$$

where U_{ei} are the elements of the first row of the PMNS matrix (see Chapter 1.2), $\alpha_2 \equiv 2\phi_2$, and $\alpha_3 \equiv 2(\phi_3 - \delta)$, ϕ_2 and ϕ_3 being the two Majorana phases. Eq. (2.4) can be written in terms of the neutrino parameters measured by oscillation experiments as:

$$|m_{\beta\beta}| = c_{12}^2 c_{13}^2 m_1 + e^{2i\phi_2} s_{12}^2 c_{13}^2 m_2 + e^{2i(\phi_3-\delta)} s_{13}^2 m_3 \tag{2.5}$$

Given the present experimental results on the parameters governing the neutrino oscillation phenomena, namely $\Delta m_{12}^2 \sim 7.6 \times 10^{-5}\,\mathrm{eV}^2$, $|\Delta m_{23}^2| \sim 2.4 \times 10^{-3}\,\mathrm{eV}^2$, $\tan^2\theta_{12} \sim 0.48$, and $\sin^2 2\theta_{23} \sim 1.02$, the expected allowed ranges for $|m_{\beta\beta}|$ as a function of the lightest neutrino mass are the ones depicted in Fig. 2.3. In the figure it is also possible to observe the parameter space that is excluded by current 0νDBD experiments and by cosmological observations.

2.1.1 Nuclear Factor of Merit

It is clear from Eq. (2.3) that the evaluation of the Nuclear Matrix Elements $M^{0\nu}$ are needed in order to extract $|m_{\beta\beta}|$ from the experimentally measured 0νDBD decay rate. Any uncertainty in the calculated values of $M^{0\nu}$ will reflect in a correspondingly large uncertainty of $|m_{\beta\beta}|$. However, the calculation of $M^{0\nu}$ is very difficult, because it requires an accurate nuclear model: since all 0νDBD candidate nuclei are relatively heavy, the corresponding many body problem cannot be solved without approximations.

Traditionally two different approaches have been used for the evaluation of the NME. These are the *Quasiparticle Random Phase Approximation* (QRPA) and the *Shell Model* (SM). Both methods describe the nucleus as a system of independent nucleons, but differ in the number of nucleon orbits included in the calculations and in the complexity of the

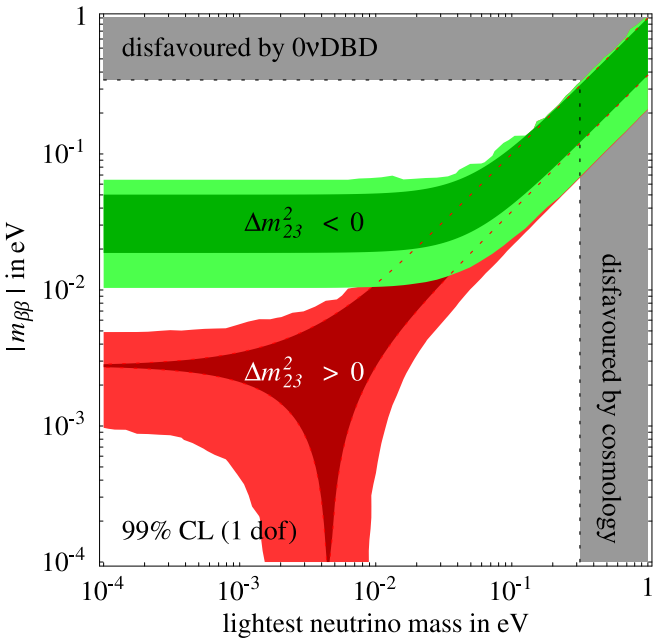

Figure 2.3: 99% C.L. expected ranges for the parameter $|m_{\beta\beta}|$ as a function of lightest neutrino mass. $\Delta m^2_{23} > 0$ corresponds to NH ($m_{lightest} = m_1$), while $\Delta m^2_{23} < 0$ corresponds to IH ($m_{lightest} = m_3$). The darker regions show how the ranges would shrink if the present best-fit values of oscillation parameters were confirmed with negligible errors. [25]

configurations of the nucleons in these orbits. Since the calculations using QRPA are much simpler, most of the results reported in literature refer to this method. There is anyway a spread in the published QRPA results, which originates from the way how the authors deal with approximations, correlations, and parameter fine tuning.

Recently a new method, the *Microscopic Interacting Boson Model* (IBM), has been proposed for the evaluation of NME. In this model the even-even nuclei are described in terms of correlated pairs of protons and neutrons - with angular momentum $J = 0, 2$ - treated as bosons.

Recent results from QRPA [26, 27], SM [28], and IBM [29] nuclear matrix elements calculations are compared in Fig. 2.4, where $F_N^{0\nu}$=$G^{0\nu}M^{0\nu}$ is plotted for different 0νDBD candidates and various nuclear models. Due to the fact that some authors make different parameter choices in evaluating both $G^{0\nu}$ and $M^{0\nu}$ (e.g. the value of r_0 in the nuclear radius $R = r_0 A^{1/3}$, the axial vector coupling g_A, ...), the comparison by means of $F_N^{0\nu}$ sets free from scaling factor inconsistencies [30] among the models, provided that the NME and the kinematic factor are consistently calculated within each model.

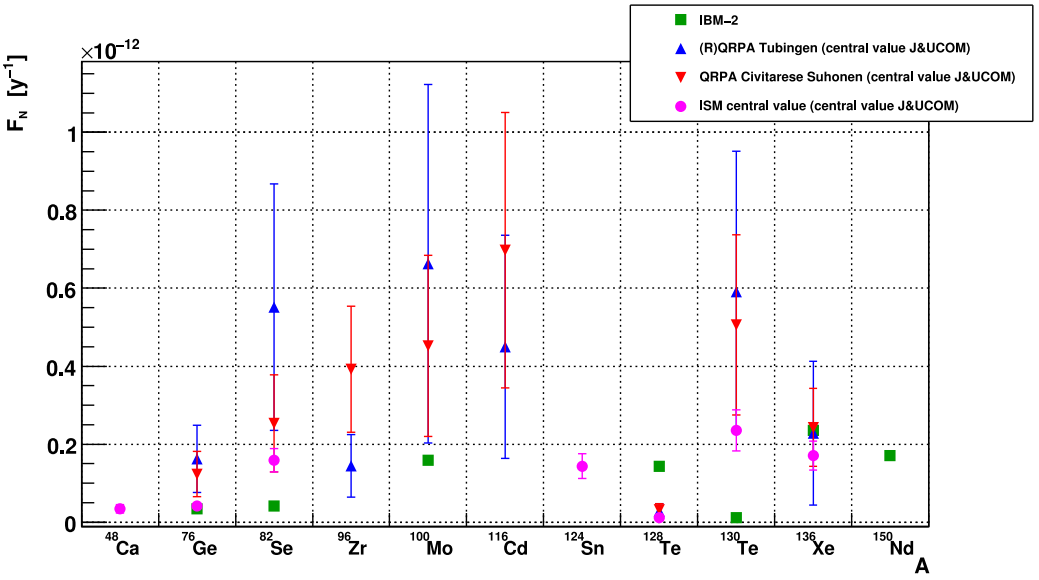

Figure 2.4: Nuclear factor of merit values calculated for different theoretical models.

2.1.2 Experimental signature

From the experimental point of view, neutrinoless Double Beta Decay searches rely on the measurement of the two electron signal. Since the energy of the recoiling nucleus is negligible, the sum of kinetic energy of the two electrons is equal to the Q-value of the 0νDBD transition (Figure 2.5). This monochromatic signal is the main signature used by all the experiments. On the other hand, given the rarity of the process, the gathering of the 0νDBD counts is complicated by the presence of background events in the energy region under investigation which can hinder the searched signal. Possible contributions to these undesired counts can come from environmental radioactivity, cosmic rays, and

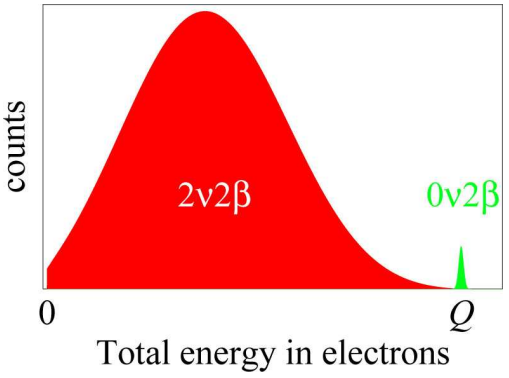

Figure 2.5: Experimental signature of 2νDBD and 0νDBD

0νDBD	Q [keV]	Isotopic Abundance [%]
$^{48}Ca \rightarrow {}^{48}Ti$	4270	0.2
$^{150}Nd \rightarrow {}^{150}Sm$	3367	5.6
$^{96}Zr \rightarrow {}^{96}Mo$	3350	2.8
$^{100}Mo \rightarrow {}^{100}Ru$	3034	9.6
$^{82}Se \rightarrow {}^{82}Kr$	2995	9.2
$^{116}Cd \rightarrow {}^{116}Sn$	2802	7.5
$^{130}Te \rightarrow {}^{130}Xe$	2527	33.7
$^{136}Xe \rightarrow {}^{136}Ba$	2479	8.9
$^{76}Ge \rightarrow {}^{76}Se$	2040	7.8

Table 2.1: Some high Q-value 0νDBD candidates with corresponding isotopic abundances.

2νDBD itself. In fact, any event producing an energy deposition similar to that of the 0νDBD decay increases the background level, hence spoiling the sensitivity of the experiment. Depending on the detector type and set-up features, other characteristic information can be used to discriminate background (e.g. the electron tracks in tracking experiments).

In table 2.1 some high Q-value 0νDBD candidates with corresponding isotopic abundances are reported.

In next section I will focus on experimental techniques to search for this peak pointing out advantages and disadvantages of each technique.

2.2 Experimental Techniques

Experimental approaches for 0νDBD searches can be classified in two main categories:

- **Indirect**: These techniques, which had an important role in the past, measure the anomalous concentration of daughter nuclei in samples with a long accumulation time. They have been used to give indirect evaluations of the 0νDBD and 2νDBD lifetimes. This category includes two type of measurements:
  - Geochemical measurement: determination of the total decay time through the measurement of the daughter nuclei (A,Z+2) produced by the parent nuclei (A,Z) in a sample of old geological rocks.
  - Radiochemical measurement: determination of the total decay time by extraction of the radioactive daughter nuclei from the parent nuclei.

- **Direct**: these are the presently most diffuse techniques, and are based on the direct observation of electrons emitted in the process. Two technical approaches are possible:

  - **Passive source**: the source is external to the detector. The experimental configuration usually consists of foil shaped sources with two detectors (e.g. scintillators, TPCs, drift chambers, etc) analyzing the electrons emerging from the foil. Using tracking detectors a background rejection is possible studying the event topology. The limits of this approach are the energy resolution and the small source mass.
  - **Active source**: the source is internal to the detector (calorimeter). The detector can be a scintillator, a bolometer, a semiconductor diode or a gas chamber. Calorimeters can have large mass and high efficiency. Depending on the technique, also high energy resolution and tracking are possible.

Geochemical and radiochemical experiments do not distinguish the different double beta decay (2νDBD and 0νDBD). Thus, there is little interest in pursuing these techniques further. Instead, relatively new technologies such as bolometers and scintillating crystals are presently receiving attention.

2.2.1 Status of the Art

A series of experiments based on the active source approach allowed to reach excellent sensitivities on 0νDBD. Past and running double beta decay experiments have typical sensitivities that allow to span the effective Majorana mass corresponding to the degenerate neutrino mass hierarchy pattern (see Fig. 2.3).

High purity Germanium detectors (HPGe) are a typical example of the source = detector approach: the investigated nucleus is ^{76}Ge, having a Q-value of 2039 keV. In particular, the best limit on 0νDBD comes from the Heidelberg-Moscow (HM) experiment even if similar results have been obtained also by the IGEX experiment [31].

The Heidelberg-Moscow experiment took data in the period 1999-2003 in the Gran Sasso National Laboratory (LNGS) using five HPGe detectors. The total detector mass was 11 kg, enriched to about 86% in ^{76}Ge. A background of 0.12 counts/(keV·kg·y) was obtained around the Q-value of the decay. With a statistics of 35.5 kg·y in ^{76}Ge, the half life limit obtained by the Heidelberg-Moscow collaboration is $\mathrm{T}^{0\nu}_{1/2} > 1.9 \cdot 10^{25}$ y at 90% C.L. [32]. In 2001 part of the collaboration has re-analysed the full data set claiming a $4.2\,\sigma$ positive hint for the 0νDBD of ^{76}Ge, with $T^{0\nu}_{1/2} = 1.19 \cdot 10^{25}$ y [33]. More recently [34], by an improved pulse shape analysis based on the use of neuronal networks and Monte Carlo simulations, a further background reduction has allowed a confidence level of 6.4 σ for a decay half-life of $T^{0\nu}_{1/2} = 2.23^{+0.44}_{-0.31} \cdot 10^{25}$ y, which would correspond to a $|m_{\beta\beta}|$

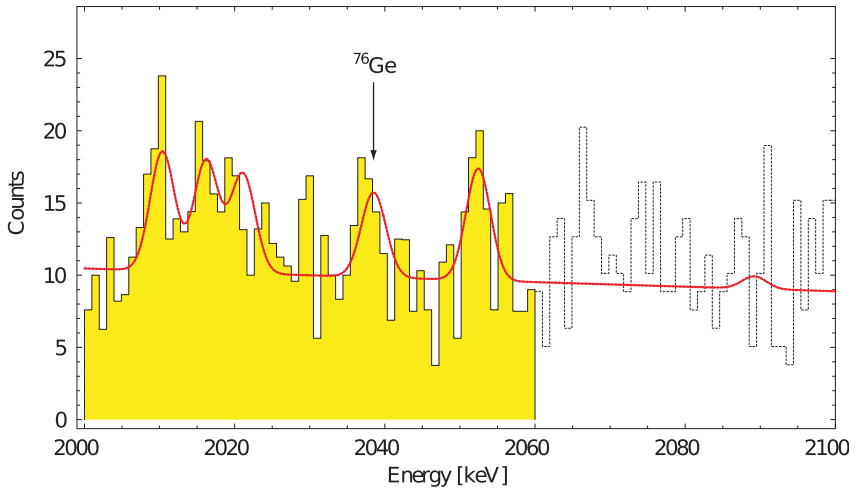

Figure 2.6: Heidelberg-Moscow data used to claim a 4.2σ evidence for ^{76}Ge 0νDBD. The claimed peak is at (2038.07 ± 0.44) keV.

value between 0.21 and 0.59 eV, according to the $F_N^{0\nu}$ values of Fig. 2.4. Since its first appearance, this claim has been strongly criticized by the double beta decay community because of the assumptions made in the background evaluation procedure [35]. Anyway all future double beta decay experiments will have to compare with this result.

The Cuoricino experiment [36] will be widely discussed in the Chapter 5. It was based on TeO_2 bolometers operating at $\sim$ 10 mK to search for neutrinoless double beta decay in ^{130}Te. It operated at LNGS in the period 2003-2008. With a background level in the region of the 0νDBD peak of 0.18 counts/(keV·kg·y), an energy resolution of $\sim$7 keV at 2.6 MeV and an exposure of 19.75 kg·y, Cuoricino obtained a limit on the ^{130}Te 0νDBD half life of $T^{0\nu}_{1/2} > 2.8 \cdot 10^{24}$ y. Using the NME reported in Section 2.1.1 this translates into a limit on the effective Majorana mass of $m_{\beta\beta} < 0.2 \div 0.7$ eV.

Competitive limits on neutrinoless double beta decay come also from the Neutrino Ettore Majorana Observatory - NEMO 3 [37]. Being a tracking experiment, NEMO 3 is not only able to measure the total released energy, but also the energy of the single electrons, their angular distribution and the position where they are produced. NEMO 3 is located in the Frejus Underground Laboratory (France) under a 4800 m.w.e. rock shield. The detector has a cylindrical structure composed by 20 identical sectors. In each sector a thin foil 0νDBD source (30-60 g/cm^2) is surrounded by a He-filled tracking detector consisting in drift cells operating in Geiger mode. A magnetic field facilitates the identification of the background produced by electron-positron pairs. The tracking chambers are surrounded by plastic scintillators to measure the energy of the two electrons. Thanks to the easy way in which the source foils can be replaced in the detector, NEMO 3 can be used to study any kind of 0νDBD isotope. Its great background rejection capabilities make this

detector an ideal tool to study the two neutrino double beta decay mode. At present seven isotopes have been investigated: ^{100}Mo, ^{82}Se, ^{116}Cd, ^{150}Nd, ^{96}Zr, ^{130}Te and ^{48}Ca, but the source mass (about 10 kg) is fairly dominated by ^{100}Mo (about 7 kg) and ^{82}Se (about 1 kg). Limits on the 0νDBD for these isotopes are: $T^{0\nu}_{1/2} > 4.6{\cdot}10^{23}$ y (^{100}Mo) and $T^{0\nu}_{1/2} > 1.0{\cdot}10^{23}$ y (^{82}Se). The corresponding upper limits for the effective Majorana mass range from 0.7 to 2.8 eV for ^{100}Mo and from 1.7 to 4.9 eV for ^{82}Se. Great efforts are needed to improve these results due to the relatively small source masses and the limited energy resolution of this approach.

2.2.2 Future experiment

In order to push $|m_{\beta\beta}|$ sensitivities towards the Inverted Hierarchy (IH) region considerable experimental improvements are needed, first of all a substantial increase of the isotope mass and a simultaneous lowering of the spurious background. Therefore all the efforts of the $\beta\beta$ experimentalists are nowadays absorbed by the design or the construction of the so called "second generation" experiments, with the goal of approaching the IH region ($|m_{\beta\beta}| \geq 50\,\text{meV}$), while considerable R&D is devoted to new techniques which could bring to the full exclusion of the IH mass region ($|m_{\beta\beta}| \geq 15\,\text{meV}$). In Table 2.2 the most significant 0νDBD experiments are reported. In the following is given an overview of experiments under construction and of projects that are carrying out a substantial R&D.

GERDA [38] and Majorana [39] are the next generation Ge calorimetric experiments. Both will use arrays of HPGe diodes, enriched in ^{76}Ge. In both cases segmented HPGe devices and pulse-shape discrimination will be used to guarantee a high efficiency in rejecting multi-site events (mostly gamma background). The main differences between the two experiments rely in the set-up design, traditional in the case of Majorana (with arrays of Ge diodes housed in high purity electroformed copper cryostats and shielded by low background copper and lead) and more innovative in the case of GERDA (the naked Ge detectors will be immersed in an ultrapure LAr tank, surrounded by a water buffer serving both as gamma and neutron shield and as a Cerenkov muon veto). GERDA, presently being under construction at Gran Sasso National Laboratory, will use in its first phase the Heidelberg-Moscow and IGEX detectors (18 kg of ^{76}Ge) aiming at confirming/disclaiming the reported ^{76}Ge positive hint with high statistical significance. In phase II the mass will be increased to $\sim 40\,\text{kg}$ of ^{76}Ge, by adding new segmented HPGe detectors with extremely low intrinsic contaminations, and the background will be reduced by pushing the multi-site energy deposit discrimination technique and by using LAr scintillation light as anti-coincidence signal.

The first phase of Majorana foresees the construction of a demonstrator module with 26 kg of ^{76}Ge with the goal of confirming/disclaiming the ^{76}Ge positive hint and 60 kg of natural Ge for background study. The experiment will be located at Stanford Laboratory.

CUORE [40] is a tightly packed array of 740 kg of natural TeO_2 bolometers, corresponding to $\sim$ 200 kg of ^{130}Te. The project is based on the experience of Cuoricino [36] and MiDBD [41] and foresees the realization of the largest array ever designed to work at 10 mK. It will consist of 19 towers, with 52 detectors each, mounted in a dilution refrigerator and heavily shielded from environmental radioactivity. CUORE, is presently under construction at Gran Sasso National Laboratory and data taking start is expected in 2013. Since a considerable amount of my PhD work took part in the CUORE experiment it will be widely discussed in the Chapter 6.

A new interesting development in the field of low temperature calorimeters is represented by scintillating bolometers (for detail on this technique see Chapter 8). Indeed, this novel type of hybrid detectors can guarantee a significant background reduction by discriminating α from β/γ spurious counts by means of a simultaneous measurement of heat and scintillation light [42]. This is the concept of the LUCIFER project, which aims at looking for the 0νDBD decay of ^{82}Se with one Cuoricino-like tower of ZnSe scintillating bolometers [43]. After an R&D phase to develop the technique for the crystallization of radiopure isotopically enriched ZnSe crystals, the data taking start is expected in 2014.

Other novel techniques for 0νDBD experiments are presently under study. As an example the EXO [44] collaboration is proposing an experiment looking for the 0νDBD decay of ^{136}Xe with large LXe TPC with a quite effective background rejection capability. The idea is to trap and identify the daughter ^{136}Ba ion by laser spectroscopy. Indeed the 0νDBD process produces a daughter Ba^{++} ion which is expected to quickly convert to Ba^{+} in a liquid Xe environment. After being attracted out of the liquid Xe and transported to an ion trap, this barium ion can be optically identified via its atomic spectroscopy by optical pumping with red and blue lasers. The collaboration is also studying the feasibility of Ba tagging in a gas environment (a high pressure Xe TPC would offer topology information and better energy resolution). If this technique will prove to work, all backgrounds but the 2νDBD events will be removed, giving the experiment a high sensitivity. Presently EXO-200, the first phase of EXO, is being commissioned at Waste Isolation Pilot Plant (WIPP) in New Mexico. The detector is a LXe TPC without barium tagging, with the liquid xenon serving both as source and detection medium. The source consists of 200 kg of Xe enriched to 80% in ^{136}Xe. This is the isotope chosen also by the NEXT collaboration [45], that is planning to use a high pressure gas TPC with 100 kg of Xe gas enriched in ^{136}Xe. The experiment will be located at Canfranc Underground Laboratory (LSC).

CANDLES [46] will use CaF_2 crystals immersed in a liquid scintillator to study the 0νDBD of ^{48}Ca. A prototype has been constructed at Osaka University (at sea level). Presently the detector with 96 CaF_2 crystals, for a total mass of 0.35 kg of ^{48}Ca, is being installed in Kamioka underground laboratory. Future steps, to reach the IH mass region, foresee the enrichment of the crystals in ^{48}Ca.

New developments have been recently proposed concerning the possibility to disperse

Experiment	**Technique**	**Isotope**	**Mass [kg]**	**Status**
H-M	*semiconductors*	^{76}Ge	11	*concluded*
IGEX	*semiconductors*	^{76}Ge	8	*concluded*
Cuoricino	*bolometers*	^{130}Te	11	*concluded*
NEMO3	*tracking*	^{100}Mo	6.9	*running*
NEMO3	*tracking*	^{82}Se	0.9	*running*
GERDA I	*semiconductors*	^{76}Ge	18	*construction*
EXO-200	*LXe TPC*	^{136}Xe	160	*commissioning*
CUORE	*bolometers*	^{130}Te	200	*construction*
GERDA II	*semiconductors*	^{76}Ge	40	*detector R&D*
LUCIFER	*scint.bolometers*	^{82}Se	18	*detector R&D*
SNO+	*liquid scintill.*	^{150}Nd	56	*detector R&D*
KamLAND	*liquid scintill.*	^{136}Xe	225-360	*detector R&D*
CANDLES	*scintillator*	^{48}Ca	0.35	*prototyping*
SuperNEMO	*tracking*	^{82}Se	100	*prototyping*
EXO-1000	*LXe+Ba tag*	^{136}Xe	800	*R&D*
Majorana	*semiconductors*	^{76}Ge	26	*prototyping*
NEXT	*gas TPC*	^{136}Xe	80	*prototyping*

Table 2.2: Summary table of most significant 0νDBD recent experiments (upper part) and selected future experiments (lower part).

0νDBD active isotopes in large masses of low activity scintillators. SNO+ [47] will load a liquid scintillator with 0.1% natural Nd inside the acrylic vessel of the now concluded SNO solar neutrino experiment, in SNOLAB facility. According to some preliminary simulations, the source would consist of $\sim 56\,\mathrm{kg}$ of ^{150}Nd. The filling of the scintillator in the vessel is foreseen in 2011. A similar approach is proposed by KamLAND [48], to study the $\beta\beta(0\nu)$ of ^{136}Xe. The idea is to dissolve Xe enriched at 90% in ^{136}Xe inside a liquid scintillator in KamLAND experimental facility. In the first phase, to be started in 2011, $\sim 250 - 400\,\mathrm{kg}$ of the candidate isotope should be used, with the goal of scrutinizing the ^{76}Ge claim and studying the entire DH region of the mass spectrum. In a second phase a Xe mass of about 1 ton should allow to explore the IH region.

Concerning purely inhomogeneous detectors the SuperNEMO [49] project will apply the NEMO3 technique to planar structure detectors where the energy resolution and the efficiency will be improved in order to guarantee, together with the increased isotope mass, a sensitivity on $T^{0\nu}_{1/2}$ of the order of $10^{26}\,\mathrm{y}$. The isotope to be investigated chosen as baseline of the experiment is ^{82}Se, but other possible candidates are ^{48}Ca and ^{150}Nd (depending on the enrichment possibilities). The location will most likely be the enlarged Fréjus Underground Laboratory (LSM) and the construction of the experiment is foreseen after 2012.

All these experiments aim at reaching a sensitivity on $|m_{\beta\beta}|$ of the order of 50 meV, approaching but probably not completely covering the inverse hierarchy region. Indeed the feasibility of an experiment able to provide a complete coverage of the IH region has not yet proved.

The realization of an experiment, with the best sensitivity and a reasonable discovery potential down to the smallest $|m_{\beta\beta}|$ values allowed by the IH interval, is today an incredible challenge in which detector technology plays a key role. In this context, the activities I have done during my PhD are focused on the study of the properties of some scintillating bolometers to evaluate the best candidate for a future experiment based on this technique.

Chapter 3

0νDBD sensitivity and background

In recent years great efforts have been made to reduce the radioactive background and to improve the energy resolution in 0νDBD experiments. Further kinematical and topological informations can help improving the signature and test model predictions. The excellent results obtained have allowed, in practice, to approach significantly the "zero background" condition (Chapter 8, 9, 10). In this chapter, after defining the experimental sensitivity, I will focus on the different sources of background in macro-bolometers for 0νDBD . The other parameters which determine the sensitivity will also be discussed in detail. Here, the most relevant result is that for a given detector mass M there always exists a threshold background level below which no further improvement of the sensitivity is obtained. This means that for experiments near the "zero background" condition it can be useless reduce the background without a corresponding increase of the experimental mass or that a balanced improvement in both background level and detector mass is required in order to have an effective increase in sensitivity.

3.1 Experimental sensitivity

The experimental signature of 0νDBD is a well defined peak at the Q-value of the transition. In the fortunate event of a 0νDBD peak showing up in the energy spectrum, the decay half life can be easily evaluated as

$$T_{1/2}^{0\nu} = \ln 2 \; T \; \epsilon \; \frac{N_{\beta\beta}}{N_{peak}} \tag{3.1}$$

where T is the measuring time, ϵ is the detection efficiency, $N_{\beta\beta}$ is the number of $\beta\beta$ decaying nuclei under observation, and N_{peak} is the number of observed 0νDBD decays. If no peak is detected, the sensitivity of a given 0νDBD experiment is usually expressed in

term of the *detector factor of merit* ($S^{0\nu}$), defined as the process half-life corresponding to the maximum signal that could be hidden by the background fluctuations n_B at a given statistical Confidence Level (C.L.). At 1σ one has $n_B = \sqrt{BTM\Delta}$ and therefore obtains:

$$S^{0\nu} = T_{1/2}^{Back.Fluct.} = \ln 2 \; T \; \epsilon \; \frac{N_{\beta\beta}}{n_B} = \ln 2 \; \epsilon \; \frac{x \; \eta \; N_A}{A} \sqrt{\frac{M \; T}{B \; \Delta}} \quad (68\% \; C.L.) \tag{3.2}$$

with

$$N_{\beta\beta} = \frac{x \; \eta \; M \; N_A}{A} \tag{3.3}$$

where B is the background level per unit mass, energy, and time, M is the detector mass, Δ is the FWHM energy resolution, x is the stoichiometric multiplicity of the element containing the $\beta\beta$ candidate, η is the $\beta\beta$ candidate isotopic abundance, N_A is the Avogadro number, and finally A is the compound molecular mass.

Despite its simplicity, Eq. 3.2 has the advantage of emphasizing the role of the essential experimental parameters: mass, measuring time, isotopic abundance, background level, energy resolution, and detection efficiency. Most of the demands to be considered when optimizing the design of a new 0νDBD experiment are indicated in it:

- a well performing detector (e.g. good energy resolution and time stability) giving the maximum number of informations (e.g. electron energies and event topology) to better discriminate the background
- a reliable and easy to operate detector technology requiring a minimum level of maintenance (long running times)
- a very large (possibly isotopically enriched) mass, of the order of one ton or larger
- an effective background suppression strategy

Of particular interest is the case when the background level B is so low that the expected number of background events in the region of interest along the experiment life is of order of unity: $BMT\Delta \simeq 1$. In such cases one generally speaks of "zero background" experiments, a condition sought by future projects. In such conditions, n_B is a constant (let's indicate it with n_L) and Eq. 3.2 is no more valid and the sensitivity is given by

$$S_{0B}^{0\nu} = \ln 2 \; T \; \epsilon \; \frac{N_{\beta\beta}}{n_L} = \ln 2 \; \epsilon \frac{x \; \eta \; N_A}{A} \frac{M \; T}{n_L} \tag{3.4}$$

The constant n_L depends on the chosen C.L. and on the actual number of observed events. The most relevant feature of Eq. 3.4 is that $S_{0B}^{0\nu}$ does not depend explicitly on the background level or the energy resolution and scales linearly with the sensitive mass M and the measure time T.

Since T is usually of the order of few years and Δ is usually fixed for a given experimental technique, the "zero background" condition ($BMT\Delta \simeq 1$) depends only on the product of the background level and the mass of the source ($B \cdot M$). This means that for a given mass M there exists a threshold for B below which no further improvement of the sensitivity is obtained. In other words it is useless to reduce further the background level without a corresponding increase of the experimental mass (i.e. it is useless to have no background events if we have also no events of the searched process).

It is clear from Eq. 3.2 and 3.4 that high isotopic abundances η are preferable, as they correspond to an increase of the number of 0νDBD nuclei that are put under observation. Despite being rather expensive, isotopic enrichment is often a forced choice for those candidate nuclei that have low natural abundances (Table 2.1).

Isotopes with high Q-value are also a better choice, for several reasons. First, the background from natural radioactivity decreases with increasing Q. Moreover phase space factor scales as $G^{0\nu} \sim Q^5$ [50].

Finally, also the detector structure is very important. It directly determines the detection efficiency ϵ and the stoichiometric multiplicity of the element containing the $\beta\beta$ candidate x.

I will discuss in the following paragraphs each of these fundamental parameters pointing out there most relevant features and criticalities.

3.2 Energy resolution

The theoretical energy resolution of a detector is generally related to the statistical fluctuation of the number of elementary events contributing to the signal (e-h pairs for solid state detectors, phonons for bolometers, ...). A very simple estimate can be made by assuming that the process of formation of each carrier is ruled by a Poisson statistics. Under this assumption, if a total number N of carriers is generated on the average, one would expect Poisson distribution of the counts, characterized by a standard deviation of $\sqrt{N}$. If this were the only source of fluctuation in the signal and offer a sufficiently large number of counts, one would expect a Gaussian response function.

Since then the response of many detectors is approximately linear, we can write H$\simeq$KN, where K is a proportionality constant and H is the average pulse amplitude. The Gaussian distribution is therefore characterized by a standard deviation σ=$K\sqrt{N}$ and a FWHM

$$FWHM = 2.35K\sqrt{N} \tag{3.5}$$

Thus the statistical contribution to the percent energy resolution R can be parametrized as

$$R = \frac{FWHM}{H} = \frac{2.35K\sqrt{N}}{KN} = \frac{2.35}{\sqrt{N}} \tag{3.6}$$

It is clear that a large number of carriers allows to reach better energy resolutions. Such a number is inversely proportional to the energy required for the production of a single carrier. In the case of bolometers this turns out to be much lower than for any other technique and thus the theoretical resolution is orders of magnitude better than for standard technique (for a more detailed description of the bolometric technique see Chapter 4). In real bolometers, however, other sources affect the energy resolution such as extrinsic noise that, anyhow, makes these detectors, together with the Ge diodes, the ones with the best energy resolution.

Since the signature of 0νDBD is a well defined peak in the energy spectrum, good energy resolution is a very important requirement because allows it to stand out on the background. Moreover, in experiments for 0νDBD this requirement is much more important because of the 2νDBD: an isotope candidate to neutrinoless Double Beta Decay will decay also with two neutrino with a continuum spectrum up to the Q value of the transition. Without a good energy resolution, the searched peak will be covered by the tail of the 2νDBD. The ratio between the number (S) of 0νDBD in the region of interest and the background (B) due to 2νDBD is [51]

$$\frac{S}{B} = \frac{m_e Q^5}{7\Delta^5}\frac{T_{1/2}^{2\nu}}{T_{1/2}^{0\nu}} \tag{3.7}$$

where m_e is the electron mass, $T_{1/2}^{2\nu}$ and $T_{1/2}^{0\nu}$ are, respectively, the half life of 2νDBD and 0νDBD. It is important to note the heavy dependence of equation 3.7 on the fifth power of the energy resolution (Δ^5).

Thanks to the very good energy resolutions reachable with some techniques based on the active source approach (source=detector) this problem can be completely ruled out.

3.3 Detector material

It is straightforward that the more material is used as detector the bigger is the probability to observe the searched process. In the case of a "zero background" experiment this relation is linear and the experimental sensitivity scales proportionally to the detector mass. This is not true however in the case of detectors with a measurable background for which the detector sensitivity depend only on the square root of mass (Eq. 3.2).

However, the size is not the only important detector parameter affecting the experimental sensitivity. The detector material play also a primary role. The 0νDBD half live (Eq. 2.3), and then the sensitivity, depend indeed on the nuclear factor of merit $F_N^{0\nu} = G^{0\nu}|M^{0\nu}|^2$. It is then straightforward that the choice of an isotope with a favorable

Crystals	Natural isotopic abundance	$N_{\beta\beta}$/kg
TeO_2	33.7 %	$1.27 \cdot 10^{24}$
ZnSe	9.2 %	$3.83 \cdot 10^{23}$
$ZnMoO_4$	9.6 %	$2.56 \cdot 10^{23}$
$CaMoO_4$	9.6 %	$2.41 \cdot 10^{23}$
$CdWO_4$	7.5 %	$1.25 \cdot 10^{23}$

Table 3.1: $N_{\beta\beta}$ for some crystals used for 0νDBD searches.

Nuclear Matrix Element $M^{0\nu}$ and with a good phase-space factor $G^{0\nu}$ is highly preferred. This corresponds to a high Q value ($G^{0\nu} \sim Q^5$) [50].

Moreover, the background from natural radioactivity decreases with increasing Q. A marking point is represented by the 2615 keV line from ^{208}Tl, the highest energy γ-line from natural radioactivity. Isotopes with Q-values above this energy benefit from a much lower background level.

The experimental sensitivity depends also on the isotopic abundance η, on the detector efficiency ϵ and on the stoichiometric multiplicity x. All these parameters are connected to the material used as detector. For bolometers the detection efficiency is generally quite high. It depends mainly on the physical properties of the detector, such as the crystal size and density, and on the Q value of the transition. For macro-bolometers, such as the ones used in Cuoricino (Chapter 5), the detector efficiency is ∼85%.

The isotopic abundance and the stoichiometric multiplicity play indeed a primary role in the number of candidate nuclei to 0νDBD (see Eq. 3.3). Except for ^{130}Te which is the only candidate with an exceptionally large natural abundance (∼34%) the other interesting nuclei (^{76}Ge, ^{82}Se, ^{96}Zr, ^{100}Mo, ^{116}Cd, ^{136}Xe, ^{150}Nd) have a natural abundance between 5% and 10%.

On the other hand enrichment is a possible way out but then costs and feasibility are the true problems. For sure it is much better to enrich materials with an already high natural isotopic abundance of the interesting isotope. For next generation experiments is indispensable to take into account also the cost and the feasibility of enrichment.

Finally, another feature related to the detector material influences the isotope choice: the value of the 2νDBD half-life. As mentioned above, 2νDBD is an irreducible source of background that can prevent the use of some isotopes in a high sensitivity experiment. The ratio between the number of 2νDBD and 0νDBD decays in the energy region of interest for 0νDBD can be evaluated considering the measured $T^{2\nu}_{1/2}$ half-life for a given $T^{0\nu}_{1/2}$ (Eq. 3.7).

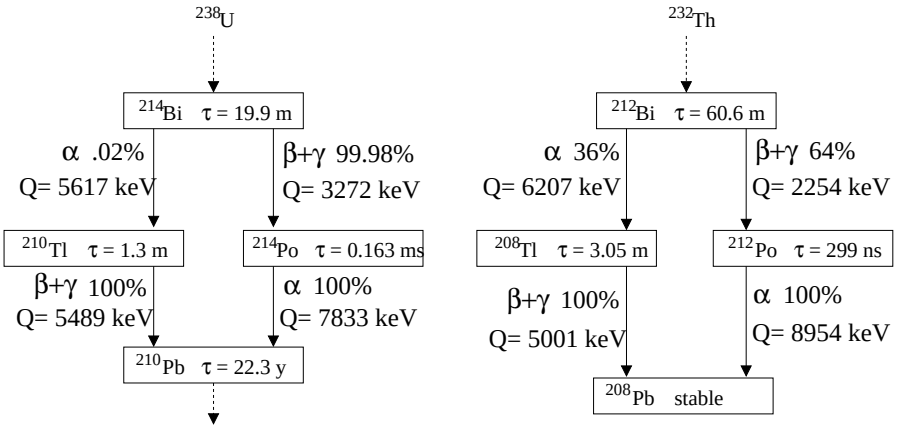

Figure 3.1: High energy β - γ decays of the ^{238}U and ^{232}Th chains preceded (or followed) by an α emission. Using delayed α coincidences, β - γ decays can be identified.

3.4 Radioactive background in macro-bolometer

The possibility to study rare events is strongly influenced by the background level (i.e. the number of events that can mimic a 0νDBD decay) in the Region Of Interest (ROI). For 0νDBD searches the ROI, strictly speaking, corresponds to a narrow region centered around the $\beta\beta$ transition energy. Background contributions extend however well outside the ROI and the crucial region for the study of the background is between $\sim$2.5 and $\sim$4 MeV (except for ^{76}Ge). There are sundry sources that can give rise to spurious counts in this region such as environmental gamma radioactivity, cosmic rays, neutrons, radon and contamination of materials which detectors and their shielding are made of.

In the following sections I will discuss background in deep underground laboratories, in particular at LNGS, were some experiments for rare events searches are located in order to reduce the background due to cosmic rays.

Depending on their origin, in the case of bolometers, the background sources can be divided into three broad categories: internal contaminations, external contaminations and surface contaminations.

3.4.1 Internal background

In the case of crystal bulk contaminations the main contribution to the background rate in the ROI comes from the beta/gamma emissions of the natural chains. Indeed the kinetic energy of α's emitted by U and Th daughters are always far above the ROI we are considering. Here we consider only natural decay chains because these contaminations are usually present in small amounts in all the crystals used. However, some crystals may contain other isotopes, not belonging to natural chains, which can decay with emission

of α or β producing background in the region of interest. Usually these contaminations are specific to given materials and its choice or the purification procedure play therefore a crucial role. In the following the individual cases will be described.

The β emitters of the natural chains that could take part to the background formation in the ROI are ^{208}Tl (^{232}Th chain), ^{214}Bi and ^{210}Tl (^{238}U chain) (see Fig. 3.1). ^{208}Tl beta decays with a Q-value of 5 MeV and a half-life of 3 min. It gives rise to a continuous spectrum of electrons which, in combination with the gammas emitted in the re-assessment of the daughter nucleus, can produces a fastidious set of counts extending to the ROI. However, the background induced by this isotope can be effectively rejected with the use of a delayed coincidence between the ^{208}Tl signal and the α emitted by its precursor, ^{212}Bi (alpha particle energy = 6 MeV). The coincidence pattern to be studied would then be an event in the 0νDBD region preceded by an α particle of 6 MeV. Provided that the α background counting rate at 6 MeV is not too high, the dead time introduced by this operation is low or even negligible. A quantitative evaluation of this source of background and the corresponding dead time based on internal contaminations measured in some bolometers is reported in Table 10.2.

In the ^{238}U chain the only contribution above 2.7 MeV comes from the β decay of ^{214}Bi. However this isotope decays with a B.R. of 99.98% to ^{214}Po which α decays with a very short half-life (163 μs) and a Q-value of 7.8 MeV. Bolometer signals development is of the order of seconds and the chain ^{214}Bi $\rightarrow^{214}$Po$\rightarrow^{210}$Po gives therefore rise to a pile-up event easily rejected. In the residual 0.02% of cases, ^{214}Bi α decays on ^{210}Tl that is a β emitter with a Q-value of 5.4 MeV and an half-life of 1.3 min. The background induced by this β emitter can be easily rejected with the use of a delayed coincidence between the ^{210}Tl signal and the ^{214}Bi alpha, as in the case of ^{212}Bi $\rightarrow^{208}$Tl chain.

Moreover we have to take into account that for slow detectors, like bolometers, even feeble beta/gamma emissions ($\sim$mBq) with Q<2 MeV can produce an unwanted background due to the difficulty to recognize and reject pile-up on the rise time of the thermal pulse. Indeed independent signals can randomly add generating a background that extends even beyond the ROI. TeO_2 [52] and scintillating crystals (Chapter 8) have already shown to reach internal contaminations of the order of μBq/kg.

3.4.2 External background sources

Contribution from external background sources can be divided in: environmental gamma radioactivity, cosmic rays (muons) and neutrons.

Gammas

The main source of natural gamma radioactivity below 3 MeV is due to α and β decays in the environmental materials that leave daughter nuclei in a excited nuclear state that

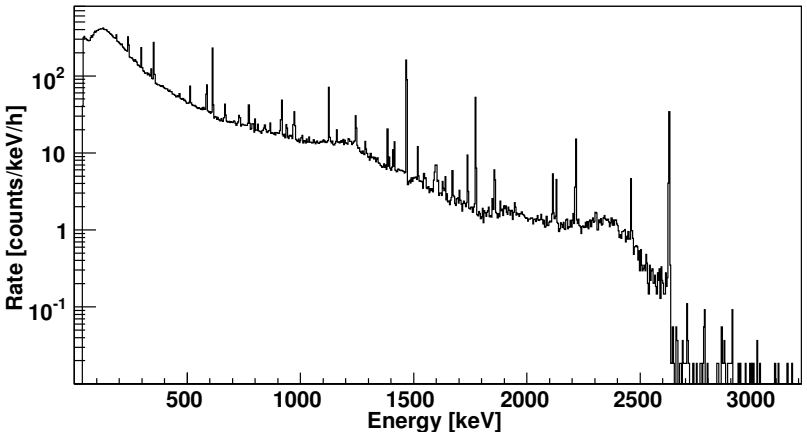

Figure 3.2: Gamma ray spectrum measured at LNGS (Hall A) with a small Ge diode.

decay with the emission of γ rays. The main components of natural γ radioactivity are ^{40}K and elements in the three decay chains of ^{238}U, ^{232}Th and ^{235}U. The 2615 keV γ-line of ^{208}Tl can be considered the most energetic γ-line of natural radioactivity. Indeed, above this value, there are only rare γ lines mainly due to ^{214}Bi. Another source of gamma rays are nuclear reactions induced by interaction of neutrons and muons with matter. This source of background is usually characterized by intensities that are order of magnitude lower than the previous one. However it extend to higher energies and then could be a problem especially for experiments that search a peak at energies higher than 2615 keV.

In Figure 3.2 the γ ray spectrum due to natural rock radioactivity, as measured by a small Ge diode in the Hall A of LNGS, is shown. The reconstructed flux obtained by deconvolving the detector response is reported in Tab. 3.2 [53]. The integral gamma ray flux below 3 MeV has been reconstructed to be $\sim$0.73 $\gamma/s/cm^2$. Above 3 MeV the main contribution to the gamma background comes from photons produced by neutron and muon interactions in the rocks. Due to their high energies and lower flux (estimated to be 10^5 times smaller than the flux of the 2.6 MeV gamma-ray of ^{208}Tl in the rock [54]) these photons cannot be measured with a small Ge diode.

In order to shield from this source of background thick layers of materials with high atomic numbers and high density are required. However, in the design of these shieldings it is necessary to take into account that the use of large quantities of materials with high atomic number increases the production of secondary gamma rays due to nuclear reactions induced by muons and neutrons.

Energy interval [keV]	Gamma flux [γ/s/cm^2]
0 - 500	0.51
500 - 1000	0.12
1000 - 2000	0.08
2000 - 3000	0.015

Table 3.2: Gamma-ray flux (γ/s/cm^2) in the underground Hall A of LNGS.

Neutrons

Neutrons with high kinetic energy can release energy in the ROI through direct scattering with atoms of the bolometer. Thermal neutrons, however, may also contribute through (n, γ) reactions with elements of the shields producing γ with energy extending up to $\sim$10 MeV. These γ, interacting with the detector, can then lead to unwanted background.

In a deep site the neutron flux below $\sim$10 MeV is mainly due to spontaneous fission (the most important source being ^{238}U) and (α,n) processes due to interactions of α's from natural emitters with light target nuclei in the rock. Neutrons with energies above $\sim$10 MeV are produced by nuclear reactions induced by cosmic ray muons in the rock and their flux can extend up to a few GeV. Results obtained by neutron flux measurements at LNGS [55, 56] are reported in Tab. 3.3. Simulations for both radioactivity induced and muon induced neutrons are found in literature [57, 58, 59]. In the case of radioactivity induced neutrons the comparison with experimental results is rather good, while in the case of muon induced neutrons this comparison is not possible since this component dominates the environmental neutron flux only above $\sim$10 MeV, a region where poor experimental data is available. This flux can be however computed on the basis of Monte Carlo simulations. Existing simulations performed to evaluate the muon induced neutrons at LNGS [57, 59] yield an integral flux above 10 MeV that is three orders of magnitude lower than the radioactivity induced one, that amounts to $\sim 4 \cdot 10^{-6}$ n/s/cm^2 below 10 MeV. Also muon induced cascades or showers in the setup materials (especially high A materials for gamma-ray shielding such as lead) can be an important source of hard neutrons.

Neutrons moderation is generally obtained by using several cms layer of hydrogen rich compounds (e.g. water and polyethylene). The resulting thermal neutrons absorption is then based on the use of shield built out of materials (isotopes) with a high neutron capture cross section (B and Li are among the most used).

Energy interval [MeV]	Neutron flux[10^{-6} n/s/cm^2] Ref. [55]	Ref. [56]
10^{-3} - 2.5	-	0.54 ± 0.01
1 - 2.5	0.14 ± 0.12	-
2.5 - 5	0.13 ± 0.04	0.27 ± 0.14
5 - 10	0.15 ± 0.04	0.05 ± 0.01
10 - 15	$(0.4 \pm 0.4)\ 10^{-3}$	$(0.6 \pm 0.2)\ 10^{-3}$
15 - 25		$(0.5 \pm 0.3)\ 10^{-6}$

Table 3.3: Neutron flux measurements at the underground Gran Sasso laboratory.

Muons

Secondary cosmic radiation at sea level is composed mainly of muons with a $cos^2\theta$ angular distribution and energies that extends up to several TeV. Muons, being very deep penetrating particles, cannot be removed by man-made shieldings. For this reason, rare event experiments must be located deep underground.

The cosmic muon flux at LNGS is reduced by about six orders of magnitude with respect to the outside flux by the 3600 m.w.e. shield, provided by the mountain itself [60]. The average muon energy in the underground site is 270 GeV [61] with an integrated flux of $\sim(3.2 \pm 0.2)\cdot10^{-8}$ μ/s/cm^2 [62] and average zenith angle $\langle\theta\rangle \sim 35°$. The distribution of the azimuth angle ϕ follows the profile of the mountain. The differential flux and zenith angle dependence have been measured by LVD [60] and MACRO [63].

Generally, direct interactions of muons in the detector are not particularly dangerous. A minimum ionizing particle traversing a CUORE crystal would cause an energy deposition of a few tens of MeV, which is well above the Q-value of 0νDBD. Moreover the contribution to the background of direct muon interactions as well as of the muon generated electromagnetic showers, can be reduced by means of an anti-coincidence cut between different bolometers. On the other hand, gamma and neutron background arising from muon interactions in the setup are very dangerous. The presence of high density and high mass number (A) shields makes the situation even worse (the neutron yield is proportional to $A^{0.8}$ [85]).

Despite the substantial reduction of the cosmic ray flux at LNGS, this component could still be a significant source of background for experiments needing extremely low background. For this reason, during my PhD, I studied, through the comparison between Monte Carlo simulations and dedicated measurements, the Cuoricino background due to muons. I then extrapolated the results to CUORE. Details of the method and of the results obtained are given, respectively, in the Chapter 5 and Chapter 6.

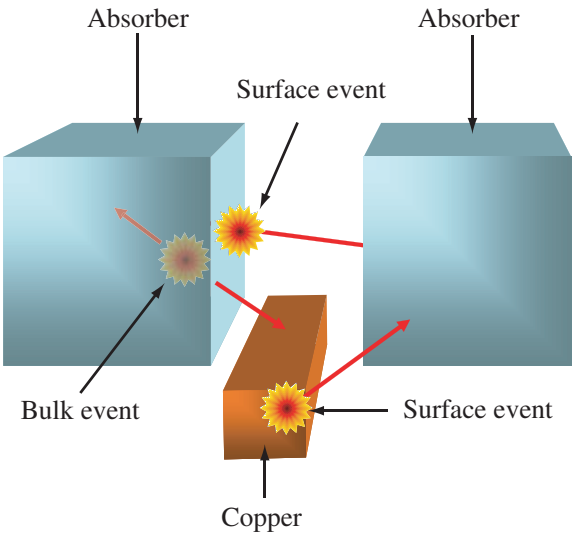

Figure 3.3: Degraded α particles due to surface contaminations.

3.4.3 Surface contamination

The kinetic energy of α particles emitted by U and Th daughters are always far above the ROI for 0νDBD. Therefore α particles give contributions only if they loose a limited fraction of their energy in the bolometer. Unfortunately this condition is not rare and happens whenever the contamination is localized on the surface of the crystal or of the material facing the detector. It should be stressed that a contamination in a shallow layer at the surface of the material facing the detector produces events only in one detector (see Figure 3.3). On the contrary, a contamination on the surface of a crystal can produce an event in two crystals within the same time coincidence window (for example, the nuclear recoil can be absorbed in a crystal and the α particle in another one). In the first case we speak of a multiplicity one or anti-coincidence spectrum while in the second of coincidence spectrum.

The Cuoricino data analysis (Chapter 5) allowed to extrapolate important information on surface contamination in the bolometric technique. The Figure 3.4 shows the spectrum of Cuoricino background above 2.3 MeV. A number of structures superimposed to a continuous background can be easily recognized. Most of the peaks appearing in the region above 4 MeV are ascribed to ^{238}U and ^{232}Th surface contamination of the crystals. In Figure 3.5 the Cuoricino background in the 0νDBD region is shown. Above the 2615 keV line a flat continuous background, attributed to degraded alpha particles, is visible. The comparison between the coincidence and the anti-coincidence spectrum allows to assess how much is due to surface contamination of the crystals and how to copper surface

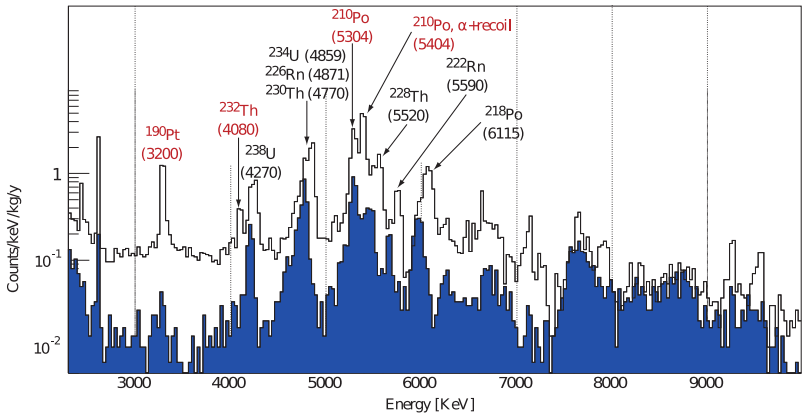

Figure 3.4: Cuoricino background above 2.3 MeV. The black line refers to the anticoincidence events spectrum, the blue filled histogram refers to coincidence events. Most of the peaks appearing in the region above 4 MeV are ascribed to ^{238}U and ^{232}Th surface contamination of the crystals.

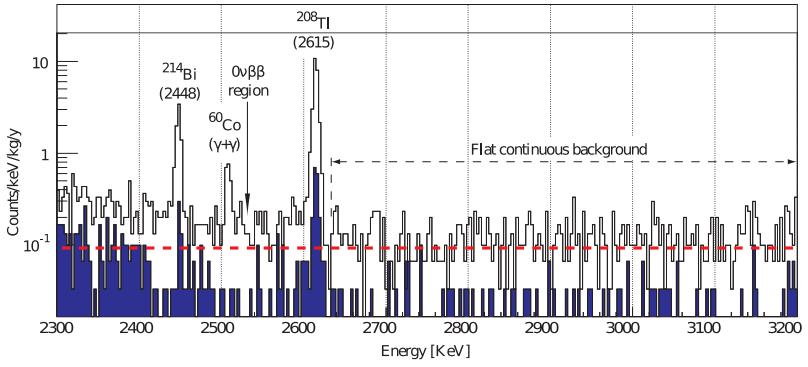

Figure 3.5: Cuoricino background in the 0νDBD region. The black line refers to the anticoincidence events spectrum the blue filled histogram refers to coincidence events. Above the 2615 keV line a flat continuous background, attributed to degraded alpha particles, is visible.

contamination.

A quantitative analysis of Cuoricino background above the 2615 keV line is reported in Table 3.4.

Source	3-4 MeV
TeO_2 ^{238}U and ^{232}Th surf. contam.	20± 10%
Cu ^{238}U and ^{232}Th surf. contam.	80± 10%

Table 3.4: Estimate of the relative contributions of the different sources responsible for the flat background measured in Cuoricino in the 3-4 MeV energy region.

In order to better understand and reduce the background due to surface contamination various measurements in the hall C of LNGS have been carried out. As will be shown in Chapter 7, these measures allowed to develop procedure able to reduce this component. A residual background still larger than expected is however observed. Mainly for this reason we undertook the development of scintillating bolometers for the study of 0νDBD which will be described in Chapter 8.

Chapter 4

The Bolometric Technique

Bolometers are calorimeters, operated at about 10 mK, in which the energy released in the absorber by an interacting particle is converted into phonons and measured via a temperature variation. The bolometric technique is one of the most promising approaches for rare events studies such as 0νDBD and Dark Matter. Indeed this technique has some especially favorable features for the study of rare events:

- the energy resolution is better than of most of the other particle detectors
- there is the possibility to build massive experiments (up to 1 ton)
- a wide choice of different materials that can be used as absorber

This last feature is very important since in the case of 0νDBD searches it can allow to cross check a possible evidence on different isotopes whereas in the case of Dark Matter it allows to probe different mass regions.

Moreover, if other excitations (such as ionization charge carriers or scintillation photons) are collected in addition to phonons, bolometers have already shown to be able to recognize the nature of the interacting particle (α, β/γ or neutrons).

In this chapter I will show the working principles of the bolometric technique with particular attention to its application in the 0νDBD research.

4.1 Working Principles

Conventional spectroscopic techniques are based on the detection of the energy released in the form of ionization and/or excitation of the detector's atoms. Unfortunately, a sizeable

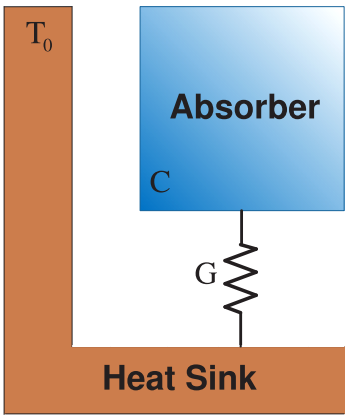

Figure 4.1: Simplified bolometer thermal model. The detector is modeled as a single object weakly coupled to the heat sink. The heat capacity C contains all the contribution of the elements which compose the detector. G describes the thermal conductance between the detector and the heat sink.

fraction of the released energy is dissipated into invisible channels and is finally converted in phonon excitations inside the detector.

The bolometric technique measures just the phonon component by means of the related temperature rise.

In 1935 S. Simon [64] proposed the use of temperature detectors to study nuclear phenomena. In 1949 H.D. Andrews, for the first time, detected alpha particles using superconductive bolometers [65]. In the following years the possibility of using thermal detectors for various research topics (such as solar neutrinos and X-ray spectroscopy, material contamination analysis, dark matter detection and rare processes) was a strong motivation for the development of this technique. However the use of large bolometric detectors for particle detection is rather recent. In particular their application for rare event physics was first suggested by E. Fiorini and T.O. Niinikoski in 1983 [66].

Bolometers can be essentially sketched as a two component object:

- **Energy absorber:** this is the sensitive part of the detector, where the interacting particles deposit their energy. The absorber material can be chosen from a wide variety of compounds, provided they have a low enough heat capacity at the working temperature.
- **Phonon sensor:** it converts the excitation (i.e. phonons) produced by particle interaction into an electrical signal.

A bolometer could be schematized as a calorimeter with a heat capacity C connected to a heat sink, with constant temperature (T_0), through a thermal conductance G (Figure

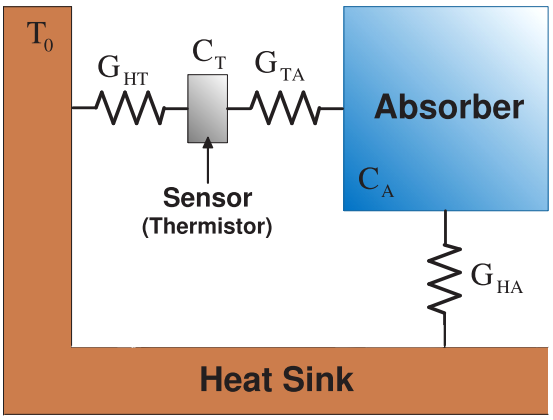

Figure 4.2: A two-stage thermal model: G_{HA} describes the conductance between the heat sink and the absorber, G_{TA} describes the conductance between the absorber and the sensor, and G_{HT} describes the conductance between the sensor and the heat sink.

4.1). The heat capacity term includes all the contributions of the elements which compose the detector: the heat capacity of the absorber (C_A) and of the sensor (C_T). The conductance G represents the thermal connection between the detector and the heat sink and its heat capacity is considered negligible.

For a given absorber with temperature T(t) at time t one can assume that:

$$\Delta T = |T(t) - T_0| << T_0 \quad \forall t \quad \Rightarrow \quad G, C = \text{const} \tag{4.1}$$

so that one can treat G and C as constant. Therefore, an ideal instantaneous deposition of energy ΔE in the absorber gives rise to a temperature variation:

$$\Delta T(t) = \frac{\Delta E}{C} e^{-\frac{t}{\tau}} \qquad \tau = \frac{C}{G} \tag{4.2}$$

One can easily see from equation 4.2 that the heat capacity is a very crucial parameter for this kind of device: the smaller is C and the higher is the signal amplitude.

The heat capacity at the temperature T is given by:

$$C(T) = c(T) \cdot n \tag{4.3}$$

where c(T) is the specific heat at temperature T and n the number of moles in the absorber. In order to minimize C, one has to use a suitable material (such as dielectric and diamagnetic crystals or superconductors below the transition phase) and, most importantly, operate the detector at a very low temperature. For bolometers the typical operating temperature is in the range of $\simeq (10 \div 100)$mK.

A real bolometer is somewhat more complicate than the naive description here presented. It is made of different elements (a slightly more detailed scheme is reported in

Figure 4.2) and it is therefore represented by more than one heat capacity and heat conductance. In principle, if the bolometer performs as an ideal calorimeter and if the conversion of the energy into heat deposited by the particle is instantaneous, then the device is insensitive to the nature of the impinging particle. However, this situation is generally very far from reality, as it will be shown in Chapter 9.

4.2 Energy Absorber

As described in the previous section, one of the most important parameters of the detector is its heat capacity, which needs to be kept as small as possible in order to achieve large and fast signals. To fulfill this requirement, low temperatures are needed.

Indeed, at low temperatures the specific heat of a crystal can be expressed as:

$$c(T) = c_r(T) + c_e(T) + c_m(T) \tag{4.4}$$

where c_r, c_e and c_m represent, respectively, the lattice, electron and magnetic contributions to the specific heat. The lattice contribution for a dielectric solid can be expressed referring at the Debye Model in the low temperature approximation:

$$c_r(T) = \frac{12\pi^4 N_A k_B}{5}\left(\frac{T}{\Theta_D}\right)^3 \tag{4.5}$$

where k_b and N_A are, respectively, the Boltzmann constant and the Avogadro number. The constant Θ_D represents the Debye temperature, a parameter characteristic of the material.

The corresponding heat capacity can be written as:

$$C(T) = \beta\frac{m}{M}\left(\frac{T}{\Theta_D}\right)^3 \qquad \text{with} \quad T < \Theta_D \tag{4.6}$$

where $\beta = 1944$ J/K/mol, m is the absorber mass and M is the molecular weight. As one can easily see, the heat capacity is proportional to the mass and, for $T < \Theta_D$, to the cube of the temperature.

The electronic contribution c_e depends on the conductive or superconductive nature of the material:

$$\begin{aligned} c_e(T) &= \tfrac{\pi^2}{\Theta_D} ZR\tfrac{T}{\Theta_F} \quad \Rightarrow \qquad \text{conductive} \\ c_e(T) &= K_s e^{-2\frac{T_c}{T}} \quad \Rightarrow \quad \text{superconductive} \end{aligned} \tag{4.7}$$

where Z, R and Θ_F are, respectively, the number of electrons in the conduction band for each atom, the gas constant and the Fermi temperature. T_c is the critical temperature

while K_s is a constant which depends on the characteristics of the superconductive material. For conductors c_e is proportional to T and then decreases much more slowly than c_r. For superconductors, when $T < T_c$, c_e decreases exponentially with the temperature. Magnetic materials are dominated by the last term in equation 4.4 which is inversely proportional to T^2.

In order to minimize the global heat capacity, one has therefore to work at very low temperatures and avoid conducting and magnetic materials. The choice to work with dielectric and diamagnetic materials (characterized by a high Debye temperature) allows to have only the lattice contribution to the specific heat, while the electron and magnetic contributions can be ignored. Furthermore, since the Debye temperature depends on the mass number A and on the material density (according to $\Theta_D \propto A^{-1/3}\ \rho^{-1/6}$) low atomic mass and low density shall be preferred. Although a higher atomic number guarantees a higher detection efficiency for electrons and gammas.

4.3 Thermalization process

When interacting with the detector a particle releases its energy into the absorber in the form of ionization and/or excitations. This energy is afterwards downgraded through two main channels: nuclear and electronic.

- **Nuclear channel:** the energy released into the nuclear branch (E_N) is in part converted in vibrational excitations (phonons) and in part it could produce structural defects in the absorber's lattice.

- **Electronic channel:** the energy released in the electronic channel (E_e) is spent to excite electron-hole pairs (e/h pairs). The impinging particle is slowed down in few μm (heavy particles) or mm (electrons) after its interaction into the crystal absorber. Along its path it produces many e/h pairs, with, at the beginning, very high spatial density and energy. These charge carriers interact with each other and spread very quickly in the crystal. As soon as an the equilibrium is reached, they undergo their final degradation interacting with the lattice: these produce phonons. In this process a large fraction of the initial pairs energy is transferred to the lattice as vibrational phonons but also other processes could occur. Indeed, a fraction of this energy instead of being converted into crystal lattice excitations can leave the crystal or can be stored in stable or metastable states. It's possible to have:

  - **radiative recombinations** of e-h couples with the escape of the emitted photons
  - **non-radiative recombinations** that take too much time compared to signal development

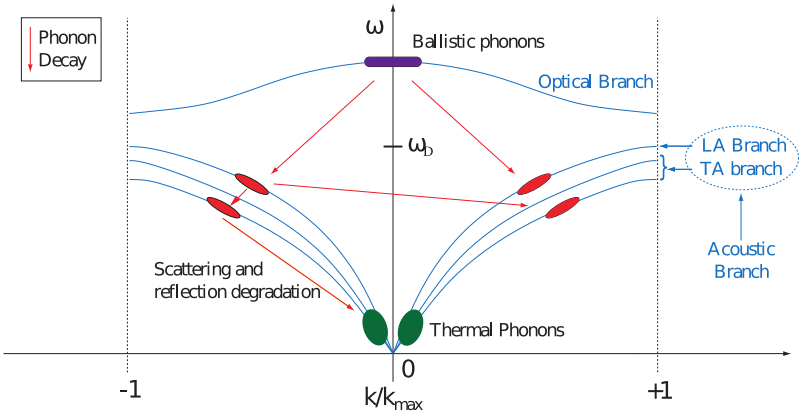

Figure 4.3: A thermal model for the phonons thermalization. The abscissa k is the module of the crystal momentum, a momentum-like vector quantum number associated with electrons in a crystal. There are two types of phonons: acoustic and optical. The acoustic phonons correspond to sound waves in the lattice and are divided in longitudinal and transverse acoustic phonons (respectively, LA and TA phonons).

– **trapping** of electrons and holes in the states created by an impurity defects in the lattice

The fraction of the energy that can leave the crystal (i.e. photons) can be very useful because it can give important information on the nature of the interacting particle (Chapter 8).

In order to understand the phonons thermalization processes inside the crystal absorber it is useful to consider the mono-dimensional representation of the phonon dispersion curves (Figure 4.3). The e/h pair recombination process across conduction and valence bands, produces high energy and low momentum phonons in the optical branch. Optical phonons decay in the Acoustic Branch in a very short time (10 ÷ 100) ps. The energy and momentum are conserved and two phonons, each having half of the energy of the initial particle (of the order of the Debye energy) and opposite momentum, are produced. Therefore the final result is a phonon system, mainly belonging to the Acoustic Branch, and having the energy of the order of $E_D = \hbar\,\omega_D$ (where ω_D is the Debye cutoff frequency of the crystal). This energy is much higher than the average energy of thermal phonons at the bolometer working temperature (at T = 10 mK, the average energy is $< E > \simeq \mu$eV) so that new phenomena of phonon energy degradation can occur and the two produced phonons become thermal phonons.

Since fast (ballistic) and thermal phonons have separated development times, two kind of phonon sensor have been conceived:

- ballistic phonon sensor, used to detect (athermal) phonons at their first interaction

with the crystal surface interface

- thermal phonon sensor, used to detect thermalized phonons (e.g. thermistors)

4.4 The phonon sensor

The phonon sensor is a device able to collect phonons produced inside the absorber and convert them in an electrical signal. In the case of thermal phonons, this device is usually realized with a thermistor whose resistance, as a function of temperature, has a steep slope. In this way a little variation of temperature can generate a significant and measurable variation of resistance. The sensors most commonly used nowadays can be divided into two main classes: semiconductor thermistors and transition edge sensors (TES). These kind of sensors are usually characterized by their logarithmic sensitivity A, which describes the sensor capability of transforming a small temperature increase in a significant resistivity variation. This parameter is defined as:

$$A = \left| \frac{d\ ln\ R(T)}{d\ ln\ T} \right| \tag{4.8}$$

The value of the sensitivity is typically in the range $(1 \div 10)$ for semiconductor thermistors and in the range $(10^2 \div 10^3)$ for TES.

4.4.1 Semiconductor thermistor

This type of sensor is intrinsically slow and is sensitive mainly to thermal phonons. For these reasons it can only give information about system at thermal equilibrium: it acts as a temperature sensor. Normally the semiconductor thermistors consist of a small Ge or Si crystal with a doped region. An effective technique used for fabricating such devices, with an uniform dopant distribution, is the Neutron Transmutation Doping (NTD) [67].

A doped semiconductor near absolute zero can behave either as insulator or as a metal, according to the concentration of dopant atoms implanted in it, which trim the conduction mechanism. If this number is greater than the critical concentration N_c the device has a metallic behavior. The region near this concentration is called metal-insulator transition region (MIT). At temperature $T < 10K$, the conduction is due to the migration of charge carriers from an impurity site to another. When the donor concentration is increased, the wave function of the external electron of the donor atom overlaps with the external electron wave function of the neighboring atoms. In this situation the electrons are not localized and the conduction happens by electrons jumping from a donor site to another without using the conduction band. This mechanism is called hopping mechanism (Figure 4.4). This migration is due to quantum-mechanical tunneling through the potential barrier which separates two dopant sites. This conduction is activated by phonons absorbed into the

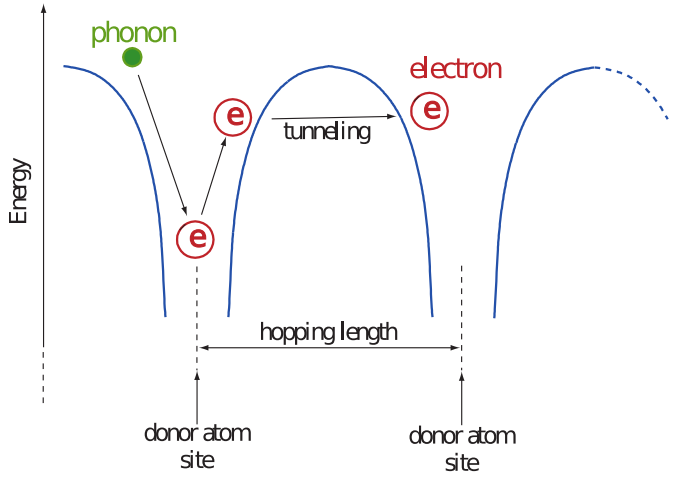

Figure 4.4: Representation of the hopping conduction mechanism.

sensor. The phonon assisted tunneling of localized electrons between different sites depends on hopping length (the mean distance between two contiguous sites) which increases with the decreasing temperature. If T << 10K and if the doping concentration is slightly lower than N_c, the resistivity is strongly dependent on the temperature. So, in order to obtain optimized phonon sensors, one chose to operate semiconductor thermistor slightly below the MIT region. Under these conditions the main electric conduction mechanism is the Variable Range Hopping (VRH) described by Sir N. F. Mott [68]. Here the carriers can migrate also in far sites if their energy levels are located in a narrow range around the Fermi energy.

In the case of VRH the resistivity depends on the temperature in the following way:

$$\rho(T) = \rho_0 e^{\left(\frac{T_0}{T}\right)^{\gamma}} \qquad with \qquad \gamma = \frac{1}{d+1} \tag{4.9}$$

where ρ_0 and T_0 are parameters depending on the doping concentration, and where d is the dimensionality of the phase space of the system. For a three-dimensional system, considering the Mott Model, one has d = 3 and $\gamma = 1/4$.

For a NTD thermistor the sensitivity parameter A takes the following form:

$$A = \left|\frac{d\ ln\ R(T)}{d\ ln\ T}\right| = \gamma\left(\frac{T_0}{T}\right)^{\gamma} \tag{4.10}$$

4.4.2 Transition Edge Sensor

A transition-edge sensor is a thermometer made from a superconducting film operated across its transition temperature T_c. The incident phonons are absorbed directly and the temperature of the electron system in the film raise. If the detector is biased in

its superconducting-to-normal transition, this energy deposition results in a macroscopic resistance change. TES are intrinsically fast and sensitive also to athermal phonons. However, given the physical principle on which TES are based, their sensitivity is limited to a very narrow temperature range.

4.5 Detector operation

In all the measurements with macro-bolometer done during my PhD, I have used semiconductor thermistors so in this section and in the following I will focus only on electronics for this kind of phonon sensor. Detailed informations on TES can be found in [69].

In order to obtain the best performance with semiconductor thermistors a proper biasing circuit is needed. As it is shown in Figure 4.5, the bias current $I_{bol} = I_{BIAS}$ is supplied by means of a voltage generator closed on a load resistor R_L in series with the thermistor (R_{bol}), whose resistance is negligible in comparison to R_L ($R_L >> R_{bol}$).

Fixed a working point by forcing a bias current (Figure 4.5), across the thermistor there is a voltage drop $V_{bol}(T) = I_{BIAS}R_{bol}(T)$. This voltage drop causes a power dissipation $P = I_{BIAS}V_{bol}$ with a consequent temperature rise. At this point the thermistor resistance decreases until the electrical power dissipation becomes equal to the thermal power flowing from the detector to the heat sink. Now a thermal equilibrium is reached and the absorber temperature is given by

$$T_b = T_0 + \frac{P}{G} \tag{4.11}$$

where G is the thermal conductance between the detector and the heat sink maintained at the temperature T_0. This phenomenon makes the V-I characteristic curve (also named volt-amperometric characteristic or load curve) deviate from the linearity and, above a certain value, bias current leads to a non-ohmic behavior. This behavior is very usual in bolometric technique and is often referred to as Electrothermal Feedback (Figure 4.5). For a given bias current, the static resistance is simply the ratio V_{bol}/I_{bol} while the dynamic resistance is the tangent at the V-I curve in the point (V_{bol} , I_{bol}).

The working point of the thermistor is a particular point on the load curve set by the bias voltage. The optimal working point is the one where the ratio of signal amplitude to noise level is maximized. In practice the optimal working point is found approximately by scanning the bias voltage in steps and selecting the value for which the signal amplitude is maximized.

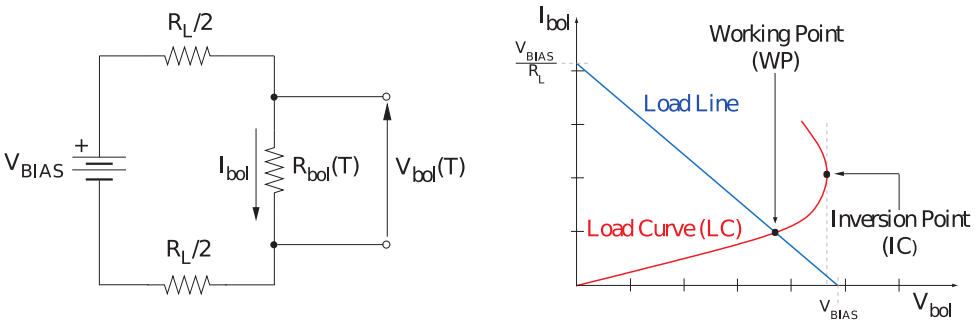

Figure 4.5: Electric scheme of the biasing system used for the read-out of a thermistor. If $R_L >> R_{bol}$ the thermistor biasing system (V_{BIAS} plus R_L) can be modeled as an ideal current generator, therefore the current I_{bol} turns out to be independent on the value of R_{bol}.

4.6 Noise

The energy resolution of a bolometric detector is limited by the noise sources. These sources can be classified in two main categories:

- **intrinsic noise:** it is strictly dependent on the physical characteristics of the absorber and of the sensor. This is an unavoidable source of noise and sets the lowest reachable theoretical limit for the energy resolution (ΔE_{MAX})
- **extrinsic noise:** it accounts for all the noise sources dependent on the experimental set-up and dominates the energy resolution. In this category are included the noise due to the cryogenics system, to the electronics read-out, to the electromagnetic interferences and to the mechanical microphonic noise.

The two main contributions at the intrinsic noise are:

- **Johnson noise:** Every resistance R working at a temperature T_b generates a white noise having a power spectrum given by:

$$e_R = \sqrt{4 k_B R T_b} \tag{4.12}$$

  In addition to Johnson noise associated with the sensor also the one due to the load resistors must be taken into account. The scheme in Fig. 4.5 shows, indeed, that the sensor is biased using a R_L load resistance that is, in general, at a temperature T_L different from T_b (for instance, at room temperature, as in most of the devices described in the following chapters). Therefore the Johnson noise of the load resistance R_L has to be taken into account, but it is possible to demonstrate that this can

be made negligible when compared to the detector noise; in fact the load resistance contribution to the detector noise, e_{det}, is:

$$e_{det} = e_{R_L}\left(\frac{R}{R_L+R}\right)^2 = \sqrt{4k_B R_L T_L}\left(\frac{R}{R_L+R}\right)^2 \tag{4.13}$$

This contribution can therefore be reduced by choosing a large enough value for R_L.

$$\frac{e_{det}}{e_R} \simeq \frac{e_{R_L}}{e_R}\left(\frac{R}{R_L}\right)^2 = \frac{R}{R_L}\cdot\frac{T_L}{T_b} \tag{4.14}$$

- **Thermodynamic Noise:** in the case of complete energy thermalization, the intrinsic energy resolution is limited by the thermodynamic fluctuations of the number of thermal phonons exchanged with the heat bath through the conductance G. This produces energy fluctuations and therefore temperature fluctuations in the absorber, i.e. an intrinsic detector noise. A very naive evaluation of the expected contribution can be obtained on pure statistical grounds as follows. The number of phonons contained in the absorber at thermal equilibrium is:

$$N = \frac{E}{\epsilon_a} = \frac{C(T)\cdot T}{k_B\cdot T} = \frac{C(T)}{k_B} \tag{4.15}$$

where the mean phonon energy ϵ_a is equal to $k_B \cdot T$ and E is the internal energy of the absorber. If Poisson statistics is assumed ($\Delta N = \sqrt{N}$), then it is possible to estimate the fluctuations of the internal energy of the absorber as:

$$\Delta E = \Delta N \cdot k_B \cdot T = \sqrt{N}\cdot k_B \cdot T = \sqrt{\frac{C(T)}{k_B}}\cdot k_B \cdot T = \sqrt{k_B \cdot C(T)\cdot T^2} \tag{4.16}$$

Such a result is surprisingly in agreement with the one obtained using thermodynamic considerations. A detailed calculation of the noise due to intrinsic sources shows that a dimensionless factor F (Fano factor) has to be introduced as a multiplier for Eq. 4.16 in order to take into account possible correlation effects among the events ($0<F<1$). The F value depends on the details of the temperature sensor, of the thermal conductance and of the heat capacity temperature dependences.

According to this last equation, the energy resolution of a bolometer is independent of the deposited energy E, so, for example 1 kg of TeO_2 crystal operating at 10 mK could measure energy deposition of the order of few MeV with a resolution of in the range $(20 \div 100)$ eV, more than two order of magnitudes better than conventional detectors.

The thermodynamic fluctuations of the crystal described above represent the ultimate limit to the noise obtainable in practical applications. Currently they give a negligible contribution to the measured noise in practical situations, when compared to the noise coming from the electronics and the cryogenic apparatus (extrinsic noise). The dominant noise contribution comes from the vibrations of the cryogenic apparatus. These vibrations are transmitted to crystals and wires producing two different types of noise. The crystal vibrations generates an energy dissipation that in turn changes the temperature. These temperature instabilities have a frequency spectrum similar to the signal one, and then they are the most dangerous source of noise. The wires vibrations change the wire-wire capacitance and the wire-ground capacitance, generating the so called microphonic noise. A quantitative evaluation of the vibrational noise contributions is difficult, and it strictly depends on the cryogenic setup and on the detector assembly. These vibrations are anyway reduced hanging the detector to the cryostat by means of a spring, and mechanically decoupling the cryostat from the outer environment.

4.7 Read-out, DAQ and analysis technique

In this section I will describe the read-out, the data acquisition system and the analysis techniques used in measurements done in hall C of LNGS and described in Chapters 7, 8 and 9. These are very similar to those used in Cuoricino and that will be used for CUORE.

The thermistor read-out [70] was performed via a preamplifier stage, a second stage of amplification and an antialiasing filter (a 6 pole roll-off active Bessel filter 120 db/decade [71]) located in a small Faraday cage. The ADC was a NI USB device (16 bit 40 differential input channels). For each triggered signal the entire waveform (*raw-pulse*) is sampled, digitized and acquired for the off-line analysis. Since all the relevant parameters (including the amplitude) of the triggered signals are evaluated off-line, a particular care has to be dedicated to the optimization of the signal filtering and digitalization. In the case of our bolometers, signals are quite slow, characterized by a rise-time of the order of few ms and a decay-time of hundreds of ms (determined by the crystal heat capacity and by its thermal conductance toward the heat sink). Consequently the sampling rate typically used for the signal is 1-4 kHz, on a time window of 200-2000 ms. A 'typical' pulse for a 'big' crystal is reported in Figure 4.6. The Bessel filter acts mainly as antialiasing filter, to avoid spurious contributions in the sampled signal. Generally it is preferred to fix its cut-off frequency at the lowest value that do not reduce the signal to noise ratio (i.e. to obtain the best results in terms of energy resolution). This results to be a frequency of the order of 10 Hz, which is by far lower than what needed for antialiasing purposes. In the studies presented in Chapter 9 the Bessel cut-off frequency was fixed at 120 Hz in order to exploit the maximum available information in the signal bandwidth.

The off-line analysis aims at determining the pulse amplitude and energy together with

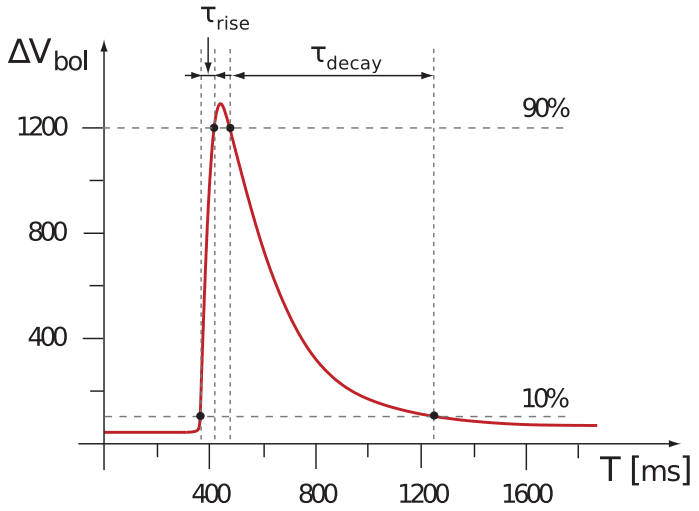

Figure 4.6: Typical thermal pulse. The rise time is the difference between the time when the signal crosses a low threshold (10% of step height) and the time when the signal crosses the high threshold (90% of step height).

several pulse shape parameters associated with each raw-pulse waveform recorded by the data acquisition system. Starting from these quantities the physical informations that are relevant for the scientific goals can be extracted.

The first operation consists in the correct evaluation of the pulse amplitude. Since thermal pulses are superimposed to stochastic noise, a simple maximum-minimum algorithm would not give the best achievable resolution. We therefore use the Optimum Filter (OF) technique, based on the approach described in [72]. This algorithm has proven to provide the best estimate of the pulse amplitude and, as a consequence, the best energy resolution. The basic concept is to build a filter that, when applied to the raw-pulse, produces a pulse with the best signal to noise ratio. The filtered pulse is then used to evaluate the signal amplitude. It can be proven that in the frequency domain the OF transfer function H(ω) is given by

$$H(\omega) = K \, \frac{S^*(\omega)}{N(\omega)} \, e^{-j\omega t_M} \tag{4.17}$$

where S(ω) is the Fourier transform of the ideal thermal signal (reference pulse in the absence of noise), N(ω) is the noise power spectrum, t_M is the delay of the current pulse with respect to the reference pulse and K is a proper normalizing factor usually chosen in order to obtain the correct event energy.

The role of the optimum filter is to weight the frequency components of the signal in order to suppress those frequencies that are more affected by noise. It can be seen from Eq. 4.17 that, in order to build the filter, the shape of the reference pulse S(ω) and the

noise power spectrum N(ω) must be known. S(ω) is usually estimated by averaging a large number of recorded raw-pulses, so that the noise associated with each of them averages to zero. N(ω) is obtained according to the Wiener-Khinchin theorem by acquiring many detector baselines in the absence of thermal pulses and averaging the corresponding noise power spectra.

Once the pulse amplitude has been evaluated, gain instability corrections are applied to data. Due to the dependence of the detector response on the working temperature, the same amount of released energy can produce thermal pulses of different amplitudes. Gain instabilities are corrected exploiting thermal pulses of fixed energy, produced every few minutes by means of a Si heater resistor attached on the crystal absorber [73]. Finally the amplitude to energy conversion is determined measuring the pulse amplitudes corresponding to fixed calibration lines.

Besides the amplitude, also few characteristic parameters of the pulse are computed by the off-line analysis. These are: τ_{rise} and τ_{decay}, TVL and TVR. The rise-time (τ_{rise}) and the decay-time (τ_{decay}) are determined on the acquired raw-pulse as ($t_{90\%}$-$t_{10\%}$) and ($t_{30\%}$-$t_{90\%}$) respectively (Figure 4.6). TVR (Test Value Right) and TVL (Test Value Left) are computed on the optimally filtered pulse A(t). They are the least square differences of A(t) with respect to the filtered response function $A_0(t)= H(t) \otimes S(t)$. In more detail, the filtered response function $A_0(t)$ is synchronized with the filtered signal A(t), making their maxima to coincide, then the least square differences of the two functions are evaluated on the right (TVR) and left (TVL) side of the maximum on a proper time interval. These two parameters do not have a direct physical meaning, however they are very much sensitive (even in noisy conditions) to any difference between the shape of the analyzed pulse and the response function. Consequently, they are used either to reject fake triggered signals (e.g. spikes) or to identify variations in the pulse shape with respect to the response function.

Part II

TeO_2 0νDBD

Chapter 5

Cuoricino

The Cuoricino experiment was a ^{130}Te-based search for 0νDBD. It consisted of an array of 62 tellurium dioxide (TeO_2) bolometers with a total mass of 40.7 kg. It was operated at the Laboratori Nazionali del Gran Sasso from early 2003 to June 2008. The Cuoricino detector was built as a prototype for the CUORE experiment, which will have 19 Cuoricino-like towers and is presently under construction at LNGS.

Cuoricino allowed to reach the best sensitivity on 0νDBD of ^{130}Te ever obtained [74] and it was an important benchmark for CUORE. In addition to providing important information on the underground operation of a large array of bolometers, Cuoricino allowed to study in detail the different sources of spurious counts that limit the sensitivity of bolometric experiments. Some of these sources, due to environmental radioactivity, muons and neutrons, can be reduced with a careful design of the experimental setup (as was done for CUORE) while others require special care in preparing the detector (screening and treatment of materials). In particular Cuoricino has given strong indications of the existence of an important contribution to the background in the 0νDBD region due to surface contamination of the setup materials. Unfortunately, such contributions have been found (in testing with bolometric small array dedicated to this purpose) very difficult to reduce.

In this chapter, after a short description of the experimental setup and of the 0νDBD result obtained by Cuoricino, I will focus the attention on the Cuoricino background and in particular I will describe the Monte Carlo simulation that I have done to study the background induced by muons.

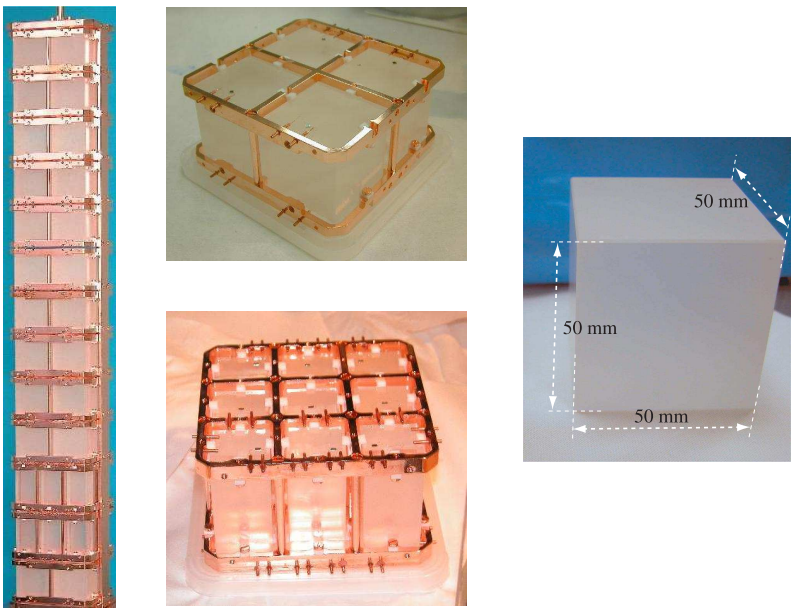

Figure 5.1: Cuoricino: on the left the 13 floors of the tower, in the center a floor of 4 crystals and one of 9 crystals. On the right the single 5×5×5 cm^3 crystal.

5.1 Experimental Setup

Cuoricino crystals were arranged in a tower made of 13 floors, 11 with four 5×5×5 cm^3 crystals and 2 with nine 3×3×6 cm^3 crystals (Figure 5.1). Each crystal was operated as a bolometer able to detect an energy deposition by recording the increase of temperature with a neutron transmutation doped Ge thermistor (Section 4.4.1).

In the case of 0νDBD, the summed energies of the electrons emitted would result in a mono-energetic peak at the transition energy of 2527.518 ± 0.013 keV for ^{130}Te [76].

Cuoricino crystals can be divided into four main groups according to their mass and isotopic abundance:

- big crystals: 44 bolometers, $5 \times 5 \times 5$ cm^3 in size and 790 g in mass;
- small crystals: 14 bolometers, $3 \times 3 \times 6$ cm^3 in size and 330 g in mass;
- ^{130}Te-enriched crystals: 2 bolometers, $3 \times 3 \times 6$ cm^3 in size and 330 g in mass, grown with ^{130}Te enriched material;
- ^{128}Te-enriched crystals: 2 bolometers, with the same size and mass of the ^{130}Te-enriched ones but grown with ^{128}Te enriched material.

The ^{130}Te-enriched crystals have a ^{130}Te content corresponding to an isotopic abundance of 75% [77]. On the contrary, the ^{130}Te content of 128-enriched crystals is so low that they were not considered for the 0νDBD analysis.

The detector tower was mounted inside the inner vacuum chamber (IVC) of the dilution refrigerator (for more details see Appendix) and thermally linked through a cold finger to the coldest point of the dilution refrigerator, at a temperature of about 10 mK. The detector was surrounded by several radiation shielding layers (see Figure 5.2). Directly above the detector, inside the cryostat, there was a 10 cm thick layer of low-activity "Roman" lead (from a sunk ancient Roman shipwrecks). Around the detector there were several layers of thermal shields and a 1.2 cm thick cylindrical Roman lead shield. The thermal shields were made from electrolytic copper for, at least, 1.5 cm in thickness. Outside the cryostat was a 10 cm low-activity lead shield and a 10 cm standard lead shield. The cryostat and shields were surrounded by a Plexiglas box flushed with clean N_2 from a liquid nitrogen evaporator to avoid radon, followed by a 10 cm borated polyethylene neutron shield. A top lead shield was located about 50 cm above the top plate of the cryostat. The entire setup was enclosed in a Faraday cage to reduce electromagnetic interference. The assembly is shown in Figure 5.2. A more detailed description of the detector can be found in Ref. [36].

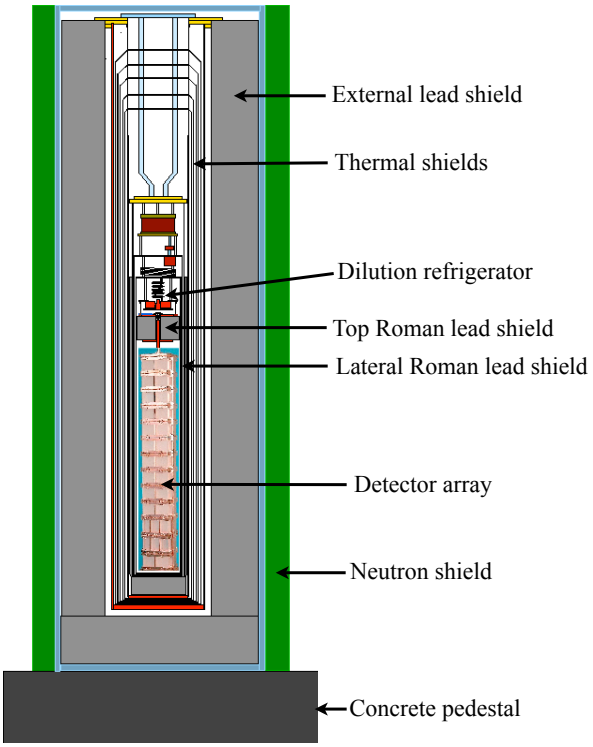

Figure 5.2: The layout of Cuoricino showing the tower, the various heat shields, and the external shielding

5.2 Cuoricino TeO_2 bolometers

The bolometric technique allows the use of a wide variety of 0νDBD candidates. The choice of the ^{130}Te comes from a good compromise between different requirements that characterize a 0νDBD experiment. First of all the high natural abundance that allows to reach an high sensitivity even without enrichment which is expensive and difficult, then the favorable Nuclear Factor of Merit of ^{130}Te. The main disadvantage of this isotope is the relatively low Q-value, as it lies between the Compton edge and the photoelectric peak from ^{208}Tl and therefore still in the region where environmental gamma rays are important.

Once decided the isotope, the choice of which compound to use as absorber falls on tellurium dioxide (TeO_2). This choice is motivated by the favorable characteristics of these crystals if compared with Te ones that were the other possible option considered in the past:

- **Debye temperature**: TeO_2 Debye temperature is higher than pure tellurium crystals. At the same temperature TeO_2 crystals have a lower specific heat and then higher signal
- **Mechanical properties**: pure tellurium crystals do not have good mechanical properties and after few thermal cycles break. TeO_2 crystals have rather good mechanical properties and is possible to grow large crystals
- **Radioactivity**: TeO_2 crystals have a good intrinsic radiopurity (< 1 pg/g in ^{232}Th and ^{238}U)

The Cuoricino single module is an array of 4 (or 9) TeO_2 crystals (i.e. the single floor of the tower shown in Figure 5.2), each provided with its own sensors. The design of the single module must satisfy stringent requirements concerning mechanical properties, thermal performance and radioactivity constraints. Crystals are enclosed in a pair of copper frames which serve both as mechanical supports and thermal bath for the detectors. The two frames are connected to each other by four small columns, also made of copper. The crystals are connected to the copper frames by small Teflon supports that represent the weak thermal conductance towards the heat sink and compensate the different thermal contractions of TeO_2 and copper. The NTD sensors are attached to the crystals using Araldit Rapid epoxy glue. Since a flat glue deposition would cause the sensor to detach from the crystal surface because of differential thermal contractions, the glue is deposited in nine separate spots, with a diameter of 0.7 mm each. The same gluing technique is used to glue on each detector the Si resistor (see section 4.7) used to feed the crystal with heater pulses. Electrical connections for both the NTD sensor and the Si resistor are made

Crystal Type	^{130}Te Mass [g]	Exposure Run II [kg(^{130}Te)·y]	Exposure Run I [kg(^{130}Te)·y]
big	217	15.80	0.94
small	91	2.02	0.094
^{130}Te-enriched	199	0.75	0.145

Table 5.1: Cuoricino crystal information and statistics.

with two 50 μm diameter gold wires, bonded to a metallic layer on the surface of the two chips.

5.3 Cuoricino data

Cuoricino data taking started in March 2003. In November 2003 the tower was warmed up at room temperature to perform maintenance operations and to recover lost connections. Data taking restarted in May 2004 with the full operation of all detectors and lasted until June 2008. The data are then separated into two runs (RUN I and RUN II). The total exposure is 19.75 kg·y. The data collection is summarized in Table 5.1.

Evaluating the energy resolution on the ^{208}Tl line of ^{232}Th source used in the calibration measurements, a value of ∼7 keV was obtained averaging the results of the 5×5×5 cm^3 crystals, while a value of ∼9 keV was obtained for the 3×3×6 cm^3 crystals.

In order to evaluate the number of ^{130}Te 0νDBD events the signal efficiency (i.e. the probability that a 0νDBD event is detected) must be accurately determined. There are two main sources of inefficiencies, one "physical" that can be computed by simulations, and the other "instrumental" that must be measured from the data. The mechanism of "physical" efficiency loss is the escape of a fraction of the 0νDBD energy from the source crystal. Mechanisms for the "instrumental" efficiency loss are: the pulse-shape cut, the anti-coincidence cut and an incorrect assignment of the energy of the signal (mainly due to noise and pile-up). The overall signal efficiency is: (82.8 ± 1.1)% for the Cuoricino big crystals and (79.7 ± 1.4)% for the small and the ^{130}Te-enriched ones. Details on the evaluation of the signal efficiency and analysis technique can be found in [74].

No evidence of a 0νDBD signal is found in the analyzed data (Figure 5.3). By applying a maximum likelihood procedure we obtain a 90% lower limit for the lifetime set to:

$$T_{1/2}^{0\nu}(^{130}Te) \geq 2.8 \times 10^{24} \quad years \quad (90\% C.L.)$$

The evaluation of an upper limit for the effective Majorana mass is strictly related to the Nuclear Matrix Elements (see Section 2.1.1). Using the latest calculations by different

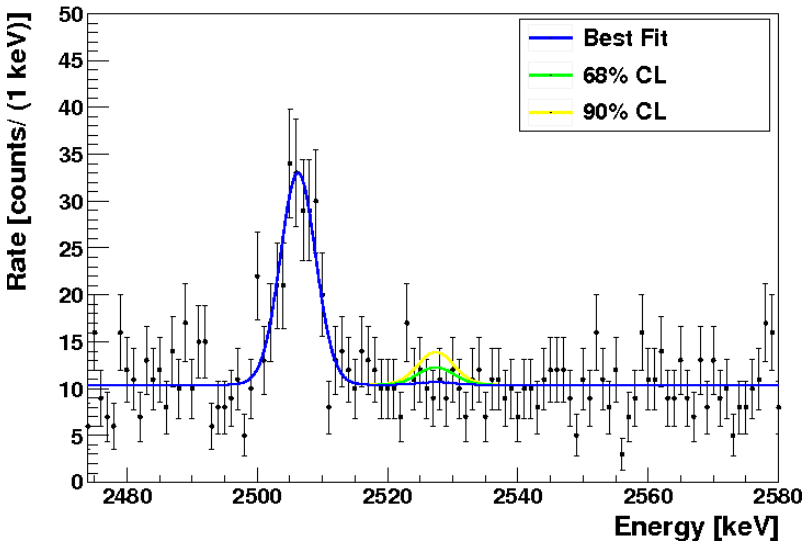

Figure 5.3: Best fit, 68% and 90% confidence intervals for the total statistics (RUN I+RUN II) superimposed on the Cuoricino sum spectrum of the three groups of crystals (each scaled by efficiency and exposure) in the 0νDBD region.

authors [26, 27, 28, 29] the lower limit on the effective Majorana mass fixed by Cuoricino is in the range:

$$\langle m_\nu \rangle < 0.3 - 0.7 \quad eV$$

5.4 Cuoricino background

Cuoricino not only provided the best sensitivity on 0νDBD of ^{130}Te. It allowed also to study with high statistic the background in the bolometric technique showing the existence of a dominant contribution due to degraded α particles.

In Figure 5.4 is reported Cuoricino spectrum in the energy region of the expected ^{130}Te decay (2528 keV). The γ lines of ^{214}Bi (2488 keV), ^{60}Co (2505 keV) and ^{208}Tl (2615 keV) can be seen. Among these isotopes, only ^{208}Tl can give a significant contribution to the background in the region of ^{130}Te decay through multi-Compton events. Comparing the intensity of ^{208}Tl with the other low-energy gamma, it was inferred that this line can be ascribed to contaminations that are far from the detector (for example, in the cryogenic setup) and thus can be suppressed through a proper shield.

Above 2615 keV, a flat continuum with several α peaks is clearly visible (Figure 5.4 and 5.5). In order to identify the sources of these contaminations, two important tools can be used: the coincidence analysis and the peak shape analysis.

The shape of the peaks can give informations about the location of the contaminants.

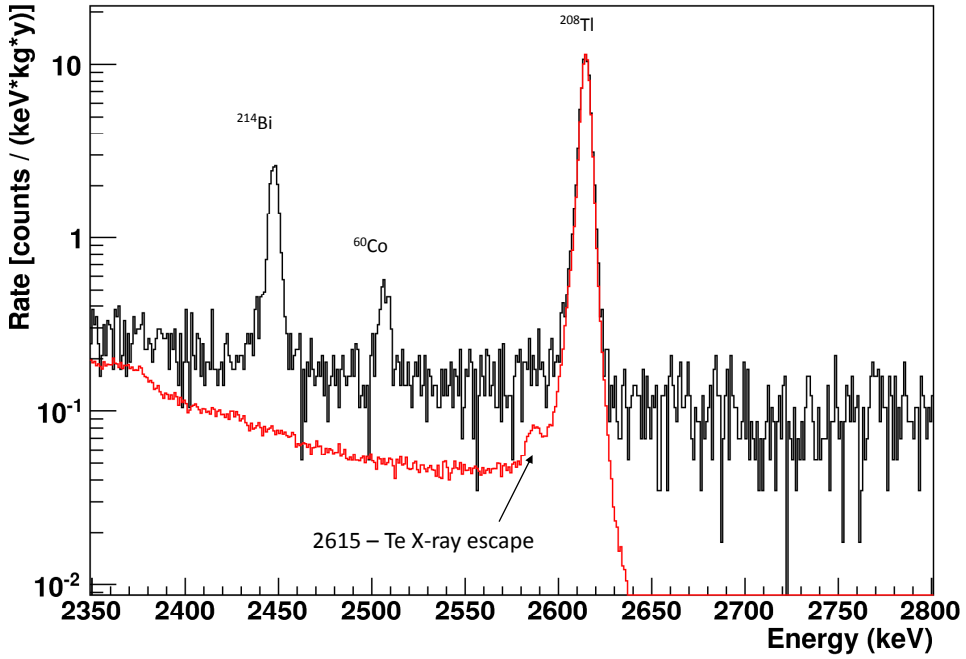

Figure 5.4: Cuoricino anti-coincidence spectrum near the 0νDB. In black the total background of all the Cuoricino detectors. In red spectrum of all Cuoricino detectors during calibration measurements. The 2 spectra are normalized at the 2615 keV (^{208}Tl γ-line).

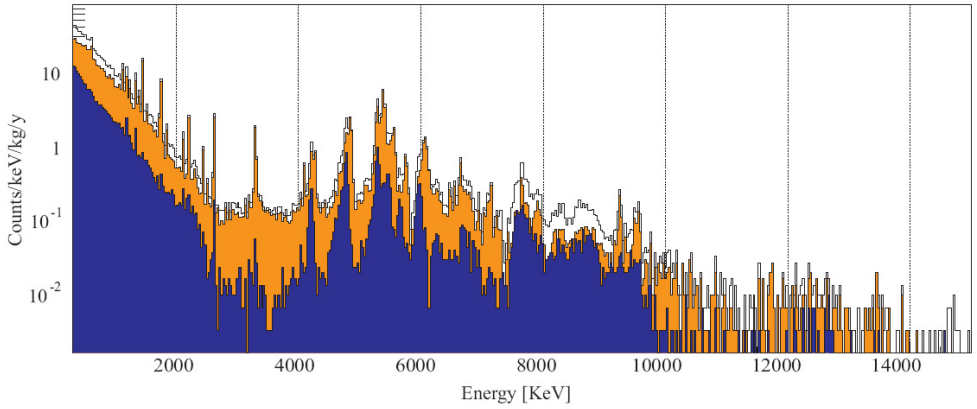

Figure 5.5: Cuoricino background. Black line: total spectrum (all the events are counted), orange filled: anticoincidence spectrum (one detector hit), blue filled histogram refers to coincidence events (two detectors hit per event).

For example, an α decay inside the bulk of the crystal gives rise to a sharp Gaussian peak at the Q-value, since both the particle and the nuclear recoil energy are deposited inside

the crystal. A contamination in a surface layer gives rise to a Gaussian peak at the α or recoil energies. Finally, a deeper surface contamination of the material facing the detector gives rise to a flat continuum, because the α particle can loose a variable amount of energy in the material [75].

The comparison between the coincidence spectrum (events where two crystals are hit within the same time coincidence window) and anti-coincidence one (events where only one detector is hit) helps in tracking back the origin of the events. For example, a contamination in the surface of the material facing the detector produces events only in the anti-coincidence spectrum. On the other hand, a contamination on a crystal surface can produce an event in the coincidence spectrum (for example, the nuclear recoil can be absorbed in a crystal and the α particle in another one). While in Cuoricino the fraction of coincidence events is relatively small in CUORE the large mass and the high granularity of the array will allow to have a relevant reduction of the counting rate by applying an anticoincidence cut.

Thanks to the peak shape analysis and the comparison between the coincidence and the anti-coincidence spectrum, it was possible to identify the peaks above 4 MeV, which were mainly attributed to surface contaminations of the crystals with isotopes belonging to the ^{238}U and ^{232}Th chains.

The origin of the flat continuum between 3-4 MeV is still a delicate issue:

- a large fraction of the flat continuum must be originated outside the crystals, since the amount of coincidence between 3-4 MeV is very small (for details on surface contaminations see Chapter 3.4.3)
- Monte Carlo simulations demonstrated that neutrons don't give appreciable contributions in this region
- ^{238}U and ^{232}Th contaminants are excluded since the rate of the low energy γ peaks is very low
- bulk contaminations in the small components of the detector (thermistors, heaters, PTFE holders, glue, Au wires) are excluded, thanks to independent radioactive measurements (Chapter 7)

Given all these hints, the most likely guess is that the flat continuum between 3-4 MeV can be ascribed to interactions of degraded α coming from the surfaces of the copper frames or of the crystals. Releasing a variable fraction of their energy in the absorber, these particles generate events which cannot be traced back to a specific decay by their signature.

Extending to lower energies, the flat continuum can give significant contributions to the background counting rate in the 2.5 MeV region, thus a reduction of these contaminations is needed.

In Table 5.2, a summary of the results of the Cuoricino background analysis is reported. From these data, one can infer that the most important sources of background come from the surfaces of the copper. In Chapter 7, a brief summary on the R&D dedicated to the reduction of these contaminations is reported.

Material	Isotopes	Energy range		
		^{208}Tl	$Q^{0\nu}(^{130}Te)$	3-4 MeV
TeO_2 surface	^{238}U and ^{232}Th	-	$(10 \pm 5)\%$	(20 ± 10) %
Cu surface	^{238}U and ^{232}Th	15%	$(50 \pm 20)\%$	(80 ± 10) %
Cryostat Cu shield	^{232}Th	85%	$(30 \pm 10)\%$	-

Table 5.2: Summary of the analysis of the data of Cuoricino.

5.5 Muon Veto

One possible contribution to the flat background above and below 2615 keV is due to cosmic rays. Although this is not deemed to be a major source of background, a dedicated measurement was performed to evaluate the real contribution to the background. For this reason ten plastic scintillator detectors were installed at the Cuoricino site and operated during the final 3 months of the experiment [78]. I took care of the comparison of the result obtained with this measurements and Monte Carlo simulations (GEANT4) to verify the goodness of the simulations and then extend the results to CUORE.

5.5.1 Muon Detector Setup

An array of ten large plastic scintillators placed outside of the Faraday cage, which surrounds the detector, was used to tag muons. The total sensitive surface area of the scintillators was about 3.67 m^2.

The scintillators were deployed to tag as many as possible of the muons hitting the lead shields while accounting for both the angular distribution of the incoming muons and the geometric constraints from existing structures. A simple Monte Carlo simulation reproducing the muon flux measured by MACRO [63] was used to optimize the placement of the counters. The arrangement of the scintillators is shown in Figure 5.6.

The scintillation counters were obtained from previous experiments so they have different shapes and dimensions. The thickest were operated alone. For these scintillators, the energy released by a through-going minimum ionizing particle was greater than 8 MeV, which was well above any naturally occurring gamma or beta background as well as most naturally occurring alpha lines; therefore, muons may be discriminated from background by simply applying cuts on the energy. The thinner were about 3 cm thick and were

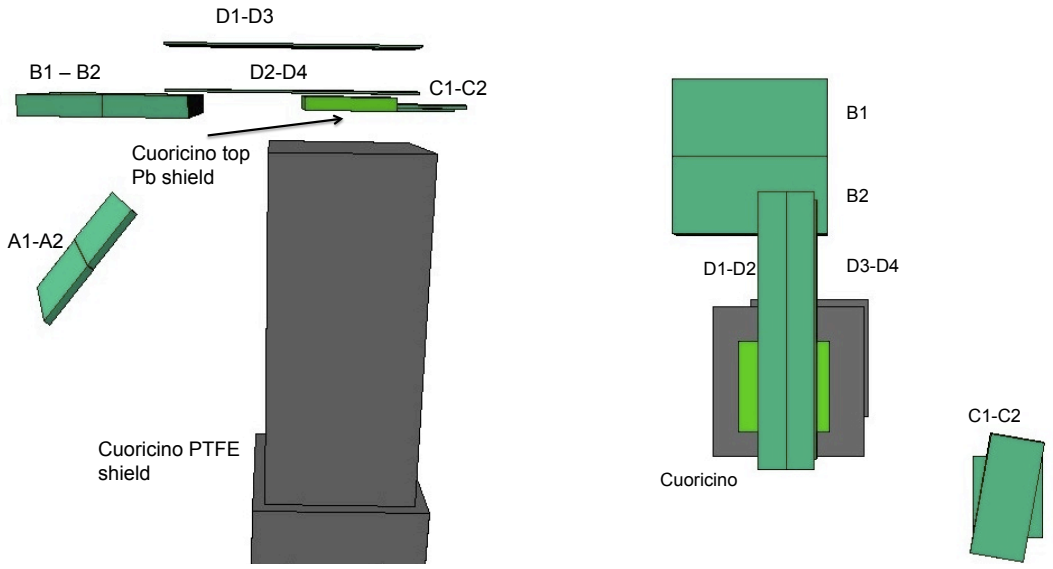

Figure 5.6: The drawings show the positions of the scintillators around Cuoricino (left: side view, right: top view): the large, dark grey box is the neutron shield placed around the detector. The smaller objects are the scintillators and the top part of the lead shield. The support structures for the scintillators have been omitted.

operated in pairs. For each pair, one scintillator was stacked on top of the other and a trigger signal was generated only when they were hit in coincidence (within 120 ns of each other).

5.5.2 Detector Operation and Performance

Figure 5.7 shows the energy spectrum acquired by one of the scintillators. Two regions are evident: a low energy background region and a broad peak at higher energies. The low energy background is due to radioactivity, dark noise, and muons that hit the scintillator, whereas the higher energy peak is mostly due to cosmic ray muons.

In order to determine the overall efficiency of the setup for tagging muons in coincidence with a Cuoricino bolometer event, the intrinsic detector efficiency and the efficiency of the software cuts were combined for each detector. The individual efficiency of the scintillators was generally greater than 95% (for a detailed description on how this efficiency was evaluated see [78]). This information was then included in a Monte Carlo simulation precisely reproducing the Cuoricino geometry, the positions of the scintillators, and the distribution of the muon flux. The simulation is described in more detail in Section 5.5.4.

The total trigger rate of the muon detectors was ∼14 mHz with no cuts applied, or ∼4 mHz with energy threshold cuts, while the expected signal rate from the simulation was

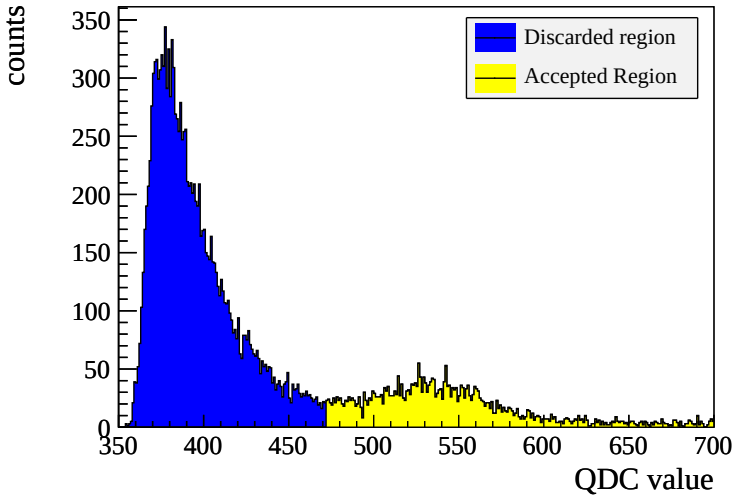

Figure 5.7: Energy spectrum acquired underground at LNGS using detector A1 (Fig. 5.6). The darker region (not used in the analysis) is dominated by low energy background, while lighter region primarily contains muon events.

1.75 mHz. The difference between the predicted and measured rate is due to the fact that the trigger thresholds were kept low in order to maximize the efficiency of muon detection; this resulted in the inclusion of some triggers caused by radioactive decays and dark noise. These spurious muon triggers contributed some background to our measurement through the increased rate of accidental coincidences between the scintillators and bolometers, which was taken into account in the analysis.

5.5.3 Data Analysis

The analysis involved searching for correlations between muon triggers and events in the Cuoricino bolometer array. A coincidence was defined as an event in the muon detector occurring within ±50 ms of a bolometer event. This large window, was chosen based on the time resolution of the bolometer signals (∼30 ms). It did not represent a limiting factor due to the low event rates.

The bolometer spectrum was divided into three energy regions: 200–400 keV, 400–2000 keV, and 2000–4000 keV, as shown in Figure 5.8. The background rate varies by several orders of magnitude over the complete spectrum; therefore, it is useful to treat the high energy region, which contains the Q-value for 0νDBD decay, separately from the lower energy regions where the background is much higher.

In the limit of low rates, the rate of "accidental" coincidences between muon events

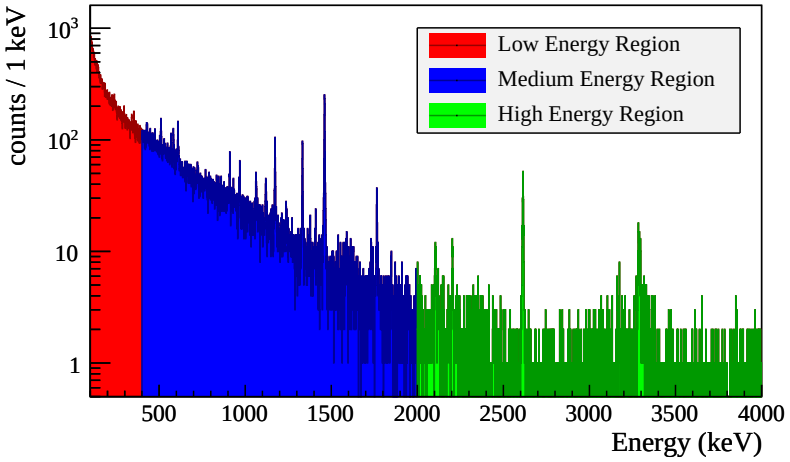

Figure 5.8: Energy spectrum of the Cuoricino background showing the division of energy regions used in the analysis. No bolometer anti-coincidence cut has been applied.

and bolometer events is given by:

$$R_{\text{accidental}} = 2 \cdot R_{\text{bolo}} \cdot R_{\mu} \cdot \Delta T \tag{5.1}$$

where R_{bolo} is the bolometer event rate, R_{μ}=4.01 mHz is the muon rate, and ΔT=50 ms is the width of the coincidence window. Multiplying this rate by the total live time gives the expected number of accidental coincidences, which is compared to the number of measured coincidences in Figure 5.9(a). This figure shows a statistically significant correlation between events in the muon detector and the bolometers.

Limiting the analysis to single-bolometer events (anti-coincidence cut), the number of coincidences between the muon and bolometer events is consistent with the number of expected accidentals, as shown in Figure 5.9(b). We can therefore conclude that the bolometer anti-coincidence cut is very effective at eliminating potential muon-induced backgrounds.

The numbers of expected accidental and measured coincidences shown in Figure 5.9(b) provide an upper limit on the muon-induced contribution to the Cuoricino background. These results are summarized in Table 5.3. The limits were computed by using the Feldman-Cousins method [81] to obtain an upper limit, ν^{up}, on the expected number of muon-correlated signal events. This number was converted into an upper limit on the background rate, R^{up}, in the usual units of counts/(keV·kg·yr) as follows:

$$R^{\text{up}} = \nu^{\text{up}} \cdot \frac{1}{f_{\text{obs}}} \cdot \frac{1}{X} \cdot \frac{1}{\Delta E} \tag{5.2}$$

Here, $X = 3.99$ kg·yr is the total exposure and ΔE is the size of the energy window. The error on the energy window is taken to be on the order of the energy resolution, 7–9 keV

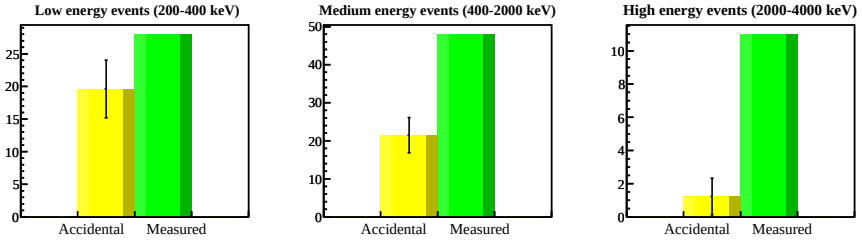

(a) Expected number of accidentals vs. measured coincidences

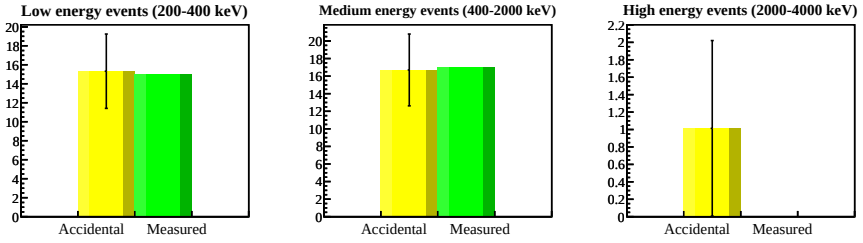

(b) Accidentals vs. measured coincidences with bolometer anti-coincidence cut

Figure 5.9: Comparison of the expected number of accidental coincidences and the number of observed coincidences between the muon detector and bolometer signals. The error bar on the accidentals column represents Poisson fluctuations. Figure 5.9(a) includes all bolometer events in the given energy region, while Figure 5.9(b) only includes bolometer events which pass an anti-coincidence cut (i.e. they do not occur within 100 ms of any other bolometer event).

Energy	$\langle A \rangle$	M	Upper Limits (95% CL)	
			ν^{up}	$R^{\mathrm{up}}/10^{-3}$
Low (200-400 keV)	15.3	15	9.0	83
Mid (400-2000 keV)	16.7	17	10.	12
High (2-4 MeV)	1.01	0	2.3	2.1

Table 5.3: Upper Limits (95% CL) on the contribution of muon-induced events to the Cuoricino background. Limits were computed using the Feldman-Cousins method. $\langle A \rangle$ is the expectation value of the number of accidental coincidences. M is the number of measured coincidences. ν^{up} is a limit on the mean number of observed muon-correlated signal events, while R^{up} gives an upper limit on the rate in counts/(keV·kg·yr).

on average. The factor $f_{\mathrm{obs}} = 13.6 \pm 1.6\%$ is the fraction of the muons producing signal in bolometers that are also observed in the scintillators. It is obtained from simulations by taking the number of muon events which hit the bolometers and the scintillators divided by the total number of generated muon events which hit the bolometers. The uncertainty in f_{obs} is the dominant systematic uncertainty in the conversion from ν^{up} to R^{up}; however, this uncertainty is much smaller than the statistical uncertainty, and has therefore been neglected in computing upper limits. After applying the bolometer anti-coincidence cut, the upper limit on the muon-induced contribution to the Cuoricino background in the 0νDBD region of interest is 0.0021 counts/(keV·kg·yr) at 95% confidence level.

In principle, a muon (or spallation neutron) could produce long-lived ($T_{1/2} \gtrsim 50$ ms) radioactive isotopes which could then decay producing a delayed coincidence signal. Based on the small number of muon events and large background, we do not expect to be sensitive to this effect. Consistent with this expectation, we find no evidence of a delayed coincidence signal. However, due to the poor sensitivity and large number of potential products (each with a different half-life and decay energy), we do not set an upper limit for delayed coincidences with the present data.

5.5.4 Simulation

GEANT4 version 9.2[1] [79] was used to simulate the muon-induced backgrounds in Cuoricino. The LBE (Low Background Experiment) physics list was used. The GEANT4 capability of event-by-event simulation was employed to follow the whole sequence of secondary tracks from the initial interaction to the detector, including the contribution of neutrons generated from muon interactions in the shields. The complete structure of the scintilla-

[1] A known bug affecting the neutron inelastic interactions has been fixed in GEANT4 9.2: http://geant4.cern.ch/support/ReleaseNotes4.9.2.html

tors, external shields, internal shields, and detector geometry was implemented according to the model shown in Figure 5.6. The propagation of particles through the rock overburden was not simulated, but was accounted for as described below.

An independent code was used to simulate the muon energy and angular distribution in the underground laboratory of LNGS. Muons were generated on a 6 m hemisphere in the underground laboratory according to the angular distribution measured by the MACRO experiment [63]. The generated muons were then assigned an energy based on the ground-level energy spectrum for that angle, which was approximated as [80]:

$$\frac{dN}{dE_{GL} \cdot d\Omega} \propto \frac{0.14 \cdot E_{GL}^{-2.7}}{\text{s cm}^2 \text{ sr GeV}} \left(\frac{1}{1 + \alpha \, E_{GL} \cos\theta} + \frac{0.054}{1 + \beta \, E_{GL} \cos\theta} \right), \tag{5.3}$$

where E_{GL} is the energy at ground level, $\alpha = 1.1/115$ GeV, and $\beta = 1.1/850$ GeV. The ground-level energy was then translated into an underground energy based on the formula [80]:

$$E_U = (E_{GL} + \epsilon) \cdot e^{-bX(\theta,\phi)} - \epsilon, \tag{5.4}$$

where E_U is the energy underground, $b = 0.4 \times 10^{-5}\,\text{cm}^2/\text{g}$, $\epsilon = 540.0$ GeV, and $X(\theta, \phi)$ is the thickness times density of the overburden in the given direction. The advantage of this method is that it includes the correlation between the direction and energy of the muons underground. The range of above-ground energies simulated was chosen for each direction such that the underground energies spanned from 1 GeV to 2 TeV, which corresponds to ∼99% of the underground muon flux.

The output of the simulation contained the event number, detector number (scintillator number or bolometer number), hit time, and energy released in the detector. This output was used to produce spectra and scatter plots, taking into account the detector response and analysis cuts in order to reproduce the experimental conditions. A Gaussian smearing of 8 keV (full-width at half maximum) modeled the bolometer resolution.

The Monte Carlo simulation produced the equivalent of about 3.5 years of data ($\sim 8{\times}10^6$ primary muons). In addition to statistics, the simulations were subject to systematic uncertainties: uncertainty in the primary muon flux and spectrum (8%) [62], GEANT4 electromagnetic tracking (5%), uncertainty in the muon-induced neutron yield (40%), and neutron propagation and interaction (20%) [54].

5.5.5 Simulation Results

The analysis of the simulated events was carried out in the same way as for the actual measurements. The spectrum of muon events in the various scintillators appears to be correctly reproduced in simulations. The spectrum of bolometer events was divided into the same three energy regions: 200–400 keV, 400–2000 keV, and 2000–4000 keV.

	Simulation 10^{-3} (counts/(keV·kg·yr))	Measurement 10^{-3} (counts/(keV·kg·yr))
All Events		
Low (200-400 keV)	25.0 ± 0.7	10 ± 7
Mid (400-2000 keV)	7.91 ± 0.14	4.2 ± 1.1
High (2-4 MeV)	1.71 ± 0.12	1.2 ± 0.4
With Bolometer Anti-coincidence Cut		
Low (200-400 keV)	1.84 ± 0.19	< 11
Mid (400-2000 keV)	0.66 ± 0.04	< 1.6
High (2-4 MeV)	0.08 ± 0.03	< 0.29

Table 5.4: Simulated and measured rates of bolometer events in coincidence with the muon detector. Only statistical errors are quoted. Systematic uncertainties are discussed in the text (Sections 5.5.4 and 5.5.3).

Energy	Total 10^{-3} (counts/(keV·kg·yr))	Anti-coincidence 10^{-3} (counts/(keV·kg·yr))
Low (200-400 keV)	184.9 ± 1.9	7.9 ± 0.4
Mid (400-2000 keV)	58.1 ± 0.4	3.58 ± 0.09
High (2-4 MeV)	12.6 ± 0.3	0.53 ± 0.06

Table 5.5: Simulated contribution of muon-induced events to the Cuoricino background. Only statistical errors are quoted. Systematic uncertainties are discussed in the text (Section 5.5.4).

In Table 5.4, the simulated rates of bolometer events in coincidence with the muon detector are reported and compared with data (with and without imposing a bolometer anti-coincidence cut). The measured rates are reported after the subtraction of the expected background from accidental coincidences. In Table 5.5, the simulation results are reported for the total muon-induced background rate in Cuoricino. In the energy region immediately surrounding the 0νDBD Q-value, a value of $(17.4 \pm 1.3)\times10^{-3}$ counts/(keV·kg·yr) was obtained for background induced by muons without any anti-coincidence cut applied and a value of $(0.61 \pm 0.25)\times10^{-3}$ counts/(keV·kg·yr) with the bolometer anti-coincidence cut.

Comparison between simulations and measurements allows to verify the correctness of simulations and to extrapolate the background induced by muons in CUORE (Chapter 6.3.1).

Chapter 6

CUORE

The CUORE detector is an array of 988 TeO_2 bolometers, 750 g each for a total mass of 741 kg, used - as in Cuoricino - for a calorimetric detection of the two electrons emitted in the 0νDBD of ^{130}Te.

In this chapter, after a short introduction on the experimental setup, the reachable sensitivity and the status of the construction, I will focus on the studies of the background since in my PhD I have worked on GEANT4 simulations to evaluate possible sources of background in CUORE and techniques that can be used to reduce them.

6.1 The detector

The CUORE (Cryogenic Underground Observatory for Rare Events) experiment [40] is the natural prosecution of Cuoricino. It aims at searching for 0νDBD of ^{130}Te with a background $< 10^{-2}$ counts/keV/kg/yr and an effective Majorana mass sensitivity of a few tens of meV, reaching the so called inverse hierarchy region of the neutrino mass spectrum. It is presently under construction in the Hall A of the Gran Sasso Underground Laboratory (LNGS).

The CUORE detector is a system of 988 cryogenic bolometers. The array is composed by 19 vertical towers cooled by means of a dilution (^{3}He/^{4}He) refrigerator to a temperature of $\sim$10 mK. A tower consists of 13 floors of 4 bolometers each. The bolometers are quite similar to the Cuoricino ones, with a $5\times5\times5$ cm^3 TeO_2 cubic crystal, an NTD Ge thermistor, and a heater (a Si resistor doped with As). Each cube has a weight of 750 g, so the detector is a granular calorimeter of total mass 741 kg, corresponding to $\sim$200 kg of ^{130}Te .

In Figure 6.1 the single module (i.e. one floor of the tower), the single tower and the entire CUORE detector are reported.

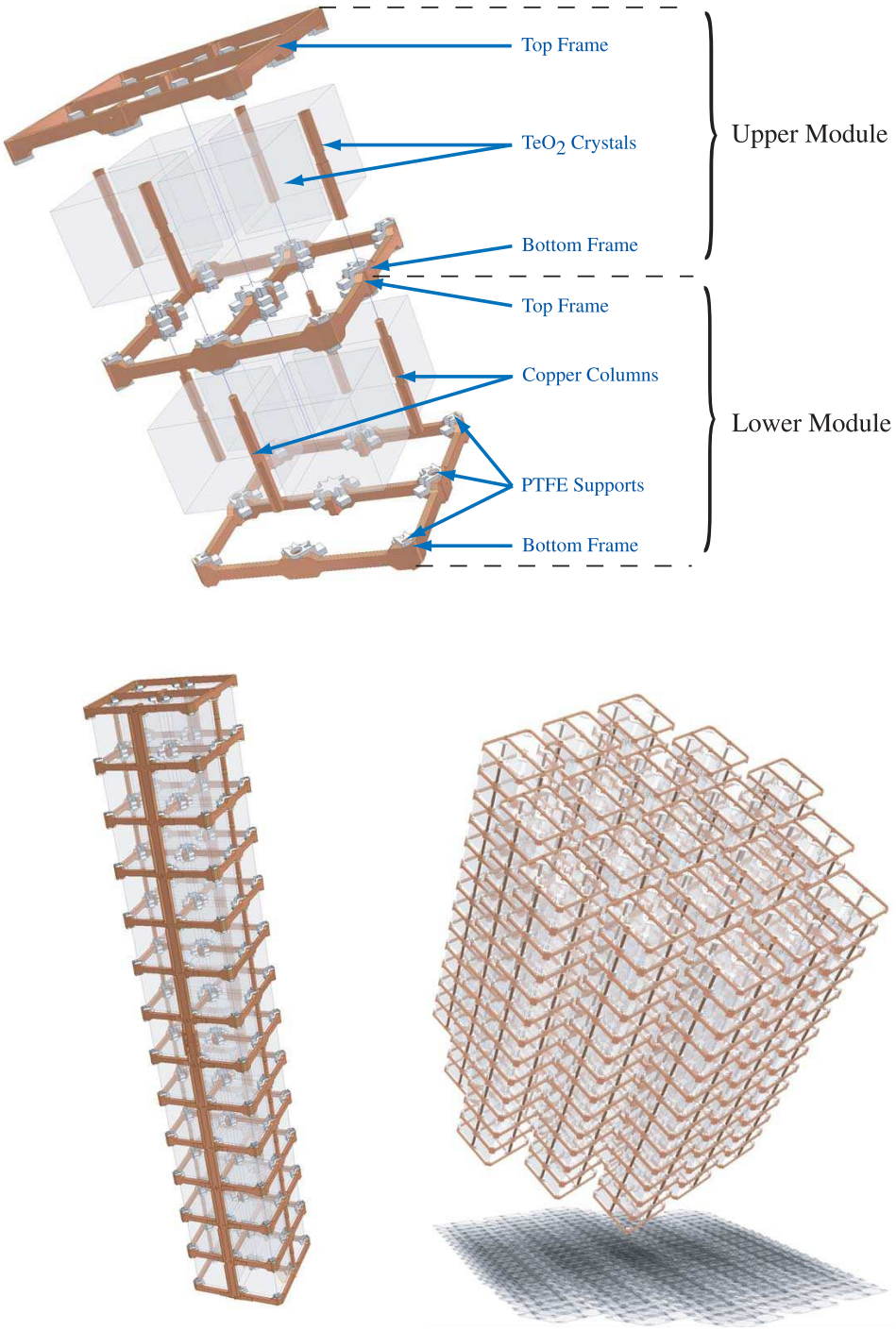

Figure 6.1: The CUORE modular structure. On top: two contiguous floors. Each frame is shared between two consecutive single modules. The copper columns join the two frames to fasten rigidly the crystals. Left on the bottom: A CUORE tower. 13 single modules are held together. Right on the bottom: the entire CUORE detector (cylindrical-shaped) built of 19 super modules.

The experiment will take great advantage from the tightly packed structure thanks to the high background rejection capability that can be obtained by operating the detectors in anti-coincidence mode. Since there is a small probability for the two electrons of 0νDBD to escape from the crystal where they are emitted, a simultaneous hit in more than one detector is an indication of a background event. In contrast to Cuoricino, most of the crystals will be completely surrounded by other detectors, thus allowing an important reduction of the background sources, especially of crystal surface contaminations.

The CUORE background goal of $<10^{-2}$ counts/keV/kg/year requires a great attention to the internal and surface contaminations levels of the crystals. For this reason the production, shipment and storage of the crystals was performed in demanding conditions.

In 2009 the production of CUORE crystal started at SICCAS Jiading with a production capacity of about 30 crystals/month [52]. The production of crystals is systematically controlled and each production phase is certified [82]. Very strict certification conditions were applied for the dimensions of the crystals and for the quality of surface processing. In the case of radio-purity the certification is based on the results obtained by ICP-MS measurements of raw materials and intermediary products. Moreover, a dedicated cryogenic setup mounted and operated in Hall C of LNGS is used to test TeO_2 crystals. The tests are performed on crystals randomly chosen from each production batch and is aimed at checking the radioactive contamination level of crystals and their bolometric performance, measured in conditions similar to those planned to be used for CUORE.

Limits on crystals bulk contaminations obtained with these bolometric tests are $\sim 10^{-14}$ g/g for ^{238}U and $\sim 5 \cdot 10^{-14}$ g/g for ^{232}Th at 90% C.L. [83]. These values are well below the concentration limits requested for TeO_2 crystals to be used in CUORE experiment.

In the CUORE Crystals Validation Runs (CCVR), crystals showed excellent bolometric characteristics, including a very good energy resolution (FWHM better than 5 keV in the spectral region of interest for CUORE). As I will show in Section 6.4, these values allow to aim at a CUORE sensitivity able to probe the inverse hierarchy of the neutrino masses.

6.2 Cryostat and shieldings

The CUORE cryogenic apparatus is shown in Fig. 6.2. The cryostat is made of six nested vessels and its base temperature without heat loads is expected to be as low as 6 mK. Three lead shields are used to protect the detector from environmental radioactivity and from contaminations in the building materials. A 25 cm thick octagonal lead layer outside the OVC shields the detector from radiations coming from the bottom and from the sides. An equivalent shielding against radiation coming from the top is placed inside the cryostat, just above the detector. This is a 30 cm thick lead disk with a diameter of about 90 cm. Just below it, copper disks totaling an additional 8 cm shields are placed. An additional shielding of detector's sides and bottom is provided by a 6 cm lead layer just outside the

Steel shield.

Outside the external lead shield an 18 cm thick polyethylene layer will be added in order to thermalize environmental neutrons that will then be absorbed by a 2 cm layer of H_3BO_3 powder contained in the hollow space between the lead and the polyethylene itself. On the top and on the bottom of the setup, due to construction difficulties, the neutron shield will be made of a single 20 cm layer made of polyethylene with 5% in boron.

The adopted layout for the geometry of the shields here described is the one I have studied and optimized during my PhD thesis with the aid of the Monte Carlo simulations that are described in the next paragraph. A second output of these studies have been the prove that the muon veto, discussed as a possible (expensive) tool necessary to ensure the required background figure, is not required.

6.3 Geant4 simulation

In this chapter I will describe simulations I have carried out to study the contribution to CUORE background due to environmental contributions, namely gamma rays (mainly from radioactivity), neutrons (induced by radioactivity or cosmic rays) and muons (the only residual of cosmic rays surviving at the LNGS depth). Informations about the background due to detector contaminations can be found in [53].

I skip here the initial step of the simulation work, when I considered the different possible configurations for the external shields and describe the final adopted configuration that is a compromise among different factors: shields efficiency (that I've studied with the simulation), cost and mechanical constraints. For this final configuration I will discuss the different background contribution expected from environmental sources.

The CUORE geometry used in the simulation is shown in Fig. 6.3 [53]. The setup of the external shield has been slightly simplified with respect to the real CUORE design. The 988 detectors are arranged as in the real CUORE design. The copper frame structure used to assemble the detector towers and the wire and source trays are also implemented. The small detector details (pins, thermistors, gold wires, Teflon spacers, glue spots, etc.) are not implemented, due to their negligible influence on the results concerning environmental contribution to the experimental background (a few tens of grams total mass against the hundreds tons mass of the shielding).

The output of the Monte Carlo simulation is converted in detector output by means of an additional code, G2TAS [53]. In order to take into account the features of the detector response, namely the slow pulse development and the dead time, two events depositing energy in the same detector are considered as a single event if the time interval between them is less than an integration time of 10 ms. A decay rate can be specified for each source, so that all pile-up events (two events in the same bolometer within the acquisition window of 4 s) are rejected. Coincidence patterns between the detectors (based on event

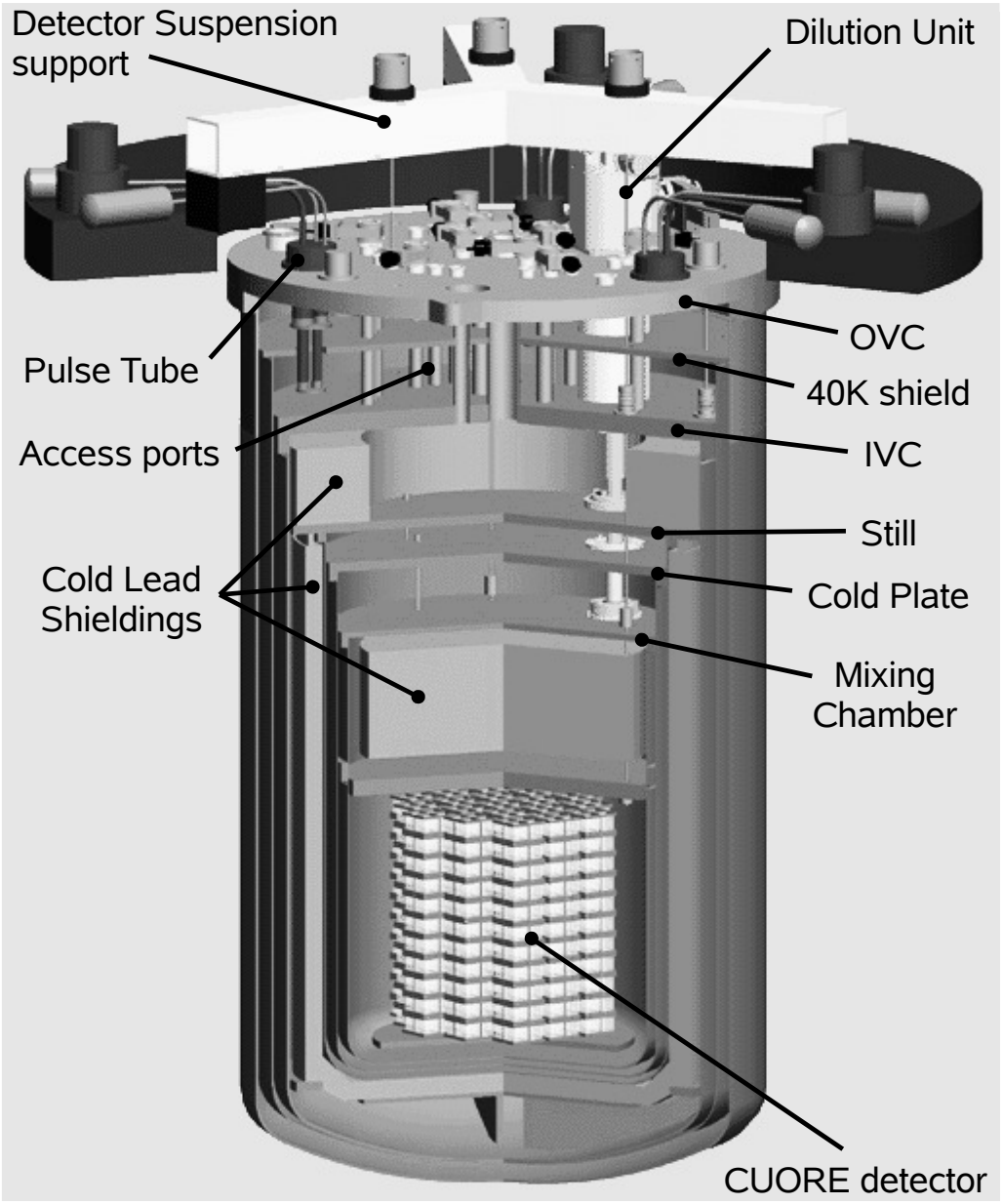

Figure 6.2: 3D view of the cryogenic apparatus.

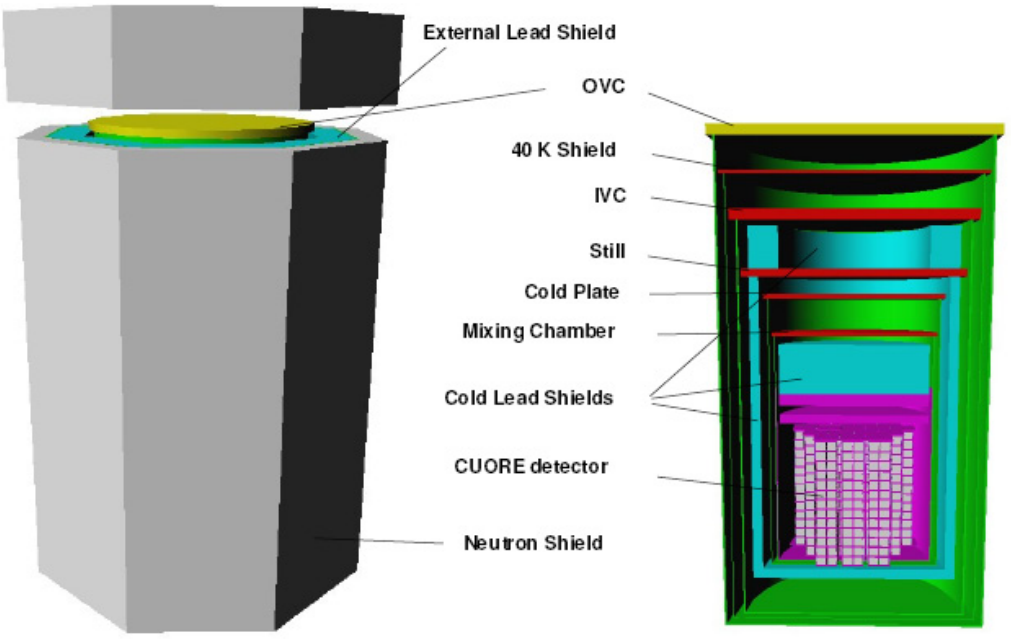

Figure 6.3: 3D view of the geometry implemented in the simulation: external octagonal PET shield (left) and internal shields and detector (right).

multiplicity, evaluated both in the entire detector array and for the nearest neighbors) are invoked when computing spectra and scatter plots, as it is for experimental data. An energy threshold of 50 keV is assumed. The detector resolution is taken into account introducing a gaussian smearing with 5 keV FWHM. The ROI has been chosen as a symmetric region 40 keV wide around the nominal Q-value of the 0νDBD of ^{130}Te. In this region no gamma photoelectric peaks due to environmental radioactivity are expected (it has been chosen above the ^{60}Co sum gamma line at 2505 keV and below the 2615 ^{208}Tl line).

6.3.1 Simulation results

The contribution of the environmental gammas impinging on the external shields of CUORE to the background in the ROI has been evaluated by simulating primary gamma events at 2615 keV, the dominant gamma contribution to the background in the 0νDBD region of ^{130}Te (see Section 3.4.2). According to the spectrum measured in the Hall A of LNGS the flux at this energy is $9{\cdot}10^{-3}$ γ/s/cm^2. The primary gamma events have been uniformly generated on a spherical surface of 500 cm radius, surrounding the most external shield. The background value in the ROI is obtained by multiplying the integral of the Monte Carlo spectrum in that region by the normalization factor between the number of

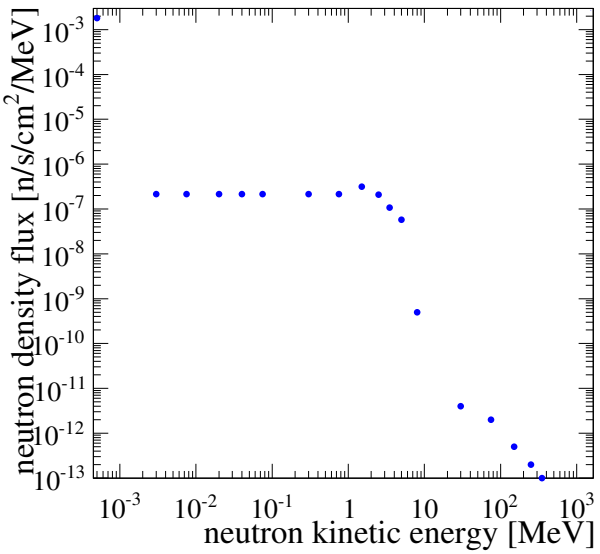

Figure 6.4: Simulated neutron flux density as a function of the neutron kinetic energy. Values are taken accordingly to experimental data [55, 56] (below 10 MeV) and to existent simulations of muon induced neutrons at LNGS [57] (above 10 MeV).

generated events and the actual flux of 2615 keV gammas at LNGS.

The results are reported in the first row of Tab. 6.1 where the total, the global anti-coincidence and the near channel anti-coincidence contributions are shown. No anti-coincidence cut is applied in the first case, while an anti-coincidence cut between all the 988 detectors and between each detector and its 18 closest ones are applied in the second and in the third case, respectively (operating the detector in anticoincidence could imply a quite high dead time, that is the reason to consider a coincidence cut involving only nearest neighbors and to evaluate its efficiency). The probability for a gamma ray generated from outside the external shield to reach the detector is very low and, due to Compton interactions, the energy released is low and below the 0νDBD Q-value. Only multi-Compton events can produce background in the 0νDBD region. No event has been recorded in the Monte Carlo in the ROI, so only an upper limit has been obtained by considering Poisson statistics, well below the CUORE background goal of $<10^{-2}$ counts/keV/kg/year.

The environmental neutron spectrum has been simulated according to the neutron flux at LNGS. The simulated spectrum is reported in Fig. 6.4. The energy interval between 25 meV (thermal neutrons) and 1.5 GeV has been divided in 22 logarithmic energy bins. Flux values are taken according to existing experimental data [55, 56] below 10 MeV and to simulations of muon induced neutrons at LNGS [57, 59] above 10 MeV. In order to be conservative, for each energy bin the highest flux among different measurements or

Source	Statistics [years]	Total	Anti-coinc. (Global)	Anti-coinc. (Near chan.)
Gamma	0.1	0.390	0.390	0.390
Neutron	7.88	0.270 ± 0.022	$(8.56 \pm 6.06) \times 10^{-3}$	0.0642 ± 0.0442
Muon	4.05	17.3 ± 0.3	0.104 ± 0.022	1.850 ± 0.049

Table 6.1: Background in the ROI obtained by simulations of the evaluated gamma, neutron and muon fluxes at LNGS. Quoted errors are statistical only. Units are: 10^{-3} $counts/kg/keV/yr$. Limits are given at 90% C.L.

different simulations has been used. The total neutron flux, thus extracted, is found to be: $(3.7 \pm 0.2) \cdot 10^{-6}$ n/s/cm^2 . The results are summarized in the second row of Tab. 6.1. Even without exploiting anticoincidences the background is well below the CUORE requirement. Furthermore, a reduction factor greater than 1 order of magnitude could be obtained by applying a global anti-coincidence cut and a reduction factor of $\sim$5 by applying a near channel anti-coincidence cut. In Fig. 6.5 a comparison between the neutron background spectrum before and after the global and near channel anti-coincidence cuts is shown. Simulations performed splitting the neutron spectrum in the energy bins of Tab. 3.3 show that the largest contribution is due to neutrons with energies up to 10 MeV, i.e. radioactivity induced neutrons.

Finally, muon induced background was modeled by generating muons on a spherical surface of 500 cm radius (similar to gamma rays and neutrons) and transporting these muons along with all secondary particles produced in muon interaction in the detector materials, through the whole setup. All energy depositions in the crystals were recorded. The muon spectrum angular distribution is parameterized on the MACRO data and it is described in details in Section 5.5

The muon energy has been chosen between 1 GeV and 10 TeV underground, including 99.2% of the total muon flux. The resulting total background from cosmic ray muons (third row of Tab. 6.1) is higher than the CUORE goal. A reduction factor of almost two orders of magnitude is obtained by applying a global anti-coincidence cut and a reduction factor of $\sim$10 by applying the near channel anti-coincidence (Fig. 6.5). In this way I proved that the CUORE background requirement could thus be reached without the necessity of a muon veto system.

As a final remark it is worth to mention that the errors quoted in Tab. 6.1 and for the background results are statistical only. The neutron flux above 10 MeV, due to cosmic muon interactions in the rock surrounding the laboratory, has a systematic error of about a factor 2. This value takes into account both the discrepancies between the Monte Carlo calculations performed with different codes (i.e. GEANT4 and FLUKA) [84] and between

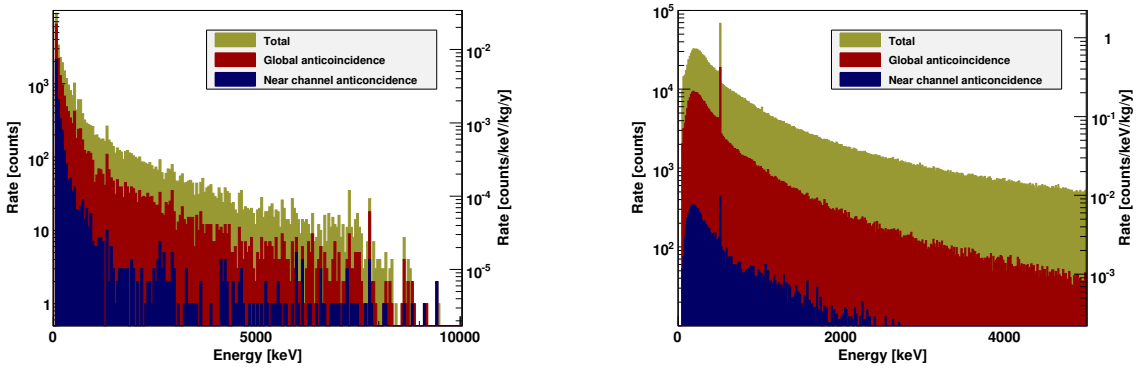

Figure 6.5: Comparison of the Monte Carlo spectra obtained by simulating neutron flux (left) and muon flux (right) at LNGS. In each plot the spectrum obtained without any anti-coincidence cut (green) is shown together with the ones obtained by applying the global anti-coincidence (blue) and the near channel anti-coincidence (red) cut respectively. On the right side of each plot the axis reporting the expected counts/keV/kg/yr in the CUORE detector is shown.

the calculations and the available neutron yield data for light targets and for heavy targets like lead [85]. Below 10 MeV the systematic uncertainty on the measured neutron flux is evaluated to be 6.5% for [56] and 31.6% for [55] and the two measures have discrepancies up to a factor 3. Also with the conservative approach adopted (see above) the event rate is much below the CUORE target. An additional source of systematics in the background evaluation is due to neutron propagation and detection in the simulation code, mainly related to the precision of the cross section tables used to model capture, elastic and inelastic scattering. According to [54] it has been assumed to be 20%.

The systematic error in the muon flux is 8% [62]. Uncertainties in the muon induced neutron yield, neutron transport and detection must be also taken into account as a source of systematic error together with the uncertainties in the models used in GEANT4 to evaluate the electromagnetic component. The former has a total error of 45%, the latter of 5% [54].

The uncertainties in the environmental gamma flux at LNGS originate from the measurement statistics and from the detector efficiency evaluation, performed with Monte Carlo simulations. The gamma peaks are measured with uncertainties of less then 8%, while the simulation uncertainties in the GEANT4 electromagnetic tracking have been evaluated to be at a few percent level [54]. Gamma transport, interaction and detection uncertainties in the Monte Carlo code used to extrapolate the CUORE background are an additional source of systematics at a few percent level.

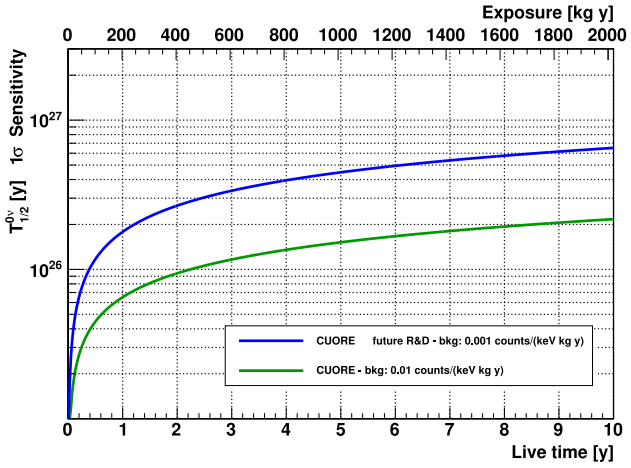

Figure 6.6: Sensitivity limit of the CUORE experiment at 1σ (green line). The sensitivity for a potential future CUORE-like experiment with an improved background of 0.001 counts/keV/kg/y is also shown (blue line).

6.4 CUORE sensitivity

As described in Chapter 3, the sensitivity of an experiment depend on energy resolution, background, live time and detector mass.

The expected energy resolution FWHM of the CUORE detectors is ≈ 5 keV at the 0νDBD transition energy. This resolution has already been achieved in tests performed in the CUORE R&D facility at LNGS. The duty cycle in CUORE is expected to be higher than that of Cuoricino, mainly due to improvements in the cryogenic, calibration and electronics systems. CUORE is expected to accumulate data for about 5 years of total live time. The background rate is the most critical parameter to assess before the calculation of the sensitivity can be carried out.

The new crystal production protocol developed for CUORE has improved the overall radiopurity of the crystals as compared to those used in Cuoricino, even before surface cleaning. A new copper cleaning procedure has also been developed for CUORE, which will be applied to the copper shields and frames. The design of the frames which hold the crystals has been refined, such that the surface area of the CUORE-style frames which faces the crystals is about 2 times less than for the Cuoricino-style frames. CUORE, in addition to the new crystals and frames, will be assembled as a 19-tower array in a newly-constructed cryostat. The change in detector geometry will have two effects. First, significantly improve anti-coincidence background rejection efficiency, allowed by the large closely-packed array, will further improve the reduction in crystal-related backgrounds. Second, the outward-facing surface area of the crystals (i.e. the surfaces covered by copper shields) will constitute a much smaller percentage of the total surface area of the

crystals, leading to a reduction factor ∼3 respect to Cuoricino. In addition to these considerations, the new cryostat will contain thicker lead shielding and be constructed of cleaner material, resulting in a predicted gamma background approximately an order of magnitude better than that in the Cuoricino cryostat. Based on the above considerations and the Cuoricino results, we can expect CUORE to achieve its design background value of 0.01 counts/keV/kg/y.

A plot of the sensitivity for the CUORE experiment, for a FWHM of 5 keV and a background of 0.01 counts/keV/kg/y, as a function of the live time and exposure is shown in Figure 6.6. The values for the sensitivity are reported in 6.2. While it is fairly certain that CUORE will reach a background level of 0.01 counts/keV/kg/y, much lower values are a challenge still open. Sensitivities for a future scenario with 0.001 counts/keV/kg/y in a CUORE-like experiment are given in Fig. 6.6 and Tab. 6.2.

Background	ΔE	Half-life sensitivity		
count/keV/kg/y	keV	10^{26} y		
		2 y	5 y	10 y
0.01	5	0.94	1.52	2.17
0.001	5	2.67	4.47	6.51

Table 6.2: Sensitivities at 1σ for CUORE to the half-life after two, five and ten years of live time. The sensitivities for a CUORE-like experiment with improved background are also reported.

In Fig. 6.7, the expected sensitivity of CUORE is compared with the preferred values of the neutrino mass parameters obtained from neutrino oscillation experiments. The sensitivity of CUORE will allow the investigation of the upper region of the effective Majorana neutrino mass phase space corresponding to the inverted hierarchy of neutrino masses.

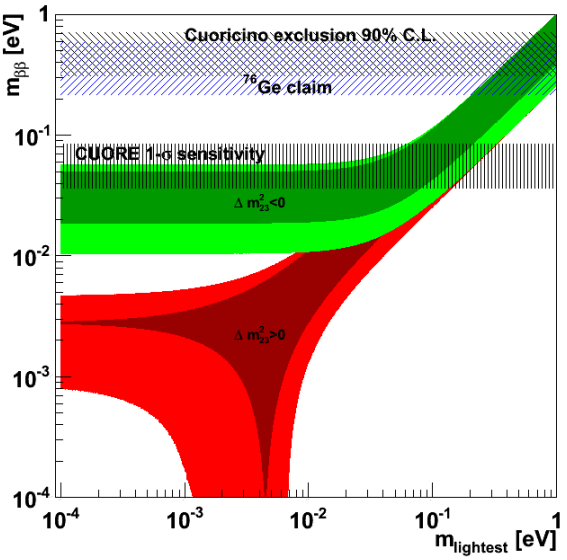

Figure 6.7: Cuoricino result and CUORE sensitivity. The ranges of the Cuoricino and CUORE bands are given by the maximum and minimum values of $m_{\beta\beta}$ obtained from the latest NME [26, 27, 28, 29].

Chapter 7

Research and Development

Cuoricino showed that in 0νDBD study with the bolometric technique, background due to surface contamination plays a key role. To better understand the behavior of this source of background and study efficient techniques for its reduction, many tests were performed in the dilution cryostat installed in the hall C of LNGS. With this cryostat it was possible to study both passive methods (i.e. copper cleaning and polyethylene films) and active methods (i.e. scintillating bolometers) for the reduction of the background. Since the latter is a significant part of this work it will be described in detail in next chapters. The passive methods are instead summarized in this chapter. In this chapter I will also describe a measurement made in the Hall A of LNGS with the aim of study surface contamination with high statistical significance: the Three Tower Test (TTT).

7.1 Experimental setup and physical goals

The Hall C cryogenic apparatus is an Oxford Instruments dilution refrigerator with a cooling power of 200μW at 100 mK (for details see Appendix). The external shield consists of 10 cm of lead surrounded by a neutron shield of $\sim$7 cm of polyethylene and about 2 cm of CB_4. To shield the bolometers from γ radiation due to cryostat contaminations a $\sim$5.5 cm Roman lead shielding is placed inside the cryostat just above detectors, $\sim$1.2 cm on the sides and $\sim$3 cm just below.

Inside the cryostat a special suspension system mechanically decouples the structure from cryogenic detectors in order to eliminate vibrations that can be harmful to the bolometers. The suspension system consists of two different stages (Figure 7.1): the first consists of a 14 kg disk of Roman lead, the second is composed of the detectors.

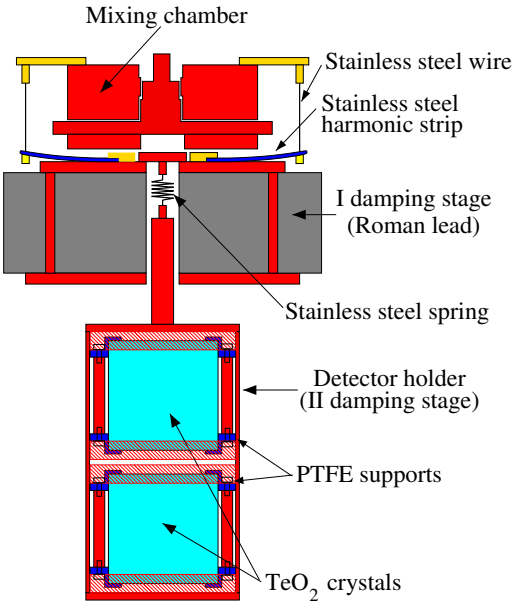

Figure 7.1: The two-stage damping system with a 2 bolometers setup.

The thermal link between the cryostat and the detector frames is achieved by a two thin strips of copper thickness of 50 μm which connect the mixing chamber to the copper structure of the detectors.

The main purpose of the measurements done in this cryostat is to understand the background observed by Cuoricino in the 0νDBD region. As already mentioned, this background has a clearly identified contribution from multicompton events due to ^{208}Tl. The residual $\sim$70% looks to be due to a source different from environmental gamma rays and have been the subject of the studies described in this chapter. The main signature of this latter source is the flat continuum extending from 4 MeV down to the 0νDBD region. Although we are interested in the reduction of the counting rate in the 0νDBD region, in order to have enough statistics in a reasonable time (some months), the larger energy region between 3 and 4 MeV is usually considered. In this region there are no peaks due to environmental γ radioactivity that ends, in practice, at 2615 keV and there are also no α peaks due to radioactive chains falling at higher energies. This region is then usually used to study the flat background that extends to even lower energies.

In Hall C apparatus had been performed, from 2004 to 2006, a set of measurements called RAD (Radioactivity Array Detector) with an array of eight 5×5×5 TeO_2 crystals. Each measurement was planned in order to study possible contribution to the 3-4 MeV background. The six RAD measurement concerned respectively:

- **RAD1**: a procedure to clean the surfaces of TeO_2 crystals (nitric acid + polished with SiO_2 powder) and copper (electro-polishing) (Fig. 7.2(a))

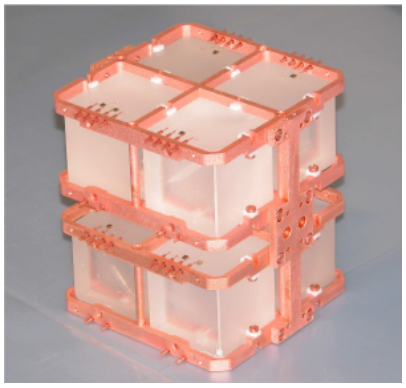

(a) RAD1

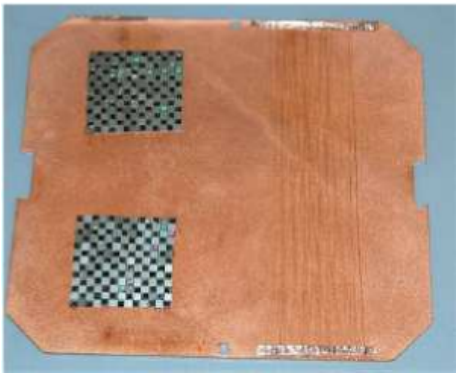

(b) RAD2

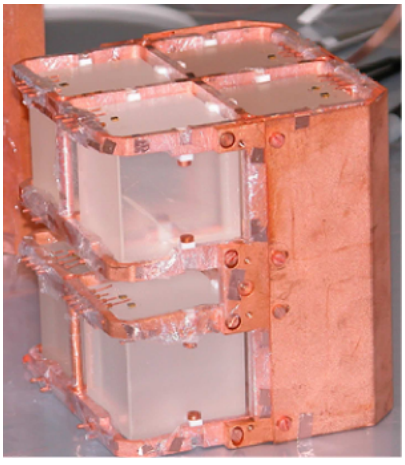

(c) RAD3

Figure 7.2: In figure (a) the RAD1 assembly. In figure (b) the small components (Si heaters and Au wires) faced to the detectors. In figure (c) the RAD3 assembly in which it is possible to observe the polyethylene wrapped around frames.

- **RAD2**: the possible contributions to the background due to the small components of the detector (Si heaters and Au wires) (Fig. 7.2(b))
- **RAD3**: the possible contributions to the background due to the copper. The copper was wrapped with a thin ($\sim$60 μm) polyethylene film (Fig. 7.2(c))
- **RAD4**: other external contributions to the background, especially neutrons
- **RAD5** and **RAD6**: other non radioactive source of background (i.e. teflon relaxations)

These measurements allowed a better understanding of the background and of the efficiency of the cleaning procedures. The procedure that was developed for the RAD1 provided a background reduction by a factor ≈ 4 of the α peaks ascribed to surface contaminations of the crystals, although no appreciable effects were seen on the flat background between 3-4 MeV.

An improvement in this direction was obtained in RAD3: the copper elements of the mounting structure were covered by a 60 μm thick polyethylene layer, whose goal was the screening of the α particles coming from the copper surfaces. This procedure provided a reduction of the counting rate in the 3-4 MeV region of a factor $\approx 2 \pm 0.4$ respect to Cuoricino and RAD1.

RAD2 and RAD4 demonstrated the possibility of neglecting contributions due to the small components and neutrons; the other tests (RAD5 and RAD6) did not rule out possible contributions to the background (for example, due to teflon relaxation processes) because of an excessive surface contaminations of materials used to replace teflon.

The results of the RAD tests (together with Cuoricino ones) can be extrapolated by means of Monte Carlo simulations in order to obtain a projection for the background of CUORE. The obtained model attribute the most dangerous sources of background in the 3-4 MeV region to contaminations of the Cu surfaces. Thus, a development of a cleaning procedure for these elements is necessary.

7.2 The Three Towers Test

Measurements done in Hall C allowed to understand Cuoricino background ascribing it mainly to surface contaminations of copper and crystals and allowing to discard other hypothesis like neutrons and muons contributions or possible contributions from bulk contaminations of the "small parts". Also these measurement gave indication on the procedure to be used for a reduction of the 3-4 MeV background (the same source that accounts for 70% of the Cuoricino 0νDBD counting rate). However RAD measurements were not completely satisfactory because affected by a high statistical errors (that could be reduced only with extremely long runs). For this reason they can not be used, for

example, to compare achievements obtained with different surface treatments. The only way to solve this problem is to increase the number of detectors. For this reason, at the end of Cuoricino, the bigger cryostat of Hall A was used to make a test (the Three Tower Test) to compare different surface treatment protocols for copper elements. Moreover this test allowed a more direct comparison with Cuoricino results since the same setup was used.

The three different cleaning procedures compared in the Three Tower Test (TTT) were:

1. **Legnaro protocol (T1)**: this cleaning procedure is performed at the Legnaro National laboratories of INFN. It has the advantage of being completely industrialized. It consists in four steps: Tumbling, Electro-polishing, Chemical Etching and Magnetron Plasma Cleaning (TECM).

2. **LNGS protocol (T2)**: it consists in a combination of electro polishing, chemical etching and passivation with citric acid.

3. **Polyethylene protocol (T3)**: the copper elements are passivated in citric acid and wrapped with several polyethylene layers.

Three towers composed by 12 bolometers each were realized (see Figure 7.3), and each tower was cleaned with one of the three procedures. The detectors operated from September 2009 to January 2010.

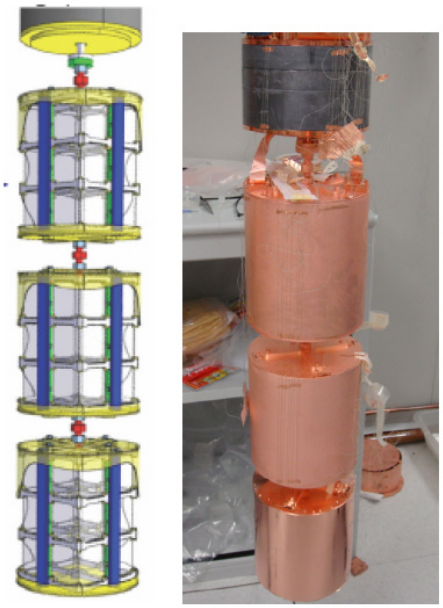

(a) *Schematic drawing.* (b) *Closed detector.*

Figure 7.3: Three Towers Test: detector.

Measurement	Background 3-4 MeV [counts/keV/kg/y]
Legnaro protocol	0.058±0.005
LNGS protocol	0.068±0.007
Polyethylene protocol	0.055±0.006
Cuoricino	0.125±0.001
Polyethylene protocol (Anti-coinc)	0.041±0.006
Cuoricino (Anti-coinc)	0.107±0.001

Table 7.1: Tree Tower Test and Cuoricino results. In the upper part the results obtained without any anti-coincidence cut are reported. In the lower part are reported the results with anti-coincidence cuts for the T3 tower and Cuoricino.

Unfortunately, a large number of electric connections of the T1 and T2 towers broke during the cooling down. This reduced the statistics collected with these towers and for this reason the anti-coincidence analysis could be performed only on the Polyethylene tower (T3).

Results obtained with the tree tower and their comparison with Cuoricino are reported in table 7.1. They show how the new copper cleaning techniques have led to a substantial reduction of the background in the 3-4 MeV region compared to Cuoricino. However, because the statistics are not very high, backgrounds of the three towers are compatible within 2σ. A more detailed analysis of the coincidence spectra showed that crystal surface contribution to the background is not important (negligible contribution in the anti-coincidence background).

These improvements in the reduction of the background due to copper contamination, together with the significant reduction of the surfaces facing copper in CUORE, allow to expect to achieve the CUORE design background value.

However, as we shall see in later chapters, the possibility of using active methods (i.e. scintillating bolometers) for the discrimination of interacting particles can significantly reduce the background due to degraded alpha particles. In addition, we will see how scintillating bolometers can be used as a powerful tool for the study of surface contamination of copper.

Part III

Scintillating Bolometers

Chapter 8

Scintillating Bolometer

Cuoricino and R&D tests had shown that most probably the main source of background for the bolometric technique in the 0νDBD region (2.6-4 MeV) arise from surface α contaminations. A possible solution to this problem is the identification of the interacting particle through the use of scintillating bolometers. The simultaneous and independent read out of the heat and the scintillation light permits to discriminate events due to γ/β, α and neutrons thanks to their different scintillation yield. This allows a significant reduction of the unwanted background in the region of interest for 0νDBD and would therefore allow to approach the condition of 'zero background' experiments. During the work done for my thesis on scintillating bolometers for 0νDBD I have realized that these devices can be suitable also to measure surface alpha contaminations with sensitivities much higher than those achievable with most (if not any) traditional techniques. In particular these detectors would allow to prove without any doubt that the background measured by TeO_2 bolometers in the 0νDBD region is dominated by alpha particle, as many indications suggest.

In this chapter, after the description of the working principles and the experimental setup, I will describe results obtained with some of the tested scintillating crystals.

8.1 Working principles

The working principle of scintillating bolometers can be summarized as follow. The detector is obtained by coupling a scintillating crystal - operated as bolometer - to a light detector (Figure 8.1). When a particle interacts with the scintillating crystal a large fraction of the deposited energy is converted into heat, while a small fraction of it is spent to produce scintillation light (i.e. photons irradiated outside the crystal). For each interaction, two signals are recorded: a thermal signal produced in the scintillating bolometer

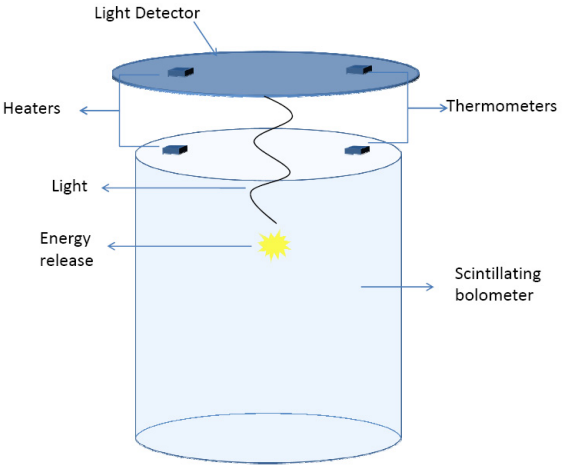

Figure 8.1: Illustration of the operating principle of scintillating bolometers. The release of energy inside a scintillating crystal follows two channels: light production and thermal excitation.

and a photon signal read-out by the light detector. The ratio between the two (heat vs. light) depends on the particle Light Yield (LY). Betas and gammas have the same LY, which is typically different from the LY of alphas or from that of neutrons. Consequently, the contemporary read out of the heat and light signals allows particle discrimination.

The usual way to present the results is to draw the light vs. heat scatter plot (left in Figure 8.2). Here each event is identified by a point with abscissa equal to the heat signal (recorded by the main bolometer), and ordinate equal to the light signal (contemporary recorded by the LD).

Two important parameters that characterize scintillating crystals are the Light Yield (LY) and the scintillation Quenching Factor (QF). In the following I will refer to LY as the energy released in the Light Detector (LD) for a nominal energy deposition of 1 MeV in the scintillating crystal. This parameter cannot be used for an absolute evaluation of the amount of scintillation light emitted by the crystal since the light amplitude is not corrected for the photon collection efficiency that is certainly below 1. The scintillation Quenching Factor is the ratio of the scintillating yield of an interacting particle (α, neutron, nucleus) with respect to the LY of a γ/β event at the same energy.

Before describing setup and results is useful define also the "discrimination confidence level" that will be used in the following sections. The discrimination between the α and the β/γ populations, provided by the scintillation signal, can be evaluated by measuring the difference between the average amplitude of the light signal produced by the two kind of particles ($\text{Light}_{\beta/\gamma}$ and Light_{α}), considering a group of events releasing the same energy in the scintillating crystal. This difference is then compared with the width of the two

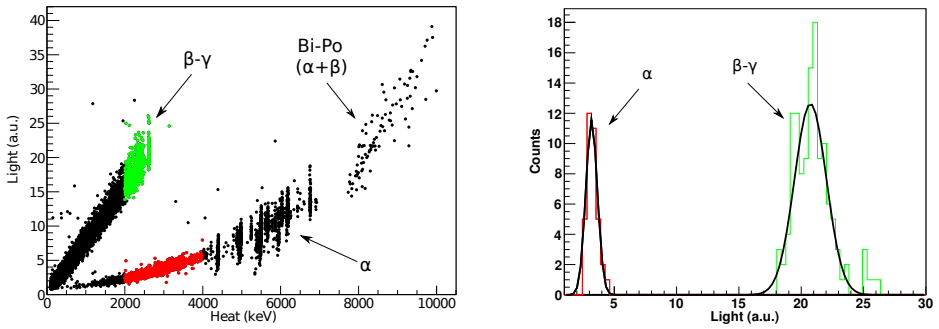

Figure 8.2: On the left: scatter plot of light vs. heat in a $CaMoO_4$ crystal. In red events in the 2-4 MeV region due to α particles while in green events due to β/γ in the same region. On the right: evaluation of the β/γ and α discrimination power in $CaMoO_4$ by projection on the light axis of the ^{208}Tl γ-line (2615 keV) (in green) and of α events (in red) that released a similar energy in the $CaMoO_4$ crystal. The separation corresponds to 12.6 sigma.

distributions ($\sigma_{\beta/\gamma}$ and σ_α). The discrimination confidence level D_{Light} is then defined as:

$$D_{Light} = \frac{Light_{\beta/\gamma} - Light_\alpha}{\sqrt{\sigma^2_{\beta/\gamma} + \sigma^2_\alpha}} \tag{8.1}$$

For example to evaluate this discrimination power at 2615 keV I have selected events belonging to the γ-line of ^{208}Tl and I have compared their light pulse distribution with events of similar energy in the α band (right in Figure 8.2). The reason for using events with the same energy to evaluate D_{light} is the energy dependence of the distance (and width) of the α and β/γ bands, that induce an energy dependence of the discrimination confidence level.

8.2 Experimental Setup

All the measurements described in this chapter were performed in configurations very similar to each other using the CUORE R&D cryostat installed in Hall C of LNGS. For details on cryostat and shieldings see Chapter 7. If a measurement was made with a different configuration from the one described below, will be explicitly stated.

The temperature sensor used for almost all scintillating crystals are 3x3x1 mm^3 neutron transmutation doped Germanium (NTD thermistors), the same used in the Cuoricino experiment. The temperature sensors of the bolometric LD (see Chapter 8.2.1) are NTD thermistors with smaller volume (3x1.5x0.4 mm^3) in order to decrease their heat capacity, increasing therefore their thermal signal. A resistor of $\sim$300 kΩ is attached to each absorber

and acts as a heater (i.e. it is used to produce a reference signal as described in section 4.7).

The heat and light pulses, produced by a particle interacting in the scintillating crystal and transduced in a voltage pulse by the NTD thermistors, are amplified and fed into a 16 bit NI 6225 USB ADC unit. The entire waveform of each triggered voltage pulse is sampled and acquired. At the ADC input, a low pass Bessel filter is used as anti aliasing to avoid spurious contributions in the sampled signal [40]. The time window has a width from 256 ms to 4096 ms and could be sampled with 512-8192 points according to the studies done. The trigger of the scintillating crystals is software generated while the LD is usually automatically acquired in coincidence with the former. The amplitude and the shape of the voltage pulse is then determined by the off line analysis that makes use of the Optimal Filter technique.

We have tried to standardize as much as possible the crystals assemblies: each scintillating crystal was faced to only one Light Detector and it was surrounded (without being in thermal contact) by a reflecting sheet (3M VM2002) to better collect the scintillation light. However, sometimes because of the different shape of the scintillating crystals or because of the goal of the measurement, the assembly was different by the one described above.

Since the main goal of scintillating bolometer measurements was evaluate the capability to recognize and reject α particles, radioactive sources were usually faced to the scintillating crystal. Mainly two different kind of radioactive source were used: source A and source B.

Source A was obtained by implantation of ^{224}Ra (through the nuclear recoil of ^{228}Th) in an Al reflecting stripe. The shallow implantation depth allows to reduce to a minimum the energy released by the α's in the Al substrate so that monochromatic α lines (those produced in the decay chain of ^{224}Ra to the stable ^{208}Pb isotope) can be observed in the scintillating bolometer. In Figure 8.3 the source A spectrum measured by a Si surface barrier detector is reported. Besides α particles, all with energies above 5 MeV, source A emits a β with a maximum energy of 5 MeV, due to the decay of ^{208}Tl.

Since our main goal was to study the efficiency of α particle rejection in the 0νDBD region (i.e. at about 3 MeV), a second source (B) was used. This was obtained contaminating an Al stripe with a ^{238}U liquid solution and later covering the stripe with an alluminated Mylar film. Thus the source has a continuous spectrum of α particles, extending from about 3 MeV to 0. In Figure 8.4 the spectra, measured by a Si surface barrier detector, for different thicknesses of the alluminated Mylar film is reported. For the source B we have chosen the 6 μm thick.

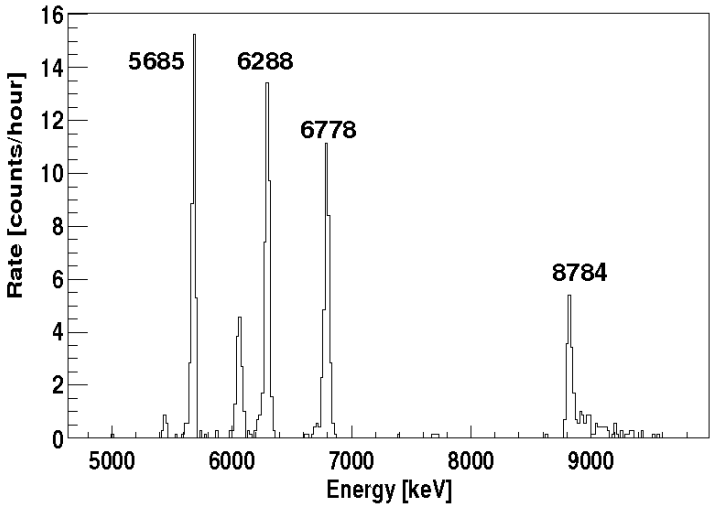

Figure 8.3: Spectrum of source A as recorded by a Si surface barrier detector (having 35 keV FWHM energy resolution at 5 MeV). The energy [keV] of the main lines is indicated.

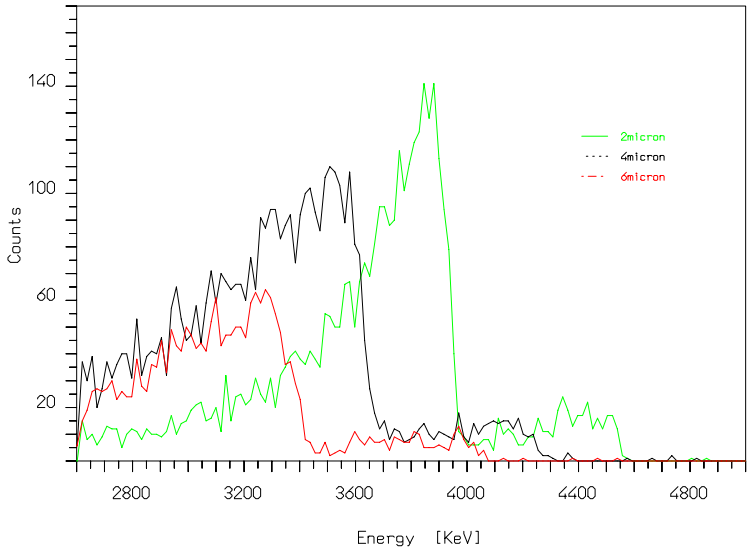

Figure 8.4: Spectra recorded by a Si surface barrier detector for different thicknesses of the alluminated Mylar film used to cover the stripe with ^{238}U liquid solution.

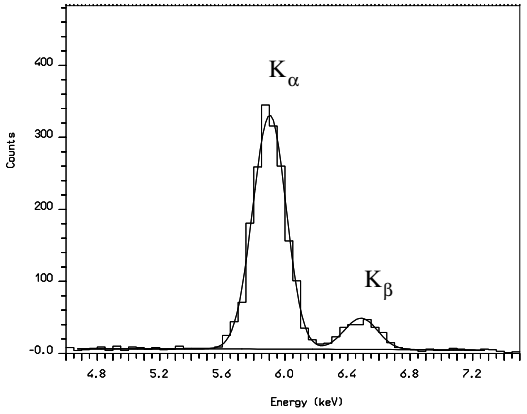

Figure 8.5: Calibration spectrum (fitted with two Gaussian distribution functions) of a light detector exposed to a source of ^{55}Fe. Thanks to the excellent energy resolution (FWHM = 250 eV at 6 keV) of this detector it is possible to separate peaks at 5.9 keV and at 6.5 keV due to the X rays of the calibration source.

8.2.1 The light detector

The idea to use a bolometer as light detector was first developed by C. Bobin et al. [86] and then optimized [87, 88] for Dark Matter (DM) searches. Starting from that work we developed a thermal light detector to be used for 0νDBD search [89]. It is made by high purity Ge wafers with a large area (to optimize photon collection) but a small mass (from 2.7 to 15 g) to reduce the heat capacity and therefore to have a sizable temperature increase upon photon absorption. The surface of the Ge wafers facing the scintillating crystal are darkened through the deposition of a $\sim$600 Å layer of SiO_2 in order to increase the light absorption.

The Ge wafer are too small to be able to detect the energetic gamma lines of the ^{232}Th source used for the calibration of the main crystals. Therefore a weak ^{55}Fe source was usually faced to the Ge wafers, on the side opposite to the crystal scintillator, for calibration purposes.

The ^{55}Fe calibration provides a method to measure and compare the LY's of different crystals. This cannot be used for an absolute evaluation of the amount of scintillation light emitted by the crystal since the light amplitude is not corrected for the photon collection efficiency. Moreover it is also possible that the thermal response to the high number of optical photons produced by scintillating crystal is different from that of an X-ray photon. Finally the energy resolution of the LD is measured as the FWHM of the 5.9 keV K_α X ray line. Depending on the detector used and on the working conditions, the resolutions

range from 200 eV to 600 eV FWHM. These resolutions are negligible if compared with the width of gamma and alpha lines in the light spectrum.

In Figure 8.5 is reported a calibration spectrum of a light detector exposed to a ^{55}Fe source.

8.3 Scintillating bolometer for 0νDBD

The possibility to reject α induced background open a new window in the future of 0νDBD with bolometers. Moreover, if the bolometric crystal is based on a 0νDBD emitter whose transition energy exceeds the 2615 keV γ-line of ^{208}Tl then the environmental background due to natural γ's will decrease abruptly (see Chapter 3).

These features allow to conceive "zero background" experiments for the 0νDBD searches. This very interesting possibility, combined with the excellent properties of bolometers as 0νDBD detectors, allowing the realization of very sensitive experiments.

Much of the work I have done during my PhD was then focused on the study of the properties of some scintillating crystals. The main characteristics considered for the choice of a crystal candidate to be a good 0νDBD detector are:

- **Q>2615 keV** to search the peak in a "zero background" region
- **good thermal response** to have an high energy resolution
- **high L.Y. and Q.F.** to be able to reject efficiently α background
- **big crystals** to conceive a large mass experiment
- **enrichment possibility** without excessive costs
- **low internal radioactive contaminations** to avoid background due to internal β/γ decays

Among the tested crystals those who gave best results and that will therefore be described in the following are: $CdWO_4$, ZnSe and some molybdates.

8.3.1 $CdWO_4$

$CdWO_4$ is an ideal candidate as scintillating bolometer for 0νDBD:

- it is a well established scintillator
- ^{116}Cd (7.5 % i.a) has a 0νDBD transition at 2805 keV
- the light yield (LY) is rather large

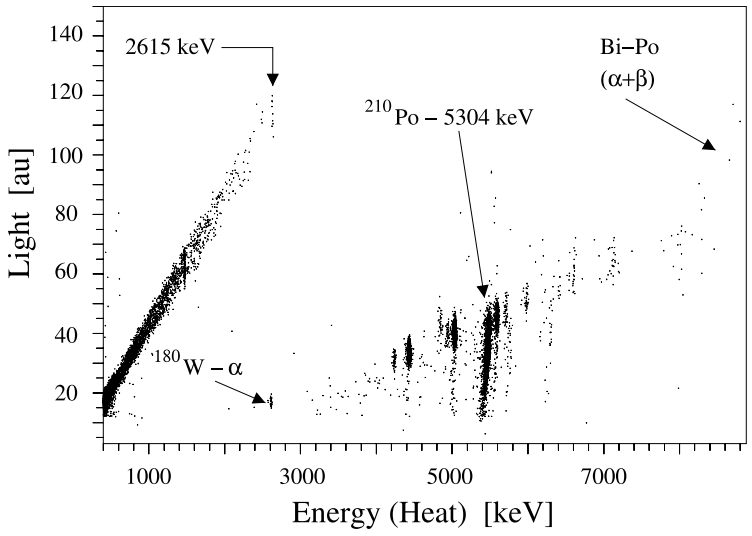

Figure 8.6: Scatter plot of heat (3x3x6 cm^3 $CdWO_4$, 426 g) vs light (collected by Ge light detector). Live Time ∼1066 h.

- the radiopurity of this compound is "naturally" high

Due to these favorable features this crystal compound was already used to perform a 0νDBD experiment [90] using "standard" Photomultipliers. A large mass experiment, based on enriched $CdWO_4$ crystals, readout by Photomultipliers, was also proposed [91]. However this technique, limited by the modest achievable energy resolution, key point of future experiments, is no more pursued.

Experimental details

In these years different $CdWO_4$ crystals were tested. The first measurements done in 2007 were made with a small size crystal (3x3x2 cm^3). The excellent results obtained have encouraged us to carry out new tests with an array of 4 crystals (3x3x3 cm^3) and a 3x3x6 cm^3 crystal to validate the possibility of measuring several scintillating crystals with a single light detector. Details on the setup and results of this measurement are reported in [92]. In Figure 8.6 the scatter plot obtained with the 3x3x6 cm^3 crystal is reported. As can be seen from the figure in this measurements it was possible to obtain a good discrimination between α particles and β/γ. Moreover we have observed some broad α lines with some events showing less scintillation light. These events are probably due to surface events. In fact this characteristic is evident in the 5304 keV α of ^{210}Po. The events belonging to that curve are certainly surface events. Comparing the shape of the lines due to internal contamination to those attributed to surface contamination we attributed this behavior to the surface quality of the crystal. This statement is also supported by

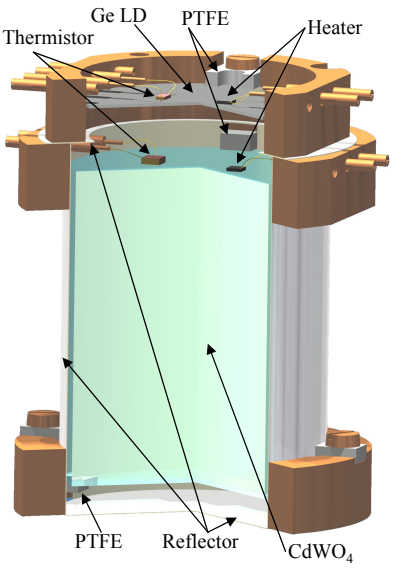

Figure 8.7: Setup of the detector. The two Cu columns, holding the two frames, are not visible from the chosen perspective.

the observations on other crystal with surfaces polished at optical grade. For this reason the new, cylindrical and bigger crystal (h = 50mm, ∅ = 40mm, 508g) tested has perfect optical surfaces. This has led to a significant reduction of the width of the alpha band compared to measurements made previously.

With this crystal several tests have been performed [93] that have yielded excellent results and therefore, in the following, I will focus exclusively on it.

The bolometric detector setup is schematized in Fig. 8.7. It is held by means of four L-shaped Teflon pieces fixed to the two cylindrical Cu frames. The frames are held together through two Cu columns. The Light Detector (LD) [89] is constituted by a 36 mm diameter, 1 mm thick pure Ge crystal absorber.

The energy calibration of the $CdWO_4$ crystal is performed using γ sources placed outside the cryostat. The heat axis is calibrated attributing to each identified γ peak the nominal energy of the line, as if all the energy is converted into heat. Consequently this calibration does not provide an absolute evaluation of the heat deposited in the crystal. The dependency of amplitude from energy is parameterized with a second order polynomial in log(V) where V is the heat pulse amplitude. The three coefficients of the polynomial are fitted on calibration data (the heat pulse amplitude corresponding to the known γ lines visible in the spectrum). The choice of such a function was established by means of simulation studies based on a thermal model of the detectors.

Three sets of data have been collected with this device: two calibrations using ^{232}Th and ^{40}K sources, a long background measurement (433 h) and a neutron measurement (8

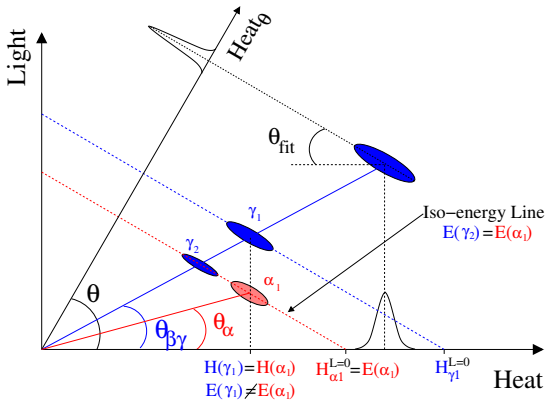

Figure 8.8: Light vs. heat scheme for the interpretation of the energy correction method. The blue (dark) spots represent the γ/β monochromatic events, while the red (light) represents an α.

h) done exposing the detector to an Am-Be source.

Scintillation Quenching Factor

The scintillation Quenching Factor for α particles was defined before as the ratio of the scintillating yield of an interacting α particle with respect to the LY of β/γ event at the same energy. As can be seen in Figure 8.8 where a typical $CdWO_4$ scatter plot is represented by an ideal diagram where alpha monochromatic lines are red spots and beta/gamma's are in blue, it could be expressed also as

$$QF_\alpha = \frac{tan(\theta_\alpha)}{tan(\theta_{\beta\gamma})} \tag{8.2}$$

This holds only in first approximation, as will be exposed later.

In our diagram we have represented a feature clearly evident in experimental scatter plots: within each band (beta/gamma or alpha), monochromatic events (i.e. those corresponding to the complete absorption of a monochromatic particle in the $CdWO_4$ crystal) appear as sections of lines with negative slope, showing a strong correlation between heat and light. This is evident in the light vs. heat scatter plot obtained with a source of ^{232}Th (Fig. 8.9) where different γ-lines are clearly visible. Despite the much lower statistics, the same feature is perceptible also for the α lines that appear in the background spectrum (Fig. 8.13).

A simple model accounts for the observed pattern. The energy E of a monochromatic particle, fully absorbed in the $CdWO_4$ crystal, is divided into two channels: a fraction (L) is spent in the production of light (photons) and a fraction (H) is spent in the production of heat (phonons). In absence of "blind" channels (i.e. channels in which the energy

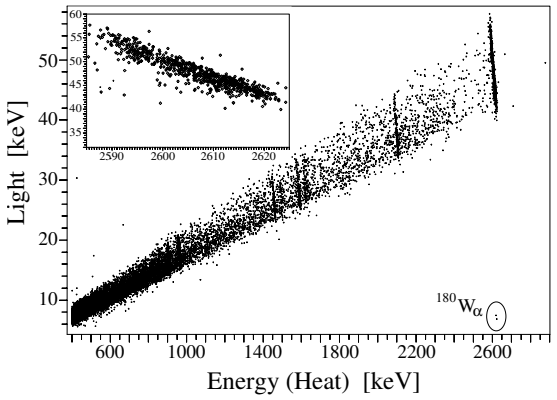

Figure 8.9: Scatter plot light vs. heat obtained in a 96 h calibration using an external ^{232}Th source. In the inset the highlight of the ^{208}Tl line. In the circle two events due to the internal α-decay of ^{180}W. The energy spectrum below 400 keV is completely dominated by the ^{113}Cd β-decay, with a rate close to 0.4 Hz.

deposited into the crystal is stored in some system that does not take part in signal formation) the energy conservation requires:

$$E = E_{Heat} + E_{Light} = (1-k)E + kE = H + L \tag{8.3}$$

being k the fraction of the total energy that escapes the crystal in form of light. The last equation states not only the energy conservation, but also a subtle distinction between the heat (what is measured) and the energy definition.

Monochromatic events should produce a spot in the scatter plot, with a size determined by the intrinsic energy resolution of the heat and light detectors. The observed spread along a negative slope line, however, can be accounted for assuming the existence of fluctuations in the H and L signal amplitudes. Since the energy has to be conserved the amplitude of the fluctuations (δL and δH) must compensate each other: δL=-δH. In other words the fluctuations are correlated between each other and produce the observed pattern. They are visible because their amplitude is much larger than the intrinsic resolution of the detectors.

We can devise two mechanisms that introduce a fluctuation in the L/H ratio:

- the statistical Poissonian fluctuation in the emitted light: the more the energy spent in light production, the less the energy spent in heat;
- any variation of the LY as those due to position dependent effects (inhomogeneities and defects of the crystals that modify the light emission or self absorption of scintillation photons).

Regardless the mechanism I will show in the next section how this correlation can be

used in order to increase (correct) the energy resolution of the detector over the entire energy spectrum.

Fig. 8.8 tries to summarize the model here discussed. The blue and red spots represent monochromatic energy deposition in the $CdWO_4$ crystal, as those observed during a γ calibration. For each of them a negative slope (iso-energy) line is tracked. The intercept on the heat axis ($H^{Light=0}$) is the heat that would correspond to a full heat conversion of the deposited energy (in absence of light emission or in the case in which all the light is absorbed by the crystal itself). In this simple model γ/β's and α's releasing the same energy within the $CdWO_4$ crystal lie on the same iso-energy line. But due to the larger LY, γ/β events will convert less heat within the crystal with respect to an α particle releasing the same energy: part of the energy escapes the crystal in form of photons. This feature can be easily deduced from Fig. 8.8: the α_1 particle release the same total energy of the γ_2 particle (they belong to the same iso-energy line) but they show a different position on the heat axis. In fact the α_1 shows the same heat of the γ_1 particle that releases a larger energy within the crystal. The "usual" picture (in which γ/β and α of the same energy show the same heat signal) corresponds to the limit in which the light emitted is negligible (or completely re-absorbed by the crystal): in this case the distinction between H and E becomes meaningless.

It is important to remark that up to now it was assumed to be able to measure the absolute values of energy converted into heat and light. In such a case, considering that δL=-δH the slope of the spots will be

$$tan(\theta_{fit}) = \frac{\delta L}{\delta H} = -1 \tag{8.4}$$

However, we have to take into account the calibration of the axes. Actually, the measured experimental heat and light signals can be written as

$$\begin{aligned} H &= \alpha(1-k)E \\ L &= \beta\epsilon kE \end{aligned} \tag{8.5}$$

being α and β the absolute calibration factors for the heat and light axes. The factor ϵ, instead, takes into account the overall light collection efficiency.

Under the condition that α and β are not depending on the energy, Eq. 8.5 implies that

$$tan(\theta_{fit}) = \frac{\delta L}{\delta H} = \frac{\beta\epsilon}{\alpha} \tag{8.6}$$

The last equation states that the effect of mis-calibrations of the heat and light axes simply implies a variation of the slope of monochromatic lines, which is exactly what is observed experimentally. Also the light collection efficiency plays a fundamental role in the evaluation of the slope.

As mentioned earlier, it is important to note that, unlike the heat channel, the LD energy calibration is more delicate. The energy calibration on this detector is performed using ionizing X-Rays from the ^{55}Fe source. A priori the thermal signal that arises by the absorption of 1 keV of photons at the boundaries of the Ge crystal (moreover covered by the SiO_2 layer) could give a different thermal signal with respect to a 1 keV ionizing energy.

Light-Heat correlation: energy resolution

The energy correlation between the two signals of a double readout system was already observed in ionization/scintillation detectors [94] as well as in heat/scintillation bolometers [95] with a device very similar to the one presented here. In the former case this correlation was demonstrated to improve the energy resolution by a factor close to ~ 25 % (evaluated at 570 keV). In the latter two different γ-lines were studied at rather low energy. An evident correlation was found but, however, the correlation factor of the two lines was found to strongly depend on the energy.

The energy correction procedure is graphically explained in Fig. 8.8. Here blue and red spots represent γ/β and α produced by monochromatic events. In order to obtain a spectrum with improved energy resolution we have to combine the heat and light values of each single event in an appropriate way. This can be obtained performing a rotation in the scatter plane an projecting the points on the Heat_θ and Light_θ axis:

$$\begin{aligned} Heat_\theta &= Heat \cdot cos\theta + Light \cdot sin\theta \\ Ligh_\theta &= -Heat \cdot sin\theta + Light \cdot cos\theta \end{aligned} \tag{8.7}$$

The value of θ can be evaluated in two different ways:

- it can be "optimized" in order to obtain the best energy resolution on the Heat_θ axis (energy resolution minimization)
- it can be obtained by fitting the monochromatic spots in the scatter plot with a negative slope line, evaluating the θ_{fit} angle for each single distribution (for construction we have $\theta = \pi/2 - \theta_{fit}$)

It is clear from this scheme that some assumptions should be satisfied in order for this procedure to work properly:

- the slope of each monochromatic spot (i.e. the θ_{fit} angle) or the θ angle minimizing the FWHM has to be the same within all the lines
- the LY of the different class of interacting particles (α's and γ/β) has to be independent from energy

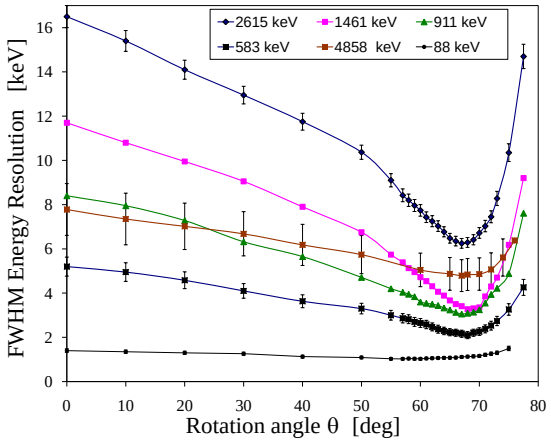

Figure 8.10: FWHM energy resolutions evaluated for different θ angles. For each angle a spectrum is produced and the corresponding peaks are fitted. The curves through the data points are only to guide eyes. For two peaks the corresponding error on the FWHM is not plotted for better clarity.

The first condition ensures that the rotation minimizes the FWHM on the whole energy spectrum. The second condition ensures that the projected spectrum keeps linearity and energy calibration. This point is less trivial and will be treated in more detail later.

Both the methods were applied in order to evaluate the rotation angle. Using the energy minimization method, the value of the rotation θ angle is allowed to vary over a wide range (0-80 degrees) and for each angle a spectrum is produced projecting the data on the Heat_θ axis. Finally the FWHM energy resolution of the more intense peaks is evaluated by a fit.

This method was applied not only to the calibration spectrum but also to the background measurement. In this way it was possible to study also the the 88 keV γ-line of ^{109}Cd (accidentally contamination in the $CdWO_4$ sample) and the α peaks due to internal trace contaminations: a line at the full energy of the decay (Q=α+nuclear recoil). The internal α-lines observed are ^{234}U-α(Q=4858 keV), ^{180}W-α (Q=2516 keV) and ^{238}U-α (Q=4270 keV).

In Fig. 8.10 is reported the FWHM energy resolutions evaluated on the most intense lines obtained varying the rotation angle θ and projecting on Heat_θ. The energy resolutions of the peaks are evaluated for each single rotated spectrum. The minimum of the energy resolution occurs within θ=(67.5 $\pm$ 0.5) deg for all the lines.

Each monochromatic events distribution in the scatter plot was also fitted with a linear function, as previously discussed. The θ_{fit} angles as well as the most relevant parameters of this analysis are summarized in Tab. 8.1. The values of the θ_{fit} angles for the α's and γ/β's lines reported are compatible within the experimental errors within the two

Line [keV]	FWHM$_{\theta=0}$ [keV]	FWHM$_{\theta=67.5}$ [keV]	LY [keV/MeV]	$\pi/2-\theta_{fit}$ [deg]
88	1.4±0.08	1.11±0.06	17.3±0.2	61.6±0.9
583	5.2±0.4	2.1±0.2	17.0±0.35	70.8±0.4
911	8.4±0.5	3.05±0.2	17.5±0.2	70.6±0.3
1461	11.7±0.5	3.27±0.2	17.45±0.15	70.4±0.3
2615	16.5±0.5	6.25±0.22	17.6±0.1	69.8±0.2
2516	5.2±1.6 †	4.3±1.3 †	2.74±0.08	73.0±0.2 †
4270	7.0±1.5 †	4.4±1.0 †	3.29±0.07	72.3±0.2 †
4858	7.8±1.2 †	4.8±0.7 †	3.44±0.08	72.7±0.2 †

Table 8.1: Table with the main parameters of the detector. The theoretical FWHM energy resolution of the $CdWO_4$ crystal, evaluated through Optimal Filtering, is 0.8 keV. The LY of the α-particles (last three lines) is evaluated for the overall Q-value of the decay. The correct value (assuming negligible scintillation for the nucleus recoil) is $\approx 2\%$ larger.

groups (with the exception of the 88 keV line). However, with respect to the γ/β's, the angular coefficient calculated by fitting linearly the single lines gives a result that is systematically slightly larger with respect to the value (67.5±0.5) obtained through the energy minimization. This systematic small difference could arise from the fact that while the bidimensional fit is model independent, the energy minimization depends on the fitting procedure of the peaks. Moreover it should be pointed out that the quoted error on θ_{fit} don't include systematic effects (introduced, for example, by the continuum background) whose values could dominate the total error.

The values of the θ_{fit} angles reported in Tab. 8.1 seem to show a slightly difference between α and γ/β. However it has to be pointed out that the quoted error on the θ_{fit} for the α particles has a (further) systematic error that cannot be easily evaluated. The point is that the α events were collected during the long background measurement. During this period the $CdWO_4$ crystal was slowly cooling down (the LD, on the contrary, was rather stable during the same period). This drift is usually corrected through the Heater pulse. If the temperature drift is rather small (~ 50 μK) then the correction is independent from the energy. On the contrary, if the drift is larger (in this case the drift was ≈ 0.3 mK) then the shape of the signal changes appreciably. In such cases the correction starts to depend on the energy. As a consequence a small drift in function of the time (or the temperature) becomes appreciable. Moreover this drift depends on the energy. So, in order to evaluate the second, third and last column in Tab. 8.1 each α peak was "self-stabilized". This can introduce an uncontrolled systematics. On the other hand, a check was made on the weak 2615 keV γ-line present in the background spectrum. As in the case of the α's, we had

to self-correct the drift. The obtained θ_{fit} value is 71.5±0.4, rather consistent with the α background. For the following I will assume $\theta_{fit}^{\gamma/\beta} = \theta_{fit}^{\alpha}$. The ^{232}Th and ^{40}K calibrations on the other hand, were made at the end of the measurement in a rather stable working temperature.

As a final remark it has to be noticed that the projection of the events on the Heat$_\theta$ axis introduces an Heat (energy) normalization factor K that will be different for different classes of particles, namely $K_{\gamma\beta,\alpha}=\cos\theta(1+\tan\theta\ \tan\theta_{\gamma\beta,\alpha})$. This feature is rather evident in Fig. 8.8: in the heat axis $H(\alpha_1)=H(\gamma_1)$ while in the rotated Heat$_\theta$ axis we have $H(\alpha_1)=H(\gamma_2)$. This has two consequences: the first, obvious, is that the intercalibration between α and γ/β is different within the Heat spectrum and the Heat$_\theta$ spectrum. The second is that the same consideration holds within the same class of events: if the LY of α particles (for example) depends slightly on energy, then the linearity of the projected spectrum will change.

Light Yield and Scintillation Quenching Factor

In Tab. 8.1 are also presented the values of the LY, determined on the different monochromatic lines.

The table shows that the LY of the γ/β events is, within the error, the same for all the observed lines. On the other hand a small, but rather clear, energy dependence is evident for α particles. This effect can also be observed in Fig. 8.12 in which it is evident that the α particles belong to a curve rather than a straight line. Moreover, as already stated, the observed α-lines are internal so that the effect cannot be ascribed to surface effects. A theoretical explanation for this behaviour and a detailed discussion of the energy dependence of LY and QF in different scintillating crystals can be found in [96]. Essentially, the observed behaviour reflects the fact that an α particle scintillates less with respect to an electron because of its larger dE/dx which can induce saturation effects in the scintillator (the Birks law [97]). The energy dependence of the LY and QF is a consequence of the energy dependence of the stopping power. Electrons, due to their low stopping power, do not suffer of saturation effects and their LY is, consequently, energy independent. For this reason the definition of $QF_\alpha=\tan(\theta_\alpha)/\tan(\theta_{\beta\gamma})$ represents only an approximation.

Using the values in the table we can evaluate the scintillation Quenching Factors of α particles (QF=LY(α)/LY(β)):

$$\begin{aligned} QF(^{180}W) &= 0.160 \pm 0.006 \\ QF(^{238}U) &= 0.192 \pm 0.006 \\ QF(^{234}U) &= 0.201 \pm 0.006 \end{aligned} \tag{8.8}$$

Within this framework, furthermore, it is possible to evaluate the total amount of

light k that escapes the crystal. Using Eq. 8.6 and considering that, for definition, LY≡L/E=$\beta\epsilon k$:

$$LY = tan(\theta_{fit})\alpha k \tag{8.9}$$

However the energy calibration adopted for the Heat axis (as discussed in Sec. 8.3.1) implies H≡E. This means (see Eq. 8.5) that α=1/(1-k_γ), being k_γ the absolute LY for γ/β events. Using this last relation in the last equation

$$k_\gamma = \frac{LY_\gamma}{tan(\theta_{fit}) + LY_\gamma} \tag{8.10}$$

The k_γ obtained using the values of Tab. 8.1 is k_γ= 4.6 %

As a final remark, it is important to note that the large spread in the light channel (6.8 % at the 2615 keV scintillation signal), as observed in the scatter plots, cannot be dominated by the fluctuation of the Poissonian statistics of the absorbed photons. In fact the mean energy absorbed by the LD for a 2615 keV interaction in $CdWO_4$ is of the order of 2.615 MeV·17.6 keV/MeV= 46 keV. Assuming ≈ 3 eV/photon the variation in the light channel is of the order of $1/\sqrt{46000/3}$=0.8 %. Moreover in other tests performed with different $CdWO_4$ crystal samples was observed the same correlation (in terms of θ_{fit}) but with a much smaller spread. Thus the magnitude of this spread is probably dominated by fluctuation in the overall light collection efficiency.

Heat absolute scale and Heat Quenching Factor

From the previous sections is evident that for scintillating bolometers the Heat/Energy scale is different for different kinds of interacting particles (or, better, for particles characterized by different LY's). In other words, with the usual calibration used also for non scintillating crystals, H measures the total energy of a γ/β particle while it doesn't for an α: the energy calibration of α-particles has to be dealt in a separate way.

This "displacement" for the α lines is evident in $CdWO_4$ data. In particular the ^{180}W-α line (as can be seen in Fig. 8.9), whose nominal Q-value is 2516 keV [98], appears (in the γ-calibrated spectra) at 2627±2 keV. This line is rather peculiar since it definitely proves that the mis-calibration cannot be ascribed to a wrong extrapolation of the detector amplitude vs. energy calibration (the highest γ-line used for the calibration of the Heat signal is indeed the ^{208}Tl line at 2615 keV).

The observed shift in keV, $\Delta E = E_\alpha - E_{\gamma/\beta}$, between the experimentally reconstructed energy and its nominal value is given, for the three mentioned α's, by:

$$\Delta E_{^{180}W} = 110 \pm 3 \qquad \Delta E_{^{238}U} = 172 \pm 3.5 \qquad \Delta E_{^{234}U} = 180 \pm 2 \tag{8.11}$$

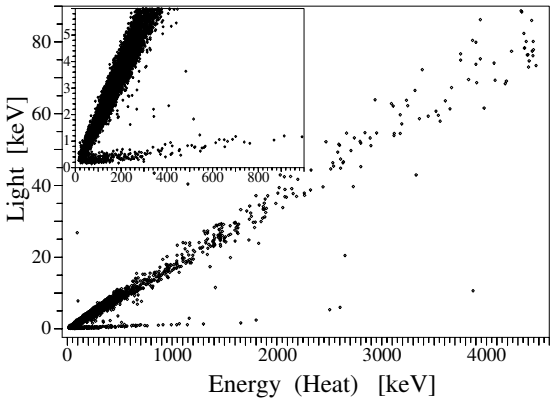

Figure 8.11: Scatter plot heat vs. light obtained in a 8 hour measurement with an Am-Be neutron source. In the inset the low energy region. The energy spectrum extends up to 9 MeV. The 4.44 MeV "line" due to the $^{12}C^*$ is visible. The intrinsic energy spread of this peak is rather large (≈ 1 %) due to Doppler shift induced by the "in flight" decay of $^{12}C^*$ in the source.

This shift can be easily recognized by looking at Fig. 8.8. In the case in which the crystal does not scintillate the two particles, α_1 and γ_1 will show, as example, $E(\alpha_1) < E(\gamma_1)$. If the crystal scintillates and the light escapes the crystal, then the two events will move left on the two different iso-energy lines up to reach the case in which H(α_1)=H(γ_1). This means that the energy shift can be written as $\Delta E = H_{\gamma 1}^{L=0} - H_{\alpha 1}^{L=0}$ and then

$$\begin{aligned} E_{\gamma/\beta}^{Light=0} &= E + \frac{Light_{\gamma/\beta}}{tan(\theta_{fit})} = E\left(1 + \frac{LY_{\gamma/\beta}}{tan(\theta_{fit})}\right) \\ \Delta E &= E\,[MeV]\ \cdot \left(\frac{LY_{\gamma/\beta} - LY_{\alpha}}{tan(\theta_{fit})}\right) \quad [keV] \end{aligned} \tag{8.12}$$

Inserting the experimental values we get:

$$\begin{aligned} \Delta E(^{180}W) &= 107 \pm 3 \\ \Delta E(^{238}U) &= 175 \pm 6 \\ \Delta E(^{234}U) &= 195 \pm 7 \end{aligned} \tag{8.13}$$

These last values are in very good agreement with the experimental ones in Eq. 8.11, confirming the model.

Background Rejection: α's and neutrons

To evaluate the rejection efficiency the detector was exposed to a neutron source. It consists of a 185 kBq Am-Be source with a neutron production rate of ≈10 n/s. The neutron spectrum has its maximum at ∼5 MeV with an high energy tail reaching 10 MeV.

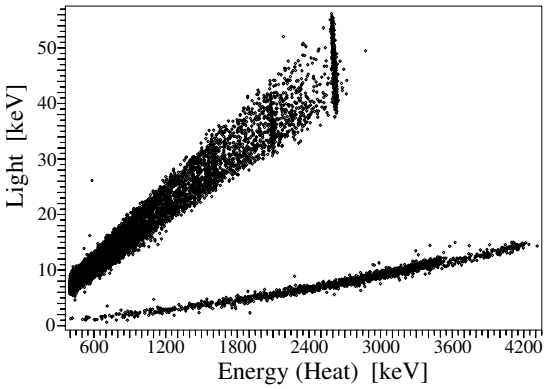

Figure 8.12: Scatter plot light vs. heat obtained in a 93 hours ^{232}Th calibration measurement with a smeared α source facing the $CdWO_4$. The liquid standard also contains a small amount of ^{234}U. The alpha curve is completely separated from the γ/β line. Moreover it can be noted that the α events are not belonging to a straight line, showing a decrease of the QF with the energy, as discussed in Sec. 8.3.1.

The source was placed inside the shielding of the cryostat, in the same place where the γ sources are inserted. The scatter plot is shown in Fig. 8.11: neutron direct interactions are clearly visible, especially in the inset. The γ/β events extends well above 2615 keV due to (n,γ) reaction on the surrounding materials but, mainly, by the source itself: for each neutron produced there is 60 % probability to produce an excited state of ^{12}C that emits a γ of 4.44 MeV.

Moreover it has to be remarked (see also Sec. 8.3.1) that ^{113}Cd has a huge neutron capture cross section, with a Q-value larger than 9 MeV, so that "mixed events" are possible (e.g. a neutron scatters on the Oxygen of the crystal and then is absorbed by the ^{113}Cd with subsequent de-excitation of the nucleus). The neutron scintillation QF with respect to γ/β was evaluated to be (0.14$\pm$0.03). The error is dominated by the systematics induced by the extreme weakness of the scintillation light in the region 0$\div$300 keV, where most of the events are recorded.

In a subsequent test the α source B, described in section 8.2, was mounted close to the detector in order to evaluate its rejection capability. The source was then faced to the crystal on the face opposed to the LD. In Fig. 8.12 is reported the scatter plot obtained with the above mentioned source during a 93 hours ^{232}Th calibration measurement. Remembering the definition of the discrimination confidence level (D_{Light}) given above (Eq. 8.1), the D_{Light} obtained in this measurements at 2615 keV is 12.6 σ. As far as the fast neutron interaction is concerned, the rejection factor will be obviously larger, but the most dangerous contribution will arise from thermal neutron absorption through ^{113}Cd. But, at least in principle, thermal neutron can be effectively shielded while fast neutron, via

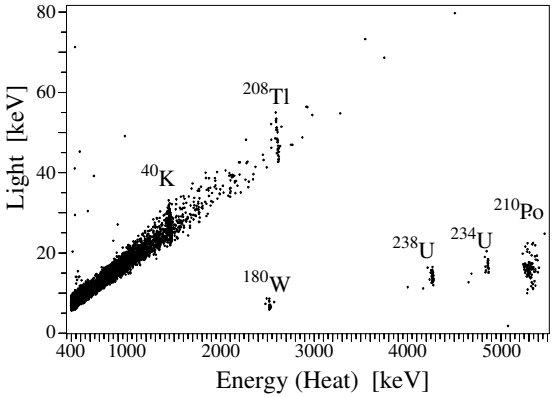

Figure 8.13: Scatter plot light vs. heat obtained in a 433 hours live time background measurement. Part of the ^{210}Po "bump" is characterized by smaller light emission. This could arise from a worse light collection efficiency, especially from the lateral part of the crystal. The energy scale of the α is corrected according with what exposed in Sec. 8.3.1.

μ-spallation within the shielding or close to it, cannot.

Background measurement: internal contaminations

In Fig. 8.13 the light vs. heat scatter plot obtained in the 433 h live time background measurement is reported. Only two α decay belonging to the Uranium chain, namely ^{238}U and ^{234}U are recognized. They correspond to an internal contamination of $3.1{\cdot}10^{-12}$ g/g and $5.7{\cdot}10^{-17}$ g/g, respectively. The Uranium chain is broken at ^{234}U, while a contamination of ^{210}Po is clearly seen. No events can be ascribed to the Thorium chain, giving a limit of $9{\cdot}10^{-13}$ g/g (95% CL) for ^{232}Th, one of the most "dangerous" contaminant for 0νDBD searches.

But the main (unexpected) feature resulting from Fig. 8.13 is the γ/β background above 2615 keV. These 11 events cannot arise from external γ's due to ^{208}Tl or ^{214}Bi since the observed background lines (583 keV, 2615 keV and 1764 keV) are too weak to allow such contribution at high energy. The same holds for internal contaminations belonging to Th and U chain. Unrecognized pile-up of the ^{113}Cd-β decay (Q= 320 keV) with a 2615 keV γ cannot contribute at this level (expected $\sim$ 2 ev/year). Internal contaminations due to rare high-energy β emitters like ^{106}Rh (Q=3541 keV) are extremely difficult to evaluate. On the other hand in previously tested $CdWO_4$ scintillating crystals was obtained, with larger statistics, no events above 2615 keV. The main difference with respect to these measurements [92] is that in this one the environmental neutron shielding (consisting of 7 cm of polyethylene and 1 cm of CB_4) was removed from the top of the cryostat, leaving $\sim$0.6 m^2 opening, corresponding to $\approx$ 8 % of the total neutron shielding.

8.3.2 ZnSe

^{82}Se is a $\beta\beta$ emitter with a natural isotopic abundance of 9.2% and a Q-value of (2995.5±2.7) keV [103]. It has always been considered a good candidate for 0νDBD studies because of its high transition energy and the favorable nuclear factor of merit. Indeed, the more recent evaluations of the Se nuclear matrix element (NME), yield for this isotope a half-life in the range 1-8·10^{26} y for an $|\langle m_\nu \rangle|$ value of 50 meV [26, 27, 28, 29] (in the same condition the predicted half-life for ^{76}Ge is about 4 times larger).

In recent years the NEMO collaboration measured its half life for 2νDBD to be 9.6±0.3(stat)±1.0(syst)·10^{19} y and set an upper bound on the 0νDBD half-life of 1.0·10^{23} y at 90% C.L. [104].

Experimental details

To study ZnSe bolometers [110] we used mainly three different crystals whose characteristics are reported in Table 8.3.2. The crystals have been produced by Alkor Technologies (Saint-Petersbourg, Russia) and are undoped (usually ZnSe is doped with Te). Their color variation is not fully understood but could be ascribed to a different stoichiometry [106].

ZnSe is a semiconductor with a Debye temperature of about 270 K [107] (not much different from TeO_2), known as a luminescent crystal since many years [108]. Its X-ray induced luminescence has been recently measured from room temperature down to 10 K, resulting in a dominant emission in the red region (610 and 645 nm) and a smaller component in the infrared region (970 nm) [106]. The Light Yield of this crystal (measured on small pieces cut from the same ingot from which the Small ZnSe crystal was obtained) was observed to increase at low temperature, with an emission characterized by more than one decay constant [130].

crystal name	crystal color	mass [g]	diameter [mm]	height [mm]	surface quality
Small	yellow	37.5	20	21	O O O
Large	red	120	41	17	O R R
Huge	orange	337	40	50	O O O

Table 8.2: ZnSe crystal characteristics. In the last column the surface quality is indicated for the lateral surface and the two basis of the cylinder respectively. O stands for optical and R for rough.

A group of more than 10 cryogenic runs, with a duration ranging from 1 month to few months, have been realized. In all these runs the bolometers worked properly, proving

that this crystal bears thermal cycles without a deterioration of its performances, whereas it exhibits an abnormal cooling slowness.

ZnSe bolometers and the heat signal

In each run, the ZnSe bolometers were calibrated with a ^{232}Th source placed between the cryostat and its external lead shield. Gamma lines between 238 keV and 2615 keV were used for amplitude (V^{heat}) vs. energy (E) linearization of the heat signal. The response of the bolometer is indeed slightly non linear, mainly because of the exponential dependence of the NTD thermistor resistance from temperature. In Figure 8.14 is reported the ratio V^{heat}/E vs. E (where E is the full energy of the corresponding gamma peak) observed for one of our detectors. The points with $E < 3$ MeV correspond to gamma peaks identified in the heat signal spectrum, the others correspond to alpha lines (these are due to the A α source described in section 8.2). The non linearity measured on gamma lines is here of about 3% on a 3 MeV energy range. Non linearities of the same order of magnitude are observed for all the other detectors. As it is usually done for other bolometers [36, 93], the non-linearity is corrected by introducing the calibrated amplitude of the heat pulse. It is worth to note that in this way the heat signal is attributed to the nominal energy E of the detected gamma line, i.e. the calibration returns heat=E for gamma particles. Here E is the total energy lost within the crystal, while only a fraction of it is converted into heat. The other fraction is spent in scintillation light or in possible blind channels such as long living metastable states. The result obtained after the calibration is shown in Figure 8.14: the colored circles are the ratio $Heat/E$ for each gamma and alpha line. The calibration returns, as expected, $Heat/E \sim 1$ for all the gamma lines. While for alpha lines $Heat/E > 1$ (all the points with $E > 3$ MeV in Figure 8.14). This means that alpha lines appears in the $Heat$ spectrum with a displacement of about 1 MeV, i.e. for the same total energy deposition in the crystal, heat pulses due to alphas are higher (by a factor $\sim$1.15) than heat pulses due to gammas. Provided that it was observed for alpha particles a higher light signal, this behaviour is quite strange. This feature is instead well explained in all the other tested scintillating crystals as, for example, in the case of $CdWO_4$ crystals (section 8.3.1).

The energy resolution on the heat signal was evaluated measuring the FWHM of the 2615 keV line in the heat spectrum. The peak FWHM was evaluated by a fit with an asymmetric gaussian. The best resolutions measured (average of left and right FWHM) for the Large and Huge crystals were of 21$\pm$2 keV and 28$\pm$1 keV respectively (see filled histogram in Figure 8.15).

In the case of the ZnSe Small crystal it was no possible to evaluate the energy resolution because no gamma peak is visible in the calibration or background spectra. This is explained by the small dimensions of the crystal and its low Z.

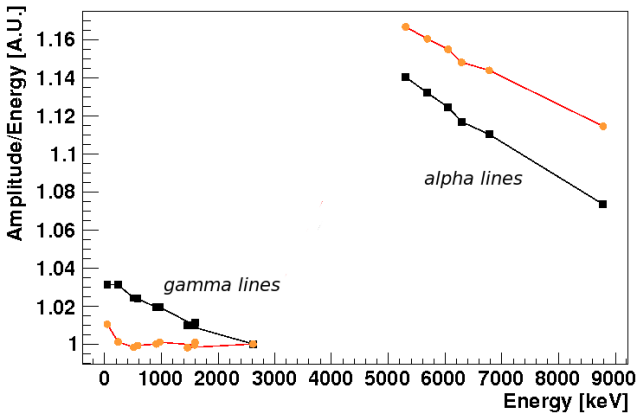

Figure 8.14: Non linearity behaviour of the ZnSe bolometer. On the X axis the nominal energy (E) of gamma (^{232}Th and ^{40}K) and alpha (source A) lines. On the Y axis the ratio between V^{heat} and E (black squares) before the energy linearization of the bolometer response (the ratio is normalized at 1 for the 2615 keV peak). For the same lines the ratio between $Heat$ and E is reported (colored circles). These data refer to the Large ZnSe crystal. A similar behaviour is observed for all the other detectors: the gamma pulses show a non linearity of the order of 3 % on a 3 MeV range, the alpha lines have a similar non linearity but a completely different energy calibration. The experimental errors are of the order of 0.1-0.2 % and are not visible in the plot.

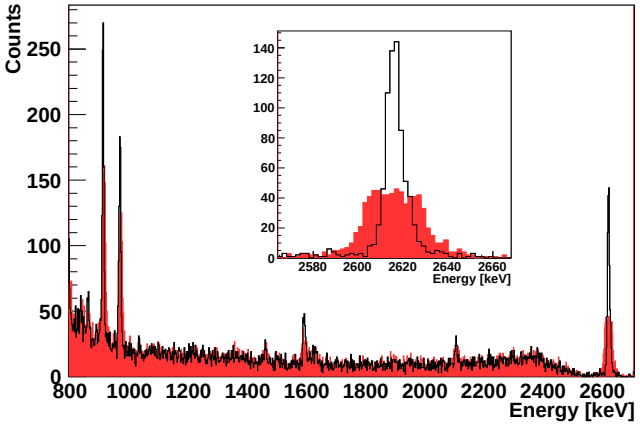

Figure 8.15: ^{232}Th gamma calibration of the Huge ZnSe crystal. The filled histogram is the projection - on the $Heat$ axis - of the events visible in the scatter plot of Figure 8.16 (right panel). The black line histogram is obtained as projection on the $Heat_\theta$ axis. In the inset the highlight of the 2615 keV line. The gain in resolution on all the lines is evident.

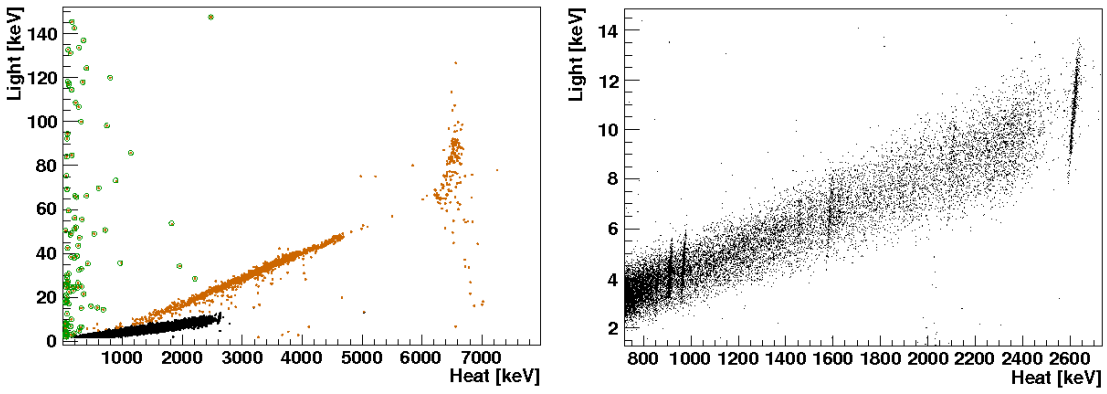

Figure 8.16: Scatter plot light vs. heat recorded with the Huge ZnSe crystal. The detector was here exposed to the B alpha source and to the calibration gamma source (^{232}Th located outside the refrigerator). Three populations of events have been marked: black spots for beta/gamma's, colored spots for alphas, circles for events with an ionization component in the LD. In the right panel a zoom of the beta/gamma band. The gamma lines due to ^{232}Th are clearly visible. The slope of all the lines is positive.

Results

Measurements performed with these crystals aimed mainly at the study of the alpha vs. beta/gamma discrimination properties of ZnSe, at the evaluation of the LY and of the Quenching Factor, and at the study of the variation of these properties upon variation of the crystal color and surface quality. In order to be able to compare the detector response to alpha and beta/gamma particles, in most of the runs, the crystals were faced to the A and B alpha sources (while gammas were generated with the external ^{232}Th source used for calibration).

The light vs. heat scatter plot of the ZnSe Huge crystal, exposed to the calibration gamma source (^{232}Th) and to the alpha source B, is shown in Figure 8.16. This scatter plot (as well as all the others obtained with ZnSe crystals) is completely different from any other we ever measured with different scintillating crystals. Three anomalies are indeed here evident:

- monochromatic gamma peaks lie on positive slope lines (right panel of Figure 8.16), whereas a negative slope is expected;
- the alpha band lies above the beta/gamma band, suggesting an alpha QF larger than one (left panel of Figure 8.16);
- alphas are always accompanied with a tail that draws negative slope lines (Figure 8.19).

Crystal	ZnSe Small	ZnSe Large	ZnSe Huge
LY [keV/MeV]	1.3	7.5	4.6
QF_α	4.4	4.2	3

Table 8.3: LY_γ measured on the 2615 keV line of ^{208}Tl (^{232}Th) and QF_α measured for the 5.7 MeV alpha line of ^{224}Ra. For each crystal we report values measured in similar experimental conditions: with the LD mounted on the top of the crystal and the alpha source facing the opposite side. The experimental errors on LY_γ and QF_α are of the order of 5% and 10% respectively. In the case of the ZnSe Small and Large crystals we were also able to compare directly their LY_γ in a dedicated run, where their scintillation photons were detected by the same Ge wafer (6 mm in diameter). The results where consistent with what reported in this table.

The anomalies resulted reproducible for the three crystals, despite the different crystal color and size and despite the different experimental conditions.

Correlation between heat and light and energy resolution on gammas

As already explained in detail in the case of $CdWO_4$ crystals, in standard scintillators, monochromatic events appear as sections of lines with negative slope.

In ZnSe crystals the slope of gamma lines is clearly positive (see right panel of Figure 8.16): for a monochromatic event the minimum heat release corresponds to the minimum of light emission, and vice-versa. Despite this unusual behaviour, also in this configuration a rotation of the axis can be used to improve the energy resolution of the detector.

Figure 8.15 shows (filled histogram) the spectrum obtained projecting the gamma events of Figure 8.16 on the $Heat$ axis. The black line histogram is obtained by projecting events on a rotated axis ($Heat_\theta$) where the rotation angle θ is chosen in order to reach the minimum FWHM for the 2615 keV. The improvement obtained on the resolution is of about a factor 3 on the 2615 keV line of ^{208}Tl (the FWHM is reduced from 28±1 keV to 9.5±0.4 keV). On the other peaks the improvement is smaller: at 911 keV from 7.8±0.6 keV to 5.9±0.3 keV, at 583 keV from 7.5±0.5 keV to 5.4±0.3 keV. Provided that it is proved that also 0νDBD events would give rise to a monochromatic line with the same slope, this technique could be used to improve the resolution of the detector.

Light Yield and anomalous light emission from the alphas

As discussed previously, we do not have an absolute calibration of the light signal, therefore we can provide only a relative evaluation of the Light Yield. The results for the 3 crystals are reported in table 8.3.

The QF_α obtained for the Small, Large and Huge crystals, for an identical position of the alpha source (i.e. facing the crystal basis opposite to the LD) are also reported in table 8.3. QF_α values are definitely larger than 1, and this unusual feature is accompanied by other peculiar behaviours extensively investigated in several dedicated runs. To our knowledge no other scintillator with a QF_α definitely higher than 1 have ever been reported in literature, and this feature cannot be easily accommodated within the theoretical framework used to describe the scintillation properties of materials. Indeed heavy particles usually have QF lower than one and this is explained on the basis of a saturation effect due to the high ionization density that characterizes the interaction of heavy particle in matter [97].

A possible way to explain a QF_α larger than 1 could be related to the experimental configuration, in some way privileging the collection of photons emitted by the point-like external alpha source with respect to the light produced in crystal bulk by gamma rays. For this reason different measurements was done to investigate the light collection, the self-absorption of the scintillation photons inside the crystal and the transparency of the LD's to the scintillation photons. In more detail:

- a self-absorption of the light inside the scintillating crystal could penalize gamma interactions (that take place in crystal bulk) with respect to alpha ones (alphas come from external sources and interact in a thin surface layer). To investigate this effect the alpha source was placed on the side opposite to the LD in such a way that only the light traversing the crystal could be detected. All the QF's reported in table 8.3 have been measured in this configuration.

- to check possible problems arising from light collection a measurement done with the ZnSe Huge crystal was compared with a measurement done with the $CdWO_4$ crystal. The two crystals have the same dimensions. Both crystals were mounted in a completely identical configuration with the same LD. The result was a normal behaviour in the $CdWO_4$ crystal and an anomalous one in the ZnSe. The LY measured for the $CdWO_4$ crystal was 17 keV/MeV. Consequently, ZnSe has a light emission on gammas that is four times lower than the one recorded with $CdWO_4$, while the light emission on alphas is nearly two times larger.

- the low LY measured could be due to a dominant beta/gamma photon emission on a wavelength to which the LD is partially transparent. The Ge wafers are completely opaque to the red light that, as measured upon X-rays excitation [106], appears to dominate the ZnSe luminescence spectra. Nonetheless, at the very low temperature, something could change. To verify this hypothesis was done a test using, as LD, a sapphire bolometer covered with a lead substrate (completely opaque from IR to UV). No relevant modification in the measured LY's and QF's was observed.

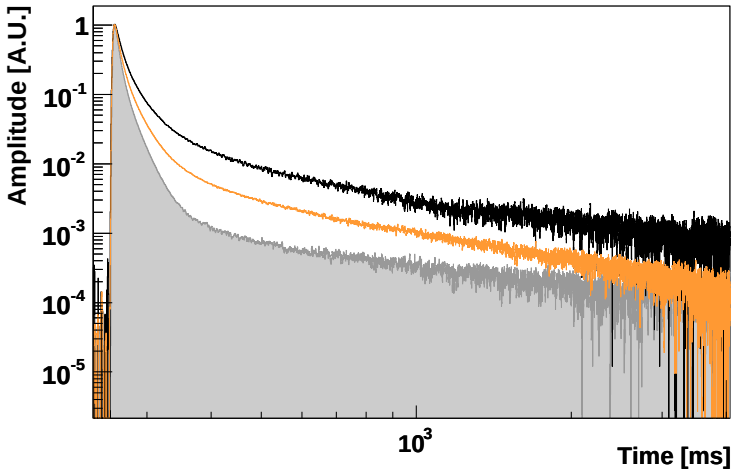

Figure 8.17: Averaged light pulses from beta/gamma (black line) and alpha (colored line), after pulse height normalization. In shadow the response function of the LD, as obtained averaging pulses due to direct ionization in the Ge wafer. The real shape of the light signals shall be obtained by deconvolving the signal with the response function of the detector. The time window is 4 sec. wide.

All the measurements, and consequently the above reported considerations, have been based on external alpha sources since it has never observed an internal alpha line. A possible explanation to this is that bulk alphas do not scintillate. In this case it should be seen a heat signals in anticoincidence with light ones. These dark counts are present in the spectra, but with the same percentage in the alpha and gamma region. They can in fact be ascribed to a light-heat coincidence lost due to trigger inefficiency on one of the two channels.

Finally, it must be taken into consideration that the QF_α may depend on the parameter used to measure the energy content of the recorded pulse (i.e. the pulse amplitude). In a very naive model of the bolometer, that assumes an instantaneous energy deposition in a monolithic device [112], the amplitude is proportional to the energy released in the crystal. However, this is only an approximation and, as will be extensively discussed in Chapter 9, do not hold. Indeed a clear difference between the shape of alpha and beta/gamma light pulses was observed. Figure 8.17 shows averaged alpha and beta/gamma light pulses having the same heat amplitude (and consequently produced by particles releasing in the scintillator almost the same energy). Once normalized to the same light amplitude the two signals show a quite different area. If the area, and not the amplitude of the pulse, would be used as an estimator of its energy content the QF_α would result lower than reported in table 8.3 (by about a factor 1.5), although still much higher than 1. It could therefore

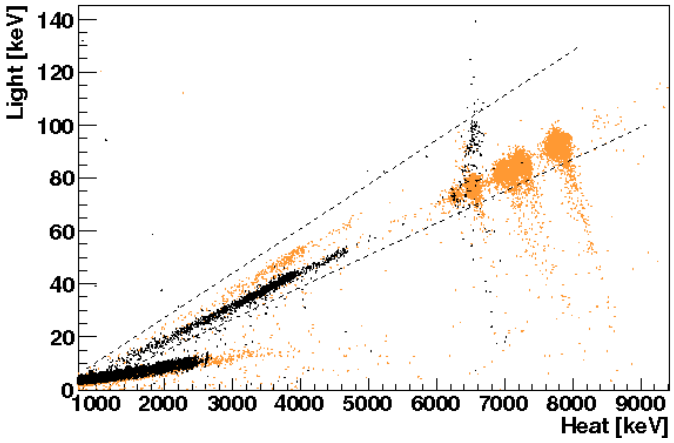

Figure 8.18: Scatter plot of light vs. heat recorded with the Huge ZnSe crystal in two different runs. In run I (colored points) the B alpha source was mounted on the bottom side of the crystal, opposite to the LD. In run II (black points) source B was moved on the side of the crystal and in its place was mounted source A. The dotted lines identify the opening of the alpha band on a wide angle, due to the variation of the QF_α upon source position.

be argued that, upon collection of all the light emitted by beta/gammas, the QF_α could approach a more standard value.

For the sake of completeness, a strange behaviour of the QF_α in ZnSe:Te (Tellurium doped Zinc Selenide) was already reported in literature. In particular, Sysoeva [113] quote a QF_α=1.05. While W. Klamra et al. [114] quote a QF_α=0.74-0.69, depending on the shaping factor of the amplifier. It is however very difficult to compare these results with those reported in literature. There are indeed two key aspects that have to be pointed out:

- all the measurement performed were carried on extremely thin crystals (1-2 mm). This because the transmission band of ZnSe, at room temperature, is very close to the emission band (while at low temperatures the crystal becomes almost transparent at the 610 nm wavelength of the dominant emitted radiation).

- these measurements are done on undoped ZnSe crystals at extremely low temperatures, while most of the literature concentrates on doped samples measured at much higher temperatures.

QF dependence on source position

Figure 8.18 compares the results obtained with the same detector changing only the position of the alpha sources. In run I the B alpha source was mounted on the bottom side of the crystal, opposite to the LD (this is the same scatter plot reported in Figure 8.16). In run II source B was moved on the side of the crystal, while in its previous position was mounted source A. By comparing the QF_α obtained for the two positions, it is clearly evident a variation of the order of 20%. This indicates that, in the case of a source distributed uniformly around the crystal (and not point-like sources like those we are using), it should be observed an alpha band spanning a much larger angle.

In Figure 8.16 and Figure 8.18 it is possible to observe the presence of background alpha events forming a positive slope line (similar to the ones observed for gamma particles) at heat ~ 6.2 MeV and light ~ 80 keV. This region corresponds to a nominal alpha energy of about 5.3 MeV, which is the energy of the alpha decay of ^{210}Po. This line can be ascribed to a ^{210}Pb contamination, a quite common contaminant whose strongest signature is the alpha emitted by ^{210}Po . The line has an evident tail (with negative slope) toward low light - high heat signals, an indication that it is due to a surface contamination. A reasonable assumption is that the source is a ^{210}Pb surface contamination of the crystal or of the mounting structure surrounding the crystal. In this case, the extension of the line on the light axis can be interpreted as due to the variation of the QF_α as a consequence of a position dependence.

The dependence of QF_α on the source position could in principle be due to a difference in photon collection efficiency, however in a test run done with two LD (where therefore the collection efficiency was definitely improved) the extension of the ^{210}Pb line on the light axis was not observed to change. Moreover, upon changes in the alpha source position, it was observed a variation not only in QF_α but also in pulse shape (the decay time of the light signals). All this gives credit to a second hypothesis: that the variation of QF_α upon source position is due to position dependence of LY_α (a similar effect is discussed in [115]) or to the self-absorption of the emitted light.

Low light tails of the alphas in the scatter plot

As consequence of the 'inverse' QF_α the separation of the alpha band from the beta/gamma one is not complete. This is evident looking at monochromatic alpha lines, like those produced by source A. For each alpha line, it was observed a spot plus a long tail of events, with lower light and larger heat, that draws a negative slope line on the scatter plot (see Figure 8.19). Obviously the same effect produces, in the case of source B, a continuum without evident structures below the alpha band. This feature is potentially dangerous since it could reduce the efficiency rejection of α particles. However, as already observed for $CdWO_4$ crystals, this problem appears to be connected to the quality of crystal surface

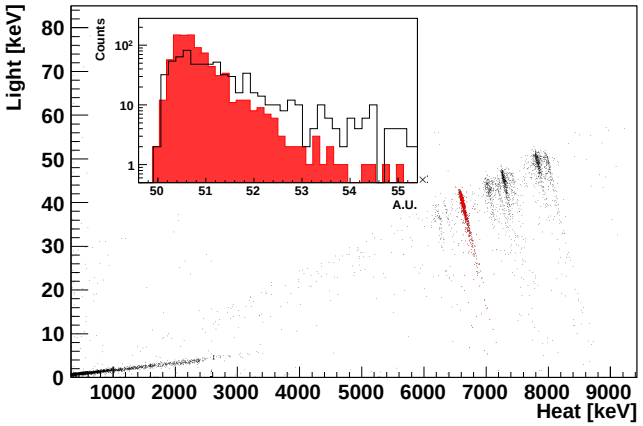

Figure 8.19: Scatter plot of light vs. heat recorded with the Large ZnSe crystal. The detector was here exposed to the A alpha source and to the calibration gamma source (^{232}Th located outside the refrigerator). Each alpha peak comes with a tail that draws a negative slope line in the scatter plot. In the inset: histogram of the events belonging to the 5.7 MeV alpha line (colored spots) projected along their negative slope line. The two histograms have been obtained for the same source (source A) and the same detector. The only difference being that in the case of the black histogram the non optical basis of the ZnSe cylinder was in front of the source, while in the case of the colored histogram it was the optical basis that faced the source (the scatter plot refers to this latter configuration).

(or to the presence on the surfaces of residuals of the abrasive, non-scintillating, powder used for polishing). Indeed the fraction of events populating the tail toward low light emission is different (for the same crystal) if the alpha source hits an optical face of the detector or a rough face. Figure 8.19 illustrates the test done and its results. The problem persists, although in reduced size, also in optical crystals as is the case of the ZnSe Huge.

8.3.3 Molybdates

^{100}Mo is one of the most promising 0νDBD isotope because of its large transition energy $Q_{\beta\beta} = 3035$ keV [117] and a considerable natural isotopic abundance (9.67%) [118].

Nowadays the best sensitivity to 0νDBD decay of ^{100}Mo is the one reached by the NEMO experiment [37] that, with $\simeq$7 kg of enriched ^{100}Mo, has obtained a half-life limit $T^{0\nu}_{1/2} > 4.6 \times 10^{23}$ yr at 90% C.L.. In this section I will describe measurements done with some molybdates crystals. Here I will only mention to the very interesting possibility to discriminate interacting particle by different thermal pulse shape observed in these crystals. A more detailed analysis of these results will be discussed in details in Chapter 9.

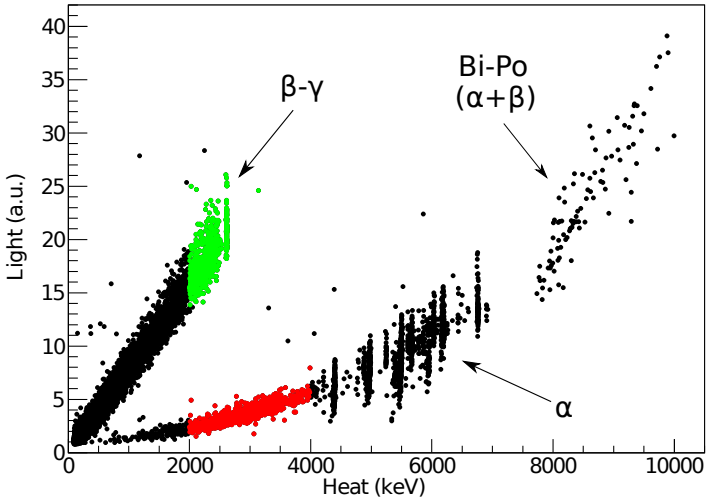

Figure 8.20: $CaMoO_4$ crystal. Scatter plot of light vs. heat. The energy calibration is performed on the γ peaks. In red (light in the bottom curve) events in the 2-4 MeV region due to α particles while in green events due to β/γ in the same region.

$CaMoO_4$

Recently $CaMoO_4$ has been intensively studied for its possible application as a scintillating bolometer for 0νDBD and Dark Matter experiments [102, 119, 116]. This crystal contains two isotopes that could undergo 0νDBD: ^{48}Ca ($Q_{\beta\beta}$=4.27 MeV) and ^{100}Mo ($Q_{\beta\beta}$=3.03 MeV). Contrary to what one might expect, this turns out to be a problem. Indeed, the natural isotopic abundance of ^{48}Ca (a.i.=0.19%) is too low to study the 0νDBD without enrichment, which is extremely difficult, and at the same time, it is too high to study the 0νDBD of ^{100}Mo, since the background due to the 2νDBD of ^{48}Ca in the 0νDBD region of ^{100}Mo will limit the reachable sensitivity for the latter isotope. A possible solution to overcome this problem was suggested by Annenkov et al. [120] who propose an experiment done with $CaMoO_4$ depleted in ^{48}Ca. Despite this, in the following I will report the results obtained with this crystal because of its extremely interesting capability to discriminate β/γ from α, thanks to the different shape of the thermal pulses.

The sample used was a cylindric $CaMoO_4$ crystal with a mass of 158 g (h = 40mm, $\varnothing$ = 35mm). The light detector consists of a 36 mm diameter, 1 mm thick pure Ge crystal absorber. The crystal was faced to A and B α sources.

In Fig. 8.20 is shown the light vs. heat scatter plot, collected while the crystal was exposed to a external ^{232}Th source. The total live time of this measurement was ~43 h. The FWHM energy resolution, on the heat signal, ranges from 2.7 keV at 243 keV to 8.7

keV at 2615 keV on β/γ events and is about 10 keV on 5 MeV α's. The light yield of the crystal, evaluated calibrating the light detector with a ^{55}Fe source, is 1.87 keV/MeV.

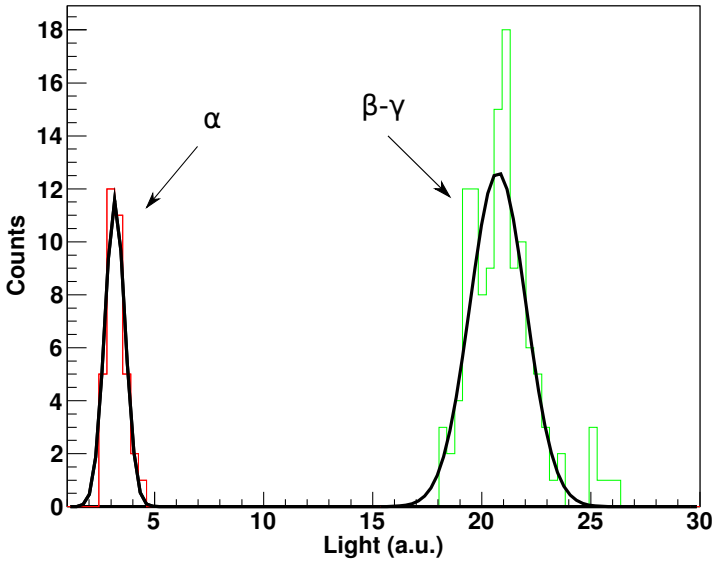

Figure 8.21: Evaluation of the β/γ and α discrimination power in $CaMoO_4$ by projection on the light axis of the ^{208}Tl γ-line (2615 keV) (in green) and of α events (in red) that released a similar energy in the $CaMoO_4$ crystal. The separation corresponds to 12.6 sigma.

The two separate bands, clearly visible in the light vs. heat scatter plot, are ascribed to β/γ's (upper band) and α's (lower band). The upper band is dominated by the ^{232}Th source γ's (plus the environmental γ's). The lower band is due to α's from source A and from Uranium and Thorium internal contamination of the crystal (these are the monochromatic lines above 4 MeV) and source B (the continuum counting rate below 4 MeV). Above 8 MeV we observe a group of events ascribed to $\alpha+\beta$ summed signals due to internal contamination in Bismuth and Polonium. Indeed, due to the long rise-time of this device (~5 ms), the beta decay of ^{214}Bi or ^{212}Bi (respectively of ^{238}U and ^{232}Th chains) followed immediately by α decay of ^{214}Po (τ=164 μs) and ^{212}Po (τ=298 μs), may lead to a pile up on the rise-time of the thermal pulses that hardly can be recognized as a double signal. The two decays produce therefore a single pulse, with an energy that is the sum of the two.

The discrimination confidence level, defined in 8.1, results to be for this crystal D_{light} = 12.6 σ at 2615 keV (see Figure 8.21). In the energy range where both the bands are populated (i.e. between 1 and 3 MeV), D_{Light}(E) appears to be linearly decreasing with

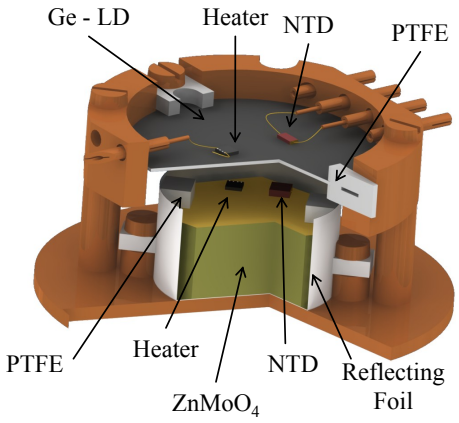

Figure 8.22: Setup of the detector ($ZnMoO_4$ crystal + light detector).

energy.

This discrimination power in the region of interest for the 0νDBD of ^{100}Mo is more than enough to completely ruled out the background due to α particles. However, the possibility to recognize the interacting particles by the shape of the thermal pulses is much more appealing than the discrimination due to the different light yield. For this reason in the Chapter 9 I will report the analysis done and the results obtained with this technique on this crystal.

$ZnMoO_4$

$ZnMoO_4$ crystals were developed only very recently [121, 122]. An important advantage of $ZnMoO_4$ is the absence of heavy elements and high concentration of molybdenum (43% in weight).

The sample used is a regular hexagon, with a diagonal of 25 mm and a height of 11 mm with a mass of 19.8 g. The color of the sample is fairly orange, showing evident inclusions along the central axis of the growth. The composite device (bolometer + light detector) is schematized in Fig. 8.22. The light detector consists of a 36 mm diameter, 1 mm thick pure Ge crystal absorber.

Two sets of data have been collected with this device [111]: a calibration using external ^{232}Th sources (65 h) and a background measurement (66 h). The intensity of the calibration sources was not optimized for small crystals, so that the statistics collected within the calibration peaks of $ZnMoO_4$ is rather poor. The energy resolution evaluated at 911, 2615 and at 5407 keV (^{228}Ac, ^{208}Tl and internal contamination of ^{210}Po, respectively) are 3.6±1, 5.6±2 and 6±1 keV, respectively. The FWHM energy resolution of the LD, evaluated on the X doublet at 5.90 and 6.49 keV, is 470±20 eV.

The LY of this crystal (measured on the 2615 keV ^{208}Tl line) can be evaluated as 1.1

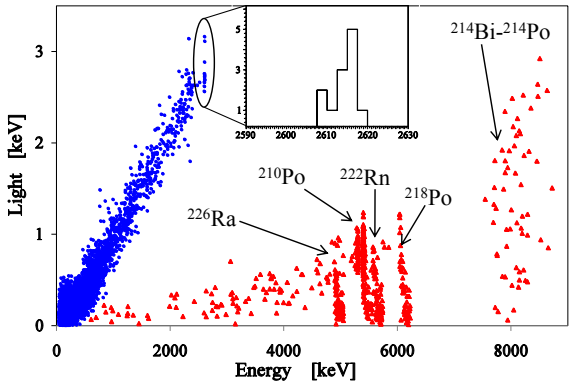

Figure 8.23: Scatter plot light vs. heat obtained with a ^{232}Th calibration (65 h) plus a background measurement (66 h). The main observed lines are pointed out. In the inset the 2615 keV γ-line of ^{208}Tl. The blue points are identified as γ/β events, while the red triangles are identified as α-particles. The BiPo points are due to mixed events induced by a γ/β decay "immediately" followed by an α decay.

keV/MeV. Even if this value is rather small it is evident from Fig. 8.23 that the continuous background induced by α-emitters located close to the surfaces is very efficiently recognized with respect to the γ/β events. The events in the α band are due to intrinsic radioactive contamination of ^{226}Ra, of the ^{238}U chain. The continuum below the ^{226}Ra peak can be ascribed to an alpha contamination in the surfaces of the mounting structure, producing degraded alpha particles with a continuous distribution of energies. ^{214}Bi-^{214}Po events are due to the fast decay chain of these two isotopes.

The α-lines are characterized by a tail that draws negative slopes "bands", as it is apparent in Fig. 8.23. This effect is extremely evident in the α-peaks induced by ^{226}Ra, ^{222}Rn and ^{218}Po. The "doublet" due to ^{210}Po, instead, shows this feature only, very marginally, on the full energy peak, at 5407 keV line. This behavior is likely when the contaminations are close to the surfaces, both of the crystal and of the the surrounding materials. The presence of large quantity of surface contaminants is corroborated by the large α-continuum background in the 2-4 MeV region, visible in the same figure. Nonetheless, by assuming, in a very conservative way, that all the observed α lines are induced by internal contamination, the values obtained are reported in Tab. 8.4.

It can be seen that, as it very often happens, the ^{238}U chain is broken at ^{226}Ra. With respect to the ^{232}Th decay chain, the most dangerous internal contaminant for this kind of detectors (see Chapter 3), it was only observed a limit.

Finally, as we will see in Chapter 9, also this crystal show the possibility to discriminate very well α and β/γ particles thanks to different thermal pulses.

Chain	Nuclide	Activity (mBq/kg)
^{232}Th	^{232}Th	≤ 0.3
	^{228}Th	≤ 0.3
^{238}U	^{238}U	≤ 0.2
	^{234}U	≤ 0.8
	^{230}Th	≤ 0.3
	^{226}Ra	8.1 ± 0.3
	^{210}Po	28 ± 2
Total α activity		73 ± 2

Table 8.4: Radioactive α activity of $ZnMoO_4$ crystal. The activity in ^{232}Th corresponds to a limit in the contamination of $7{\cdot}10^{-11}$ g/g. The contamination in ^{238}U has a limit of $2{\cdot}10^{-11}$ g/g. The observed ^{226}Ra contamination, instead, would correspond, assuming secular equilibrium, to a contamination of $^{238}\text{U} = 6{\cdot}10^{-10}$ g/g.

$MgMoO_4$

This compound contains, as in the two previous cases, the 0νDBD active isotope ^{100}Mo which is here present in a larger concentration ($\sim$52% in weight).

The tested crystal is 32x31x24 mm^3 and weight = 89.1 g. The total live time of this measurements was $\sim$22 h. In this run it was not possible to face the crystal to a light detector so it is not possible use the light vs. heat scatter plot in order to study LY, QF and discrimination power. Also the performances of the bolometer were quite poor, most probably this was due to a problem with the gluing of the NTD thermistor: at the end of the measurement, when the crystal was back to room temperature, I discovered that under the thermistor the crystal was broken. For this reason the signal to noise ratio was quite bad (the energy resolution measured on α lines was $\sim$150 keV FWHM).

Despite these problems I wanted to mention also the measurement made with this crystal because the favourable properties and the high concentration of ^{100}Mo. Despite signals in this measurements were quite bad, in Chapter 9 I will show how it was possible to discriminate interacting particle by pulse shape analysis demonstrating that the potential of this crystal are significant.

8.3.4 Summary of 0νDBD scintillating bolometer

The high number of results obtained with scintillating bolometers can make difficult an overview. For this reason, in this section, I will try to summarize them. The application of these results to the bolometric technique as a tool for the study of 0νDBD will instead be described in Chapter 10. However, before the analysis of 0νDBD applications I will

describe, in Chapter 9, the results obtained with the pulse shape analysis technique.

$CdWO_4$

We have performed different test with $CdWO_4$ crystals. Best results was obtained with a 508 g, cylindrical, crystal with optical surfaces. This $CdWO_4$, grown without any precaution in terms of radiopurity, shows extremely low trace contaminations in U and Th. The LY obtained in measurements done with this crystal, evaluated on all the γ lines, is $\sim$17 keV/MeV. On the other hand a small energy dependence is evident for α particles. This is a consequence of the energy dependence of the stopping power. The QF evaluated for the internal contamination in ^{238}U is 0.192. The discrimination confidence level results to be for this crystal D_{light}=12.6 σ. Moreover it was shown how the use of the correlation between light and heat improves the energy resolution by a factor 2.6 at 2615 keV. This allows to reach energy resolution $\sim$5 keV in the region of interest ($Q_{\beta\beta}(^{116}Cd)$ = 2805 keV). The excellent discrimination power together with the good energy resolution allow to envisage the use of this crystal for a future high sensitivity experiment for 0νDBD search.

ZnSe

ZnSe scintillating crystals present a number of anomalies or unexpected behaviours:

- monochromatic gamma peaks lie on positive slope lines
- the alpha band lies above the beta/gamma band, suggesting an alpha QF larger than one
- alphas are always accompanied with a tail that draws negative slope lines
- for the same total energy deposition in the crystal, heat pulses due to alphas are higher (by a factor $\sim$1.15) than heat pulses due to gammas. Provided that it was observed for alpha particles a higher light signal, this behaviour is quite strange

Some of these anomalies could be explained by existence of a light emission from gammas on extremely long time scales. The understanding of these behaviours is obviously mandatory when projecting a 0νDBD experiment since they can influence the response of the detector to a 0νDBD decay and therefore its efficiency and resolution. The energy resolution, provided that the technique of axis rotation is proven to be reliable also for a 0νDBD event, is $\sim$ 10 keV.

In this chapter it was also described the possibility to identify the interacting particle by the shape of the pulse in the light detector. As I will shaw in Chapter 9 also on the

thermal channel α and β/γ particles have different pulse shape. This feature may allow a better discrimination than the one obtained thanks to the different light yield.

Despite the problems presented above, this crystal is, however, a good candidate for the study of 0νDBD because of the relatively high amount of ^{82}Se in the crystals.

Molybdates

^{100}Mo is one of the most promising 0νDBD isotope because of its large transition energy $Q_{\beta\beta} = 3035$ keV [117] and a considerable natural isotopic abundance (9.67%). Tested crystals containing this isotope were:

- $CaMoO_4$: not the best candidate for 0νDBD of ^{100}Mo because of ^{48}Ca (however it could be depleted). It work fine as bolometer and has a Light Yield of 1.87 keV/MeV. On this crystal, for the first time, was observed the possibility to recognize the interacting particle by the pulse shape of the thermal pulse.
- $ZnMoO_4$: it work fine as bolometer and has a Light Yield of 1.14 keV/MeV. The sample tested has higher internal contaminations respect to other molybdates.
- $MgMoO_4$: very interesting crystal because the high concentration (52% in mass) of molybdenum. The tested crystal wasn't faced to a light detector and moreover had small thermal pulses. Despite this it was possible to discriminate interacting particle by pulse shape.

8.4 Surface contaminations studies

It is now proved that scintillating bolometers are able to recognize the nature of the interacting particles allowing to 'completely' remove the α background in 0νDBD experiments. However, this feature can be used also for diagnostic purposes, e.g. to study surface contaminations of materials faced to the detector. In this section, the first measurements for the study of the CUORE background with scintillating bolometers will be presented.

The current model of the background in the 0νDBD region of bolometers is derived from the Cuoricino experience with TeO_2 crystals (see Chapter 5 and Chapter 7). It assumes that the background in the region above 2615 keV is due mainly to degraded α's from surface contaminations of materials faced to crystals. This model is mainly based on the study of coincident events between TeO_2 bolometers and on the spectral analysis of the structures in the higher energy (alpha) region (see Chapter 5.4). None of the conventional techniques for surface contaminations studies has shown enough sensitivity to study the very low level of contaminations reached. Traditionally the devices used in this field are Si surface barrier detectors. For low counting rates, large area and low background detectors are needed. Today Si surface barriers detectors with an active area

of about 10 cm^2, a typical energy resolution of about 25-30 keV FWHM, and background counting rates of the order 0.05 count/h/cm^2 between 3 and 8 MeV are available [128]. On the contrary, bolometers can easily reach a much larger active area, with a typical energy resolution of 10 keV and a background counting rate in the 3-8 MeV region that can be as low as 0.001 count/h/cm^2. Moreover scintillating bolometers allow a direct identification of the interacting particles and thus dispelling any doubt about the nature of the background. Indeed, if the flat background measured by TeO_2 bolometers in the 3-4 MeV region comes from degraded alphas produced by a contamination in the materials facing the detectors (i.e. the mounting structure) then substituting the TeO_2 crystal with a scintillating bolometer it should be possible to measure the same background and to ascribe it to alpha particles. Such a measurement allows therefore to distinguish between several background scenarios in the 0νDBD region:

- 'all' the events lie in the α band. This will confirm the model according to which the background is due mainly to α surface contaminations
- some of the events lie in the β/γ region. The background could be attributed also to external γ contaminations or (n, γ) reactions
- some of the events lie below the α band in the scatter plot, i.e. in a region where the events are characterized by a very small light output. In this situation, the background must be attributed to neutron interactions or to "dark events" (for example, to random relaxation processes in the materials that constitute the detector, which introduce heat deposits in the crystals, simulating particle interactions)
- the event rate in the energy region of interest is smaller with respect to one observed in measurements done with TeO_2 bolometers. This would mean that the sources of background should be attributed to unknown internal β decay in the TeO_2 crystals
- a mix of the previous situations

In order to reach the ability to identify the nature of the background observed in all the TeO_2 bolometric tests, a very accurate measurement with scintillating bolometers is necessary. Thus some experimental requests on the choice of the absorber must be made.

8.4.1 The choice of the scintillating crystal

Due to their lack of a dead layer and their high energy resolution, bolometers have an extraordinary sensitivity to low range particles like α's. However, a conventional bolometer cannot distinguish the nature of the impinging particle, providing a limited diagnostic power (especially for α particles with energies lower than 2615 keV where the β/γ induced background dominates the detector counting rate).

On the contrary, a scintillating bolometer, thanks to the particle identification technique discussed above, can distinguish an α emission from a β/γ one and finally can reject the β/γ background extending its measurement field to energies by far lower than 3 MeV. However, usually, a scintillating bolometer has to be surrounded by a reflector in order to properly collect the scintillation light therefore it cannot be directly faced to a given sample to study its radioactive emission. However, if a crystal with a very high LY is chosen, it is possible to carry out a measurement without the reflecting sheet. I have therefore proposed to use a BGO crystal ($Bi_4Ge_3O_{12}$), which have a very high light yield and is one of the cheapest and commercially available scintillators that can fulfill these requests.

A run with scintillating bolometers supported by a Cu structure similar to the Tree Tower Test was therefore planned. An array of four $5\times5\times5$ cm^3 BGO crystals was chosen. However, since for this measurements we have to use a light detector, for each crystal only 3 faces could be faced to the mounting structure (see Figure 8.24). The effective surface faced to the copper is then $\sim$300 cm^2.

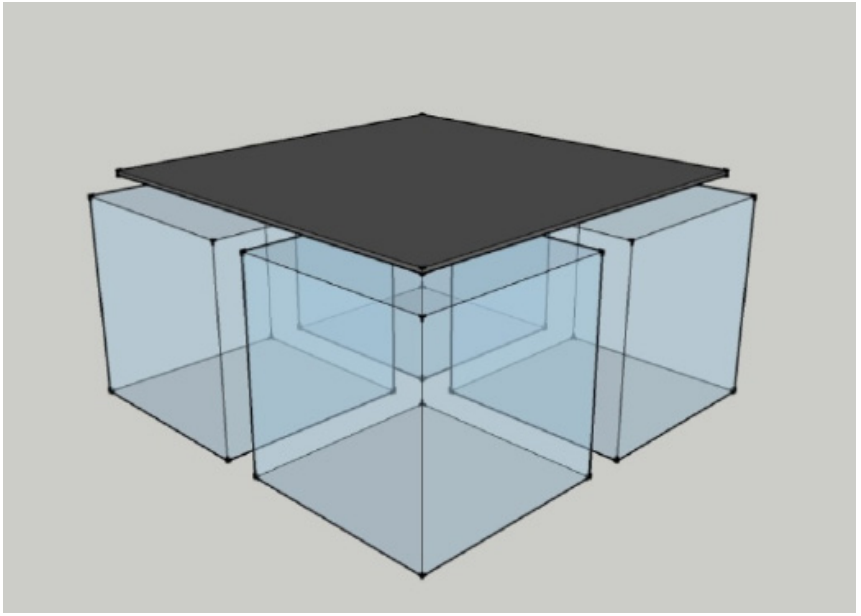

Figure 8.24: Schematic drawing for the arrangement of the four BGO crystals and the Light Detector.

Since crystals are not surrounded by reflecting foil we assume that we will be able to evaluate the surface contamination of the crystals thanks to coincidence studies. Then we can extrapolate the number of counts in anti-coincidence due to surface contaminations of the mounting structures.

In order to evaluate the sensitivity of such a measurement, we have to estimate how long should be a measurement in order to allow a comparison with TeO_2 measurements. It is therefore necessary to fix the background level. In the following we will take as a

reference the Three Tower Test (section 7.2) value because it is the best result obtained with TeO_2 crystals. Then the comparison with any other measurements will simply require a shorter time.

The background observed in the TTT run was 0.055±0.06 counts/keV/kg/y in 3-4 MeV region. Through anti-coincidence analysis it was possible to remove events due to crystals surface contaminations. The background due to only Cu contaminations resulted thus to be 0.041±0.006 counts/keV/kg/y. To compare the TTT results with the BGO measurement it is better refer to the counts per week per detector surface:

$$R_{TTT} = (8.96 \pm 1.31) \cdot 10^{-3} \quad counts/cm^2/week \tag{8.14}$$

The number of expected events for a measurement done with BGO crystals (N^{exp}_{BGO}), supposing a copper surface contamination identical to the TTT one, is reported in Figure 8.25. Here the average number of counts and its 68% C.L. limit, evaluated according to the Feldman-Cousins recipe, are reported as function of the live time. These values are evaluated for three different configurations because, as I will show later, before the start of the actual measurement with the array of four 5x5x5 cm^3 BGO crystals two additional tests were performed. The three different configurations are:

- an array of four 2x2x2 cm^3 BGO crystals
- a single 5x5x5 cm^3 BGO crystal
- an array of four 5x5x5 cm^3 BGO crystals

From Figure 8.25 it is clear that with an array of four 5x5x5 cm^3 BGO crystals within few weeks there will be enough events for a good evaluation of surface contaminations. To compare this expected events N^{exp}_{BGO} with the number of events that will be measured N^{meas}_{BGO}, in Figure 8.26 I report the number of counts with their 68% C.L. limit for measured levels between zero and 0.1 counts/keV/kg/y after 2 weeks (on the left) and after 4 weeks (on the right). Of course, the duration of the measurements will depend on the actual number of counts observed but, presumably, in few weeks we will have enough information to draw conclusions on the background in the α or β region.

8.4.2 The array of 2×2×2 cm^3 BGO crystals

As discussed above, the possibility to do a measurement with an array of 4 BGO crystals (5x5x5 cm^3) is very appealing because it allows to reach enough sensitivity in a reasonably short time (few weeks) and moreover the assembly is similar to a single module (four detectors) of the TTT. However, before arranging this measurement, a test was performed with an array of 4 'small' BGO crystals (2x2x2 cm^3), polished at optical grade, in order to evaluate some technical aspects. The first was to check that the light yield of these

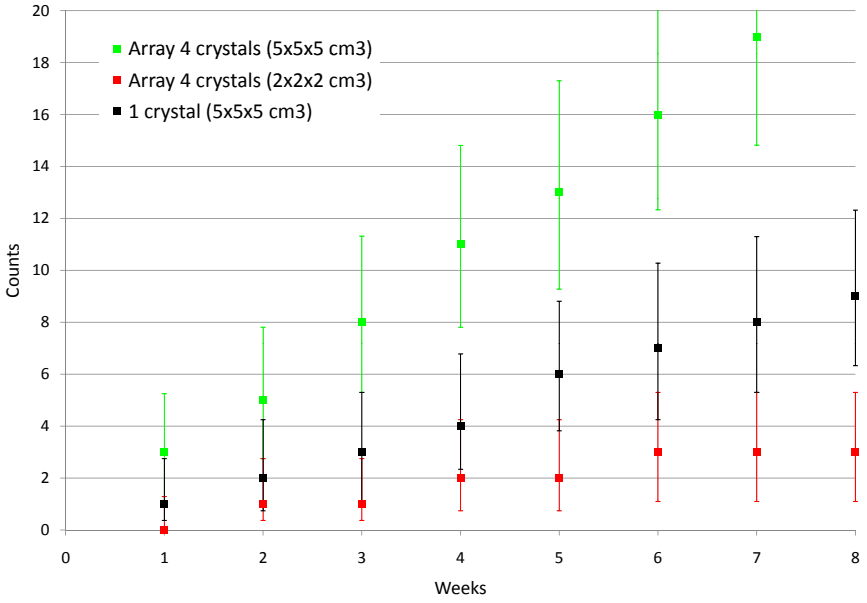

Figure 8.25: Number of expected counts in an energy region of 1 MeV as function of weeks for an array of four 2x2x2 cm^3 BGO crystals (red), a single 5x5x5 cm^3 BGO crystal (black) and an array of four 5x5x5 cm^3 BGO crystals (green).

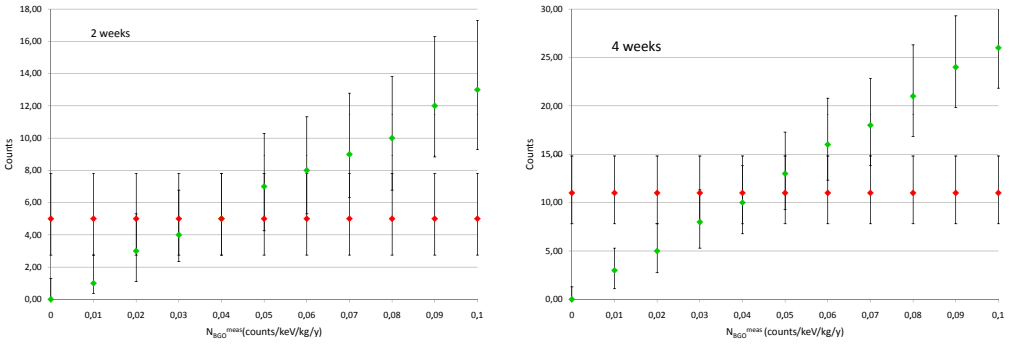

Figure 8.26: Average number of counts and 68% Confidence Level limit for the array of four 5x5x5 cm^3 BGO for 2 weeks (left) and 4 weeks (right) of live time. The number of events expected N_{BGO}^{exp} in the case of a surface contaminations equal to that of the TTT is shown in red while in green the one corresponding to a counting rate less than 0.1 counts/keV/kg/y.

crystals is high enough to have good discrimination even without the reflecting sheet. Another aspect deserving our attention is the internal contaminations of the crystals. As we will see in the following, this preliminary measurement has been very useful also because it allowed to observe an unexpected slow cooling rate for these crystals.

The assembly used for this measurement is reported in Figure 8.27: the four BGO crystals are shown on the left, faced to the light detector (66 mm diameter, 1 mm thick pure Ge) on the right.

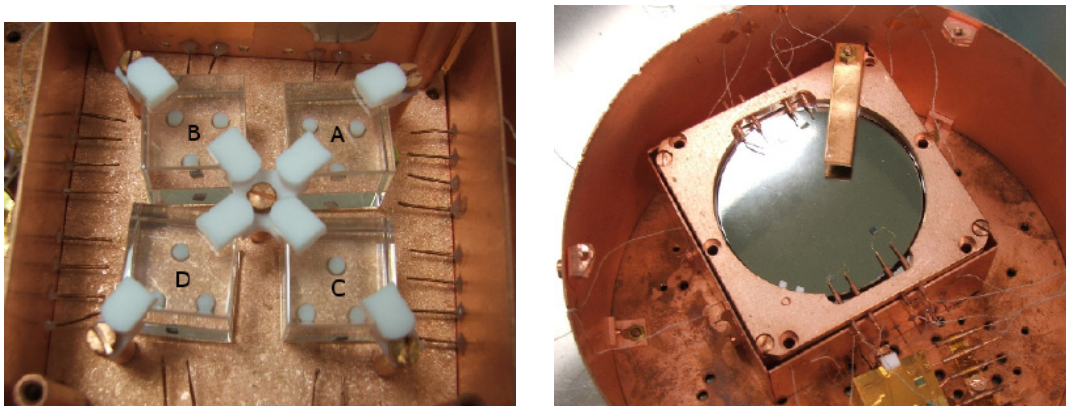

Figure 8.27: Array of four 2x2x2 cm^3 BGO crystals faced to one light detector (66 mm diameter, 1 mm thick pure germanium disk) .

A ^{55}Fe source was used to calibrate the Light Detector while a ^{147}Sm and a ^{224}Ra α-sources (source B) were faced to crystals 'A' and 'B' (see Figure 8.27). The ^{147}Sm source was used because of the very low Q value of its α decay (Q=2233 keV) which allows a direct comparison of the detector response (heat and/or light) to alpha's and gamma's.

BGO cooling

During the cooling down of the cryostat it was observed that the BGO crystals cooling was very slow (Figure 8.28). Just to give an idea, crystals of the same size usually reach temperatures of ∼15 mK in few days (∼ 2-3 days). A possible explanation of such a strange behaviour could be addressed to cryostat problems or to bad thermal link between the detector assembly and the Mixing Chamber. However, other crystals hosted in the same bolometric setup haven't shown this behaviour. A possible explanation for such a behavior is an excess of the heat capacity (see Section 4.2). Such a residual contribution would lead to the observed slow heat releases.

The slow cooling of the crystals raised a lot of worries when extrapolated to the 5×5×5 cm^3 BGO absorbers, since their thermal capacitance is even bigger than the one of the 2×2×2 cm^3 BGO crystals. For this reason, before achieve a measurement with an array of 5×5×5 cm^3 BGO crystals, a measurement with only one 5x5x5 cm^3 crystal was performed. This turns out to be a no-cost measurements because it was hosted in a run planned to test other crystals.

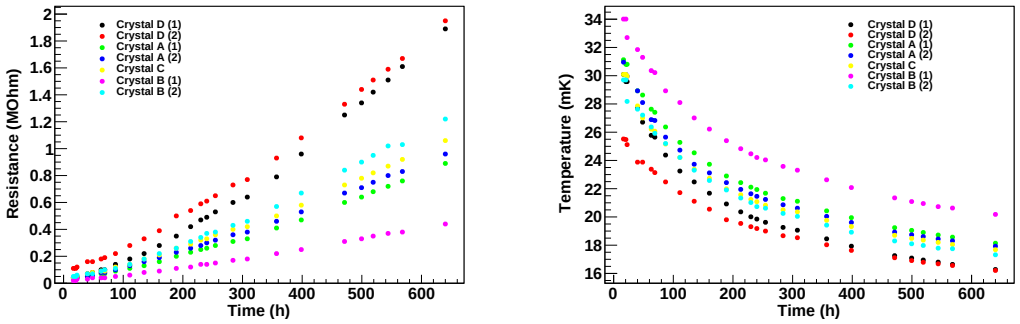

Figure 8.28: Resistances and temperatures of the detectors. On each crystal we glued two thermistors (1 and 2 in the plots); the electrical connections of crystal C broke during the cooling, thus only one thermistor is reported. The different temperatures measured by two thermistors on the same crystal can be explained by small differences of T_0 and ρ_0 values. However, most important is the trend of the curves than temperature absolute values.

Analysis and Results of the 2×2×2 cm^3 array

The crystals did not cool as expected and their high temperature spoiled the quality of the measurement on the thermal channel. Nevertheless, the results were more than satisfactory with regard to the discrimination power even without the reflecting sheet.

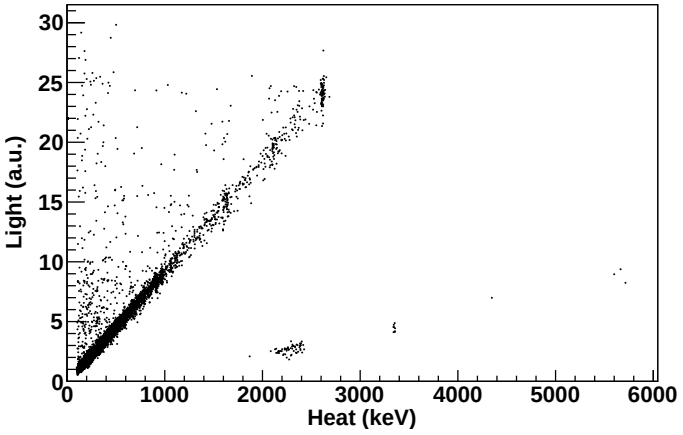

Figure 8.29: Light vs heat scatter plot for a calibration measurement performed with a ^{232}Th γ source. The heat channel is calibrated on γ events.

In Figure 8.29 it is reported the scatter plot of light vs. heat obtained with the crystal 'A' faced to the ^{147}Sm source. It is clear from figure that the discrimination power is much more than enough to recognize α particles. The β/γ LY for this crystal is 18.8 keV/MeV at 2615 keV γ-line.

In the α region (bottom band) it is possible to observe two peaks in the 2-4 MeV energy region (calibration performed on β/γ events). The peak at lower energy, visible only on crystal 'A' and 'B', is due to the α decay of ^{147}Sm. As mentioned above this source was faced to the crystals in order to allow an overlap of the energy regions with alpha and gamma lines (which are usually well separated). For this reason we tried to produce a very shallow source in order to have a sharp peak to being able to accurately assess the position of the peak. To fulfill this difficult task the ^{147}Sm source was deposited through electrodeposition. Since this was our first experience with such a kind of source the deposition is not so good and the peak has a very long tail (see Figure 8.30). It is evident the difference between this peak and the α peak at $\sim$3.4 MeV due to internal contaminations. It is then clear that it was very difficult to calibrate with the ^{147}Sm peak.

The other peak at higher energy is due to ^{209}Bi (Q=3137 keV). This is a very interesting rare α decay and for this reason it will be described in detail in the following. Using this peak it was possible to evaluate the QF_α which is

$$QF_\alpha(^{209}Bi) = 0.14 \pm 0.02 \tag{8.15}$$

This Q.F. together with the very small width of the α and β bands allowed to obtain a discrimination confidence level of D_{light}=10.5 σ.

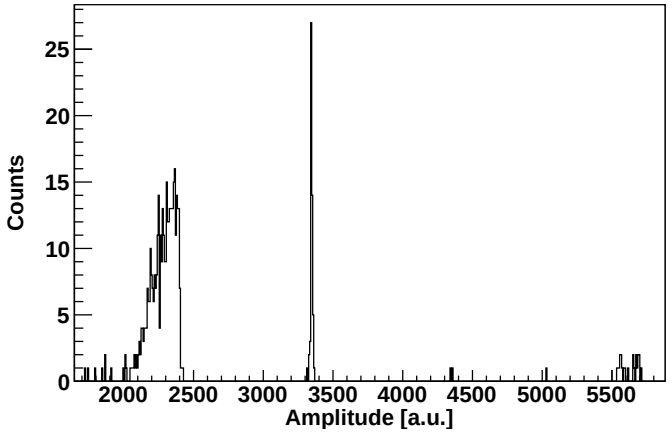

Figure 8.30: Spectrum of the α region. It is possible to observe the broaded α peak due to ^{147}Sm source and the sharp ^{209}Bi peak.

The β/γ spectrum

The β/γ region of a background measurement is reported in Figure 8.31. Some peaks are clearly visible. These peaks have been attributed to a ^{207}Bi contamination of the crystals. ^{207}Bi is produced by charged particle reaction and has a half-life of 31.55 years. A possible

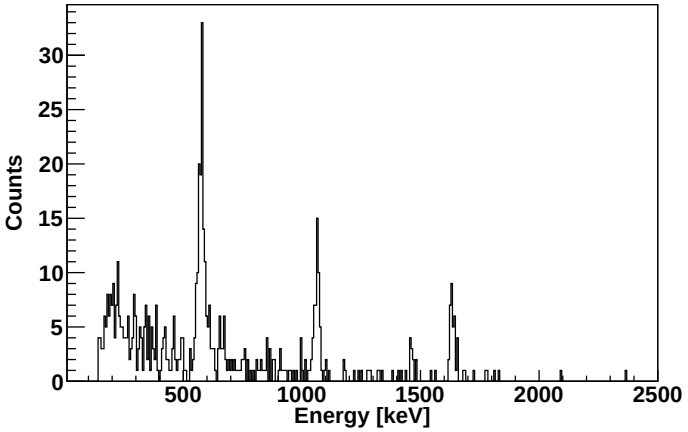

Figure 8.31: Calibrated β/γ spectrum for BGO crystals: background measurement.

explanation for its presence in the crystals is that ^{207}Bi was originated by the interaction of the cosmic ray protons (^{206}Pb+p$\rightarrow$ ^{207}Bi) [123]. This crystals are indeed produced at SICCAS, in China, and arrived at LNGS by plane.

^{207}Bi decays via electron-capture and emits mainly γ-rays of 570 keV (97.74%), 1064 keV (74.5%) and 1770 keV (6.9 %) (see decay scheme in Figure 8.32).

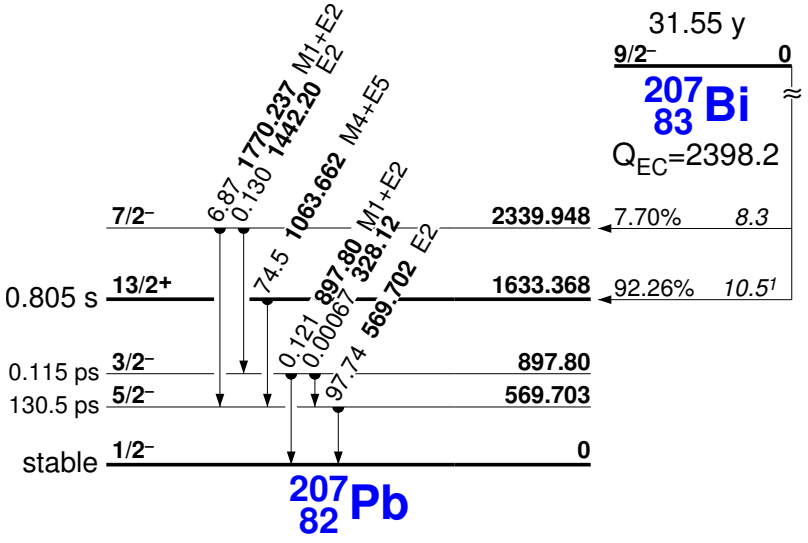

Figure 8.32: Decay scheme of ^{207}Bi.

In the electron capture process, in addition to the γ-rays emission due to the de-excitation of the daughter nucleus there is also the X-ray emission associated to the rearrangement of the electronic shell. For this reason, in the case of an internal contaminations of the bolometers, a peak at the sum energy of gamma's and the X-rays is observed. How-

ever, the ^{207}Bi decay is a very peculiar one. The half life of the 1633 keV level is 'very long' (0.8 s) and thus the γ emitted by this level do not add up to X-rays. Instead, the level at 2340 keV decays instantly and therefore, in this case, the binding energy of the captured electron (K, L, M, ...) must be added to that of the emitted gamma. However, the K-capture from this level was not observed [124]. The electron capture then happens practically only on L shell and an X-ray energy of ∼10 keV must be added to the 1770 keV gamma line. In summary therefore, with regard to internal contamination in ^{207}Bi, the most intense peaks observed have energies of 570 keV, 1064 keV, ∼1770+10 keV, 570+1064 keV and ∼570+1770+10 keV. Taking into account these peculiarities of the ^{207}Bi decay was possible to calibrate the β/γ spectrum and explain all the peaks in the spectrum.

A large internal contamination in ^{207}Bi could constitute a serious technical problem for large mass bolometers because of the pile-up. This could greatly reduce the detection efficiency and moreover produce an unwanted background in the β/γ region above the γ line of ^{208}Tl (2615 keV). This issue should be taken into particular attention especially with larger crystals. Thus I have done a GEANT4 simulation in order to ensure that the background counting rate will not grow up to a dangerous level by using the 5×5×5 cm^3 BGO crystals.

Scaling the ^{207}Bi contamination for 2×2×2 cm^3 crystals to the 5×5×5 cm^3 crystals and evaluating the change in the detection efficiency through simulations (see Figure 8.33) it was possible to evaluate the rate expected for big crystals. It should be ∼50 mHz. This value is acceptable for bolometric measurements but, however, it must be kept in mind that this evaluation depends heavily on ^{207}Bi contamination in the 5×5×5 cm^3 crystals. Then, also for this reason, it was useful to do a measurement with one 5×5×5 cm^3 BGO crystal.

^{209}Bi Rare Decay

As mentioned above the ∼3.4 MeV α peak (calibration performed on β/γ region) was attributed to ^{209}Bi. This isotope was supposed to be the heaviest stable isotope in nature, since its decay had never been observed. Nevertheless, some theoretical calculations [125] showed that ^{209}Bi is metastable with respect to α-decay, according to the schema depicted in Figure 8.34.

The detection of this decay with "standard" techniques is extremely difficult because the energy of the emitted α particles is very low (3.137 MeV). Indeed, no positive results were reported. In 2003, the possibility of performing this kind of measurement by means of BGO scintillating bolometers was demonstrated [126]. Thanks to that measurement, an energy release of 3137±1(statistical)±2(systematic) keV, an a half life of $T_{1/2}^{meas}(^{209}Bi)$ = (1.9 ± 0.2)×10^{19} years were measured. Following this idea, the collected data was used to study the rare decay of this isotope.

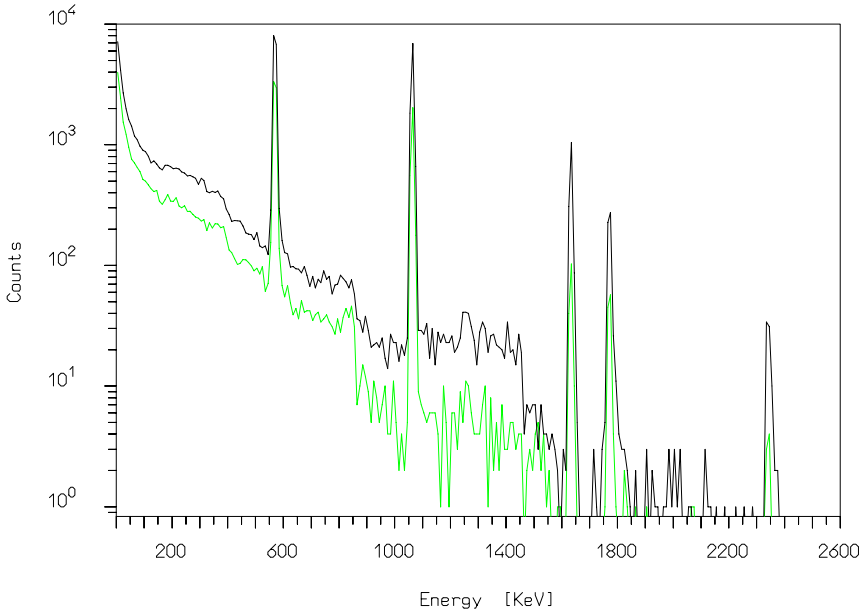

Figure 8.33: Simulation of the background counting rate due to ^{207}Bi in a 2×2×2 cm^3 BGO crystal (black line) and a 5×5×5 cm^3 crystal (green line).

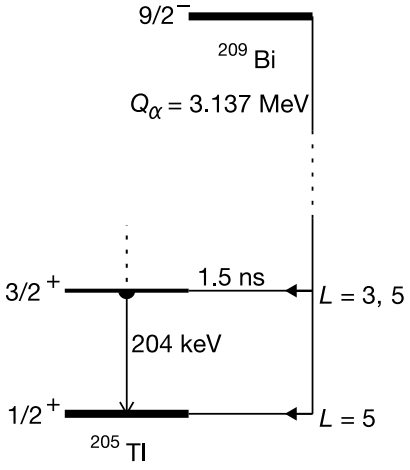

Figure 8.34: Decay scheme of ^{209}Bi.

The ^{209}Bi peak (see Figure 8.30) was fitted by means of a single Gaussian function and the obtained FWHM was 19 ± 2 keV. The total statistic obtained with 2×2×2 cm^3 BGO crystals was 2.14×10^{22} atoms×year and the half life:

$$T_{1/2}(^{209}Bi) = (1.99 \pm 0.03) \times 10^{19}\ years \tag{8.16}$$

This result is compatible with the previous measurement but with much more higher precision.

8.4.3 The 5×5×5 cm^3 crystal

The excellent discrimination level obtained with small BGO samples convinced to continue our program with these crystals. In order to investigate the problem of the slow cooling down for big (5x5x5 cm^3) BGO crystals and measure the rate due to ^{207}Bi. For this reason a measurements of a single 5x5x5 cm^3 BGO crystal was performed. It was decided to surround the crystal with a reflecting sheet because the goal of this measurement wasn't the study of surface contaminations. In such a way it could be possible to evaluate the collection efficiency due to the reflecting sheet comparing this measurement with future ones without reflecting sheets.

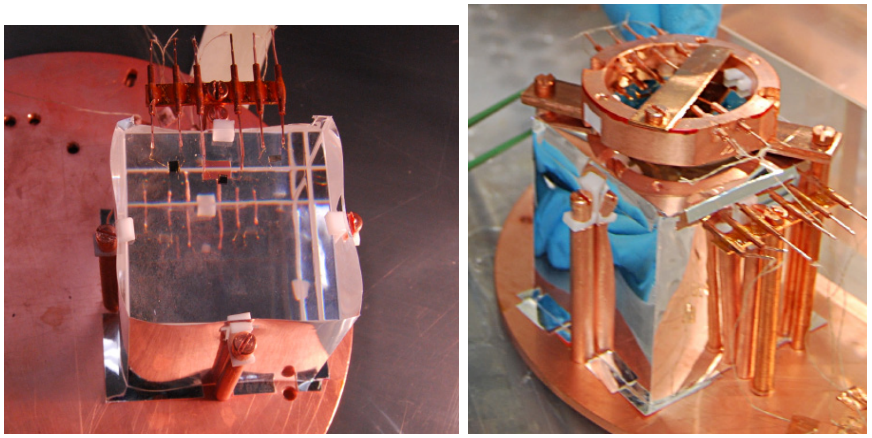

Figure 8.35: On the left the 5×5×5 cm^3 BGO crystal (optical surfaces) surrounded by the reflecting sheet while on the right the 5×5×5 cm^3 BGO crystal with the light detector

In Figure 8.35 it is possible to observe the assembly for this crystal. The scintillation light produced by the crystal was detected by a 36 mm diameter, 0.3 mm thick pure germanium disk.

As expected also this crystal cooled down very slowly. It is important however to note that also other crystals in the same assembly showed a long cooling down. This could then partially be explained by a reduction of the cooling power of the cryostat due to losses of ^{3}He/^{4}He mixture (working principles of cryostat in Appendix). For this reason, ∼1 month after the start of the cooling down procedure a small amount of ^{3}He/^{4}He mixture was added. At the same time, also some changes to the acquisition channel of BGO crystal were also done (changed the load resistances and increased the voltage bias supply in order to have a higher bias current which increased the signal amplitude). After these changes the quality of measurements improved considerably.

The scatter plot obtained in ∼540 hours of measurements is reported Figure 8.36. In red are reported α events. The same data are reported in the heat channel spectrum of Figure 8.37. The α peak of ^{209}Bi and the β/γ events of the internal contamination in

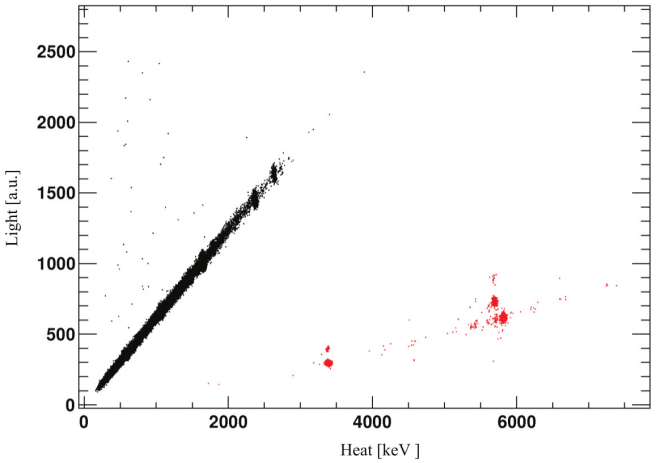

Figure 8.36: Scatter plot heat vs light of a 5×5×5 cm^3 BGO crystal for a ∼540 hours background measurement.

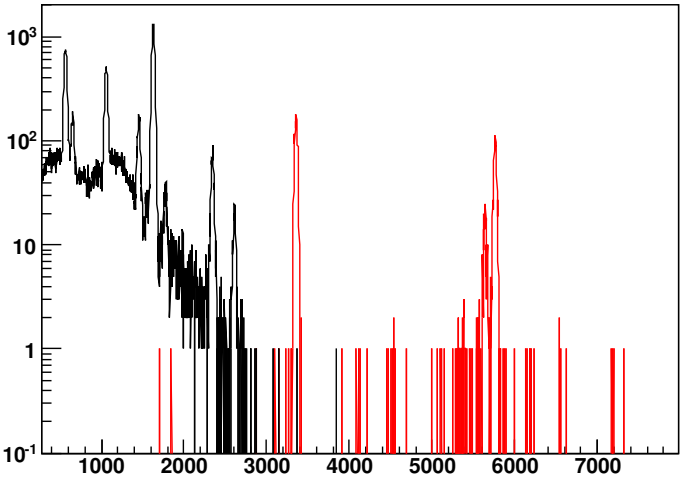

Figure 8.37: Spectrum acquired with 5×5×5 cm^3 BGO crystal. In red α events selected in the light vs heat scatter plot.

^{207}Bi can be easily recognized. In addition, can be seen the α + nucleus recoil peak at 5.4 MeV of ^{210}Pb and the 5.3 MeV α peak due surface contaminations of this isotope. It must be highlighted that, except for the contaminations in ^{207}Bi, the crystal is very clean from a radioactive point of view.

The rate of counts between 200 keV and 3 MeV is ∼70 mHz.

The obtained FWHM for the peaks in the heat channel is not excellent: 34.5 ± 0.7 keV on the ^{209}Bi peak. This can be explained by the high temperature of the crystal (signals were very small (≈ 1 μV/MeV)). Keeping in mind the precautions described above better results will be obtained by a further cooling of these crystals.

Peak	Energy [keV]	L.Y. [keV/MeV]
^{207}Bi	570	16.67 ± 0.04
^{207}Bi	1064	16.51 ± 0.04
^{207}Bi	1634	16.22 ± 0.02
^{209}Bi	3137	2.53 ± 0.02

Table 8.5: LY for γ and α events due to ^{207}Bi and ^{209}Bi.

Thanks to the high Light Yield it is possible to observe α and γ peaks also on the LD spectrum (Figure 8.38). The LY for ^{207}Bi γ lines and for the ^{209}Bi α line are reported in Table 8.5. The Q.F. for the ^{209}Bi is:

$$Q.F.(^{209}Bi) = 0.16 \pm 0.01 \tag{8.17}$$

The ^{209}Bi decay

The data obtained during the ∼540 hours measurement can be also used to evaluate the ^{209}Bi half-life. But first, a consideration is needed. Another interesting feature can in fact be observed in the scatter plot reported in Figure 8.36. Above the 'big' ^{209}Bi spot there is another, smaller, spot at the same energy on the heat channel but with higher light. An estimate of the distance between the two spots could be obtained by means of a rough calibration of the light detector with the γ peaks (Figure 8.38). The distance between the two spots turns out to be equal to the light produced by the release of ∼200 keV by a γ particle in the BGO crystal. Then a possible explanation of the 'small' spot could be given by the ^{209}Bi decay leaving the ^{205}Tl on an excited state with an instantaneous de-excitation with the emission of a 204 keV γ ray. Since the efficiency of containment of this γ is ∼1, these events will still be at the Q value of the transition on the heat axis. On the contrary, on the light channel, because of the greater LY for γ than for α, these events will emit more scintillation light than those decaying directly to the ground state. The ratio between the number of events in the two spot is ∼1.2%. More detailed check on these events are being carried out.

In Figure 8.39 the projection of ^{209}Bi events on the heat axis is reported. The statistics collected in this measurement is 1.07×10^{23} atoms×year, ∼30 times higher than [126]. The high statistics would therefore give a good result on the life of ^{209}Bi. However, due to the

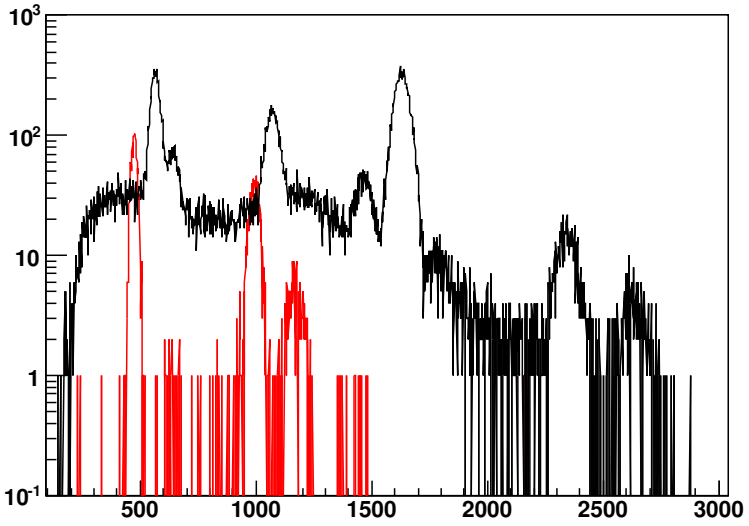

Figure 8.38: Spectrum acquired by the light detector faced to 5×5×5 cm^3 BGO crystal. In red, the α events selected in the light vs heat scatter plot.

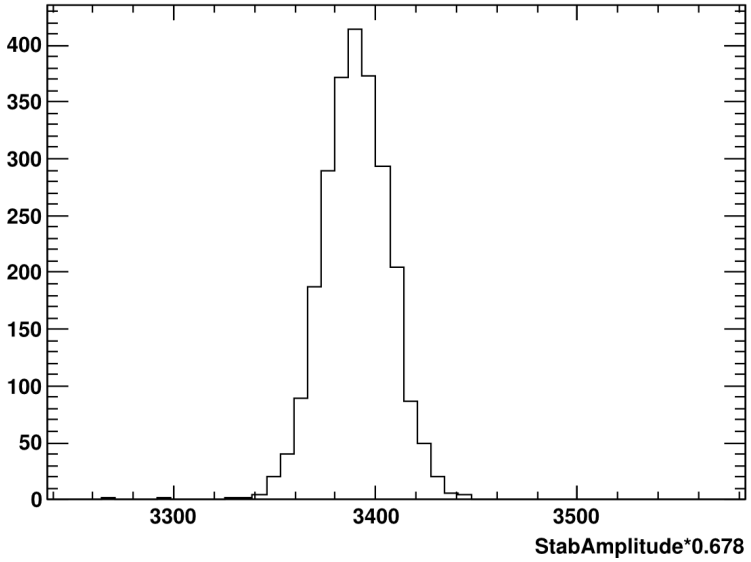

Figure 8.39: ^{209}Bi α peak in the 5×5×5 cm^3 BGO measurements. Calibration performed on γ events.

high rate measured, an evaluation of the detector efficiency better at than few percent is very difficult. We are therefore working on the data analysis to further improve the already excellent results obtained with the array of 2×2×2 cm^3 BGO crystals.

Study of surface contaminations

Although the purpose of this measurement was not the study of surface contamination is still very interesting to report the obtained values. Table 8.6 shows the values measured in the beta region (for E>3 MeV) and in the alpha band in the 2-3 MeV region and in the 3.5-4 MeV region (calibration performed on γ region). The α band was divided in two regions because of the ^{209}Bi peak.

Band	Energy Region [MeV]	Background [counts/keV/kg/y]
β	3.0 - 4.0	0.07±0.04
α	2.0 - 3.0	<0.043
α	3.5 - 4.0	0.181±0.08

Table 8.6: Background obtained with the 5×5×5 cm^3 BGO crystal in three different region. The limit in the α region between 2-3 MeV is evaluated with Feldman-Cousins at 90% C.L..

In this measurement the anti-coincidence method can not be used and these values are due to surface contamination both of the crystal and of materials facing it. It could be also interesting to note that no care was made to clean surfaces. They were simply wiped with alcohol. Taking into account these aspects it is quite surprising to note the good levels of background reached especially in the 2-3 MeV α region. Looking at these results the measurement with the array of 4 BGO (5×5×5 cm^3) crystals is even more interesting.

Chapter 9

Pulse Shape Analysis in bolometer

In Chapter 8 it was shown how, thanks to the double read-out of light and heat, in scintillating bolometers it is possible to discriminate α particles from β/γ. In this Chapter I will report on the possibility to obtain similar results just by Pulse Shape Analysis (PSA), without the requirement of a double readout. Indeed, during the R&D work described in the previous Chapter and centered on the development of scintillating bolometers for 0νDBD , I discovered that some of the scintillating crystals had a thermal signal showing clear differences depending on the interacting particles. Namely the pulse shape parameters used to characterize the thermal signal had different distributions for alphas and beta-gammas.

9.1 PSA advantages

The discovery of a different pulse shape of the thermal signals produced by α's and by β/γ's opens the possibility of realizing a 'zero background' bolometric experiment without the need of a light detector coupled to each bolometer. In the case of construction of a huge, multi-detector array, such as CUORE [40] and EURECA [127], the benefits of employing this technique would be impressive:

- more ease during assembly because the single element of the array would be a quite simpler device.
- fewer readout channels, with not only an evident reduction of cost and work, but also a cryogenic benefit. In a cryogenic experiment particular care should be devoted to reduce any thermal link between room temperature and the bolometers, that work at few mK. Among the other possible heat loads, the one due to readout wires must be taken into account and its reduction is always a good solution.

- a significant cost reduction, saving money and work that would be necessary for the light detectors procurement and optimization.
- no need of light collectors, this would simplify the structure of the assembly and - avoiding the interposition of materials between the crystals - would allow to fully exploit the anticoincidence technique for background reduction.

As a final remark, it is worth to note that these devices could be also used for the measurements of α emissions from surfaces, when extremely low counting rate are needed. As already described in Chapter 8.4, bolometers can reach sensitivity on surface contaminations order of magnitude higher than traditional devices. However, to study surface contaminations the reflecting sheet must obviously be removed. To ensure a sufficient collection of light even in these condition only scintillating crystals with very high LY can be employed (like the BGO). A viable alternative is always the use of crystals able to discriminate particles through thermal pulse shape.

9.2 Pulse shape signature in the heat pulse

The results here reported refer to measurements in which different scintillating bolometers, each coupled to a light detector (but in one case), were exposed to γ and α sources. This allowed to study the response of devices to different radiations. The light signal was used to identify, on the basis of the heat to light ratio, the particle producing the event under study.

As mentioned in section 4.7, in bolometric measurements, for each triggered signal different pulse shape parameters are computed by the off-line analysis, generally to be used to recognize and reject spurious and pile-up events. In the case of scintillating bolometers, looking at the distribution of the pulse shape parameters for the heat signals, I realized that it was possible to distinguish β/γ from α events. This is clearly evident in Fig. 9.1 where the scatter plot of the amplitudes measured for the light and heat signals is compared with the scatter plot (obtained for the same events) of the linearized rise-time (see later in the text) vs. amplitude for the heat signal (τ^{lin}_{rise} vs. heat). In this detector, α and β/γ interactions draw different distributions in both the scatter plots, definitely proving that the shape of the thermal pulse induced by an α particle is different from that of a β/γ interaction.

This behavior could be explained by the dependence of the light yield on the nature of the interacting particle. Indeed, the high ionization density of α particles implies that all the scintillation states along their path are occupied. This saturation effect does not occur - or at least is much less - for β/γ particles. Therefore, in α interactions a larger fraction of energy flows in the heat channel with respect to β/γ events. This leads not only to a different light and heat yield but also to a different time evolution of both signals. The

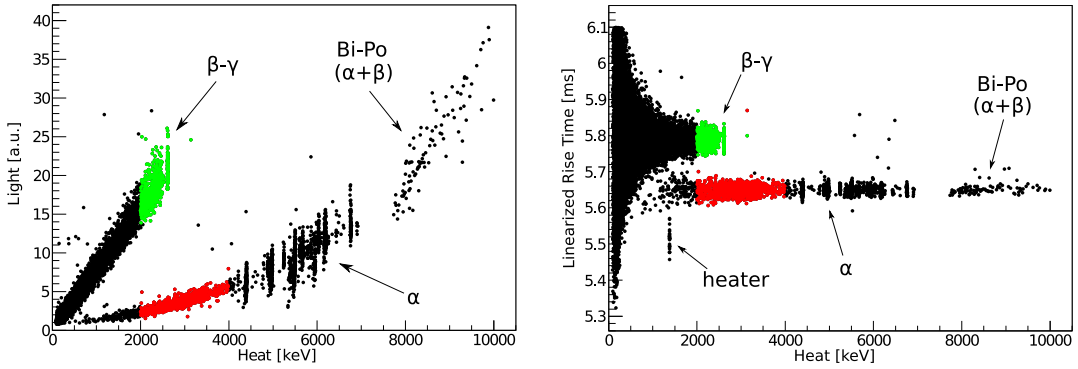

Figure 9.1: Scatter plot obtained with a $CaMoO_4$ crystal. Left panel: scatter plot of light vs. heat. The energy calibration is performed on the γ peaks. In red events in the 2-4 MeV region due to α particles while in green events due to β/γ in the same region. Right panel: scatter plot of τ_{rise}^{lin} vs. heat obtained for the same events. In green events in the 2-4 MeV regions due to β/γ particles and in red α events.

pulse shape of the thermal signal then could be explained by the partition of energy in the two channels with different decay constants (more details on this will be given in section 9.7). In particular, as shown by [129, 130] the scintillation produced in molibdates by α and β/γ particles presents few decay time constants with different relative intensities. Also a strong temperature dependence of the averaged decay time of the light pulses in these same crystals was reported [131, 132]. For this reason, while at room temperature the averaged decay time of molybdate scintillators is of the order of tens of μs (thus almost instantaneous in the heat pulse timescale), at low temperatures it increases to hundreds of μs and is therefore comparable to the typical rise-time of the heat signal of scintillating bolometers.

In the following sections I analyze the results obtained with different crystals, each being a possible candidate for a 0νDBD experiment. For each crystal I will quote the discrimination power achieved in the 0νDBD region between α and β/γ particles on the basis of the light/heat ratio or simply on the basis of the pulse shape of the heat signal, proving how similar they are. I will discuss in more detail the case of $CaMoO_4$, briefly summarizing the results obtained for other crystals.

9.3 $CaMoO_4$

As described in Chapter 8.3.3, $CaMoO_4$ is a very interesting compound for the study of 0νDBD. In that chapter it was observed that the discrimination power D_{Light} (see equation

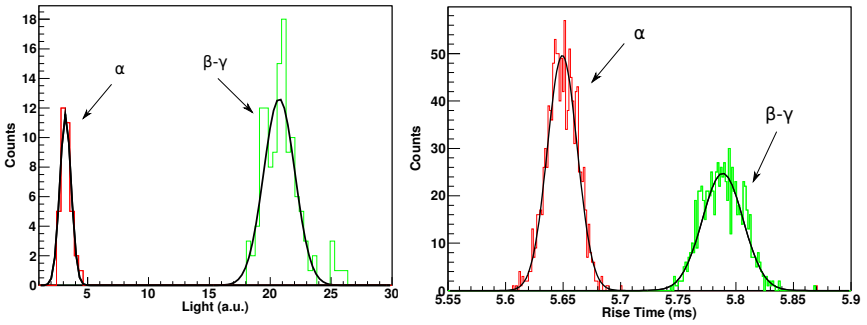

Figure 9.2: β/γ and α discrimination power in $CaMoO_4$. Left panel: projection on the Light axis of the ^{208}Tl γ-line (2615 keV) (in green) and of α events (in red) that released a similar energy in the $CaMoO_4$ crystal. The separation corresponds to 12.6 σ. Right panel: projection on the τ^{lin}_{rise} axis of events in the 2-4 MeV regions due to β/γ events (in green) and α events (in red). The separation here corresponds to 6.5 σ. These same events are reported, with identical colors, in Fig. 9.1

8.1) due to the different light yield of alphas and beta/gamma particles is 12.6 σ (Fig. 9.2 left). Even if in a little bit less efficient way, also the analysis of the shape of the thermal signal can distinguish between the interacting particles. This is shown in the right panel of Figure 9.1 where the distribution of the thermal pulse τ^{lin}_{rise} is shown as a function of heat for the same events shown in the left panel. Two separate bands, ascribed to β/γ and α events can be identified. The former with an average rise-time of ∼5.8 ms, the latter with ∼5.6 ms. In this plot the weak energy dependence of τ_{rise} observed for the two populations was corrected by fitting their rise-time distributions with two lines having the same slope. To do this the β/γ events in the 0.5-2.6 MeV range and α events in the 1.5-7 MeV range were used. The τ_{rise} is then linearized re-defining it as $\tau^{lin}_{rise} = \tau_{rise} - slope \times E$ with $slope$=0.0075 ms/MeV.

In order to emphasize the correspondence in the identification of β/γ and α events, signals selected in the light vs. heat scatter plot as having an energy between 2 and 4 MeV and belonging to the β/γ or α bands, are reported in different colors. I will refer in the following to these two groups of events as to 2-4 MeV γ's and 2-4 MeV α's, although above the 2615 keV line the γ group results empty. These two samples will be used to evaluate the difference in shape among β/γ and α signals.

In Fig. 9.3 two pulses obtained by averaging separately over the two groups of signals are compared. The average is needed to get rid of the noise that can otherwise shadow the small differences among the pulses. The difference in shape can be appreciated in the bottom panel of Fig. 9.3

The discrimination power $D_{RiseTime}$ can be defined exactly as done for D_{Light} (eq. 8.1):

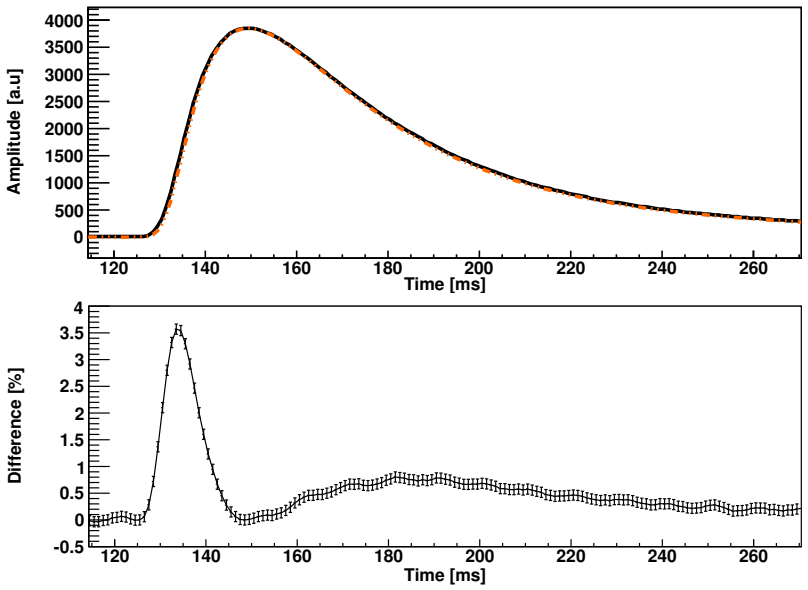

Figure 9.3: $CaMoO_4$ crystal, comparison of β/γ's and α's pulse shape. Top panel: thermal pulse obtained by averaging signals belonging to the 2615 keV γ-line (black continuous line) and signals due to α particles that release a similar energy (red dotted line). Bottom panel: difference, in percent of the maximum amplitude, between the two averaged pulses.

$$D_{RiseTime}(E) = \frac{RiseTime_{\beta/\gamma} - RiseTime_{\alpha}}{\sqrt{\sigma^2_{\beta/\gamma} + \sigma^2_{\alpha}}} \tag{9.1}$$

where, however, the dependence on energy is due only to the variation of the width of the rise-time distributions since the difference in rise time appears to be independent on energy. The rise time distribution of 2-4 MeV γ and 2-4 MeV α events is shown in Fig. 9.2 (right panel). A gaussian fit of the two peaks yields a rise-time of (5.788±0.017) ms for γ's and of (5.649±0.013) ms for α's. $D_{RiseTime}$ is therefore 6.5 σ. As done for D_{Light} it was possible extrapolate the $D_{RiseTime}$ value even in the energy region where the α band is poorly populated, simply assuming that the distance between the two bands remains constant (as observed) and the only change in $D_{RiseTime}$ is due to the larger width of the two distributions, at low energies, because of the noise. The result is that $D_{RiseTime}$ becomes lower than 2 σ at 500 keV and the ∼150 μs difference in rise time of α and β/γ events cannot be appreciated when the pulse amplitude is too low.

The discrimination of α events was observed also in other shape parameters such as the decay-time and the TVR. The possibility to increase the discrimination power by combining the information from different shape parameters or the fit on the rise-time is under study.

Either in the light vs. heat scatter plot as in the τ^{lin}_{rise} vs. heat one there are some

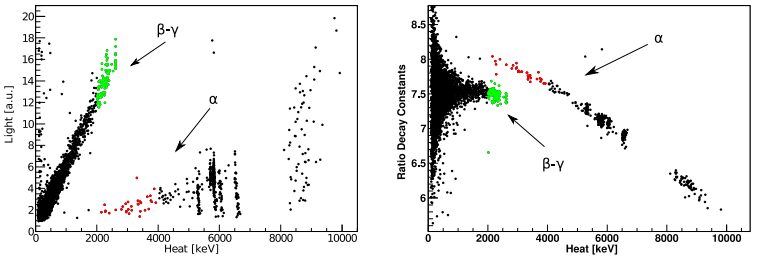

Figure 9.4: $ZnMoO_4$ crystal. Scatter plot of light vs. heat (left panel) and scatter plot of RDC vs. heat (right panel). In green events in the 2-4 MeV regions due to β/γ particles and in red those due to α's.

outliers that could be an indication of a failure of the one or the other particle identification technique. However the events that in the two plots lie outside the main distributions can be accounted for if one considers the following two effects. If a γ-ray interacts both in the light detector and in the scintillator the corresponding light signal has a wrong amplitude since it is not only ascribed to scintillating photons but also by a direct γ interaction in the Ge wafer. Furthermore, the measurement is performed in a high rate condition, therefore a number of pile-up events in each of the two detectors are expected. This leads to an erroneous evaluation of the pulse amplitude and pulse rise time.

9.4 $ZnMoO_4$

As described in section 8.3.3 a 19.8 g $ZnMoO_4$ crystal was tested. Unlike for the $CaMoO_4$ case where the most efficient parameter for the discrimination is the rise-time, this measurement showed a higher discrimination power on the decay-time of the thermal pulse. In order to emphasize the discrimination power, all signals has been fit with a function obtained as the sum of two exponentials:

$$\Delta V(t) = (e^{-t/\tau_1 + A_1} + e^{-t/\tau_2 + A_2}) \tag{9.2}$$

where the τ_1 and τ_2 parameters are obtained by fitting the decay of the raw thermal signals. It was observed that the best discrimination power is obtained by the ratio of the two decay constants (RDC):

$$RDC = \frac{\tau_1}{\tau_2} \tag{9.3}$$

The scatter plot of RDC vs. heat is reported in the right panel of Fig. 9.4 (in the left panel the light vs. heat scatter plot is shown). The discrimination between α and β/γ populations provided by RDC is evaluated linearizing the RDC vs. heat relationship

(fitting the α band in the scatter plot of Fig. 9.4 with a polynomial as done for the τ_{rise} of $CaMoO_4$) and then projecting the distribution of RDC^{lin} for events in the 2-4 MeV range (Figure 9.5). The two peaks (β/γ and α) are then fitted with a gaussian. The discrimination power D_{RDC} is 5.4 σ.

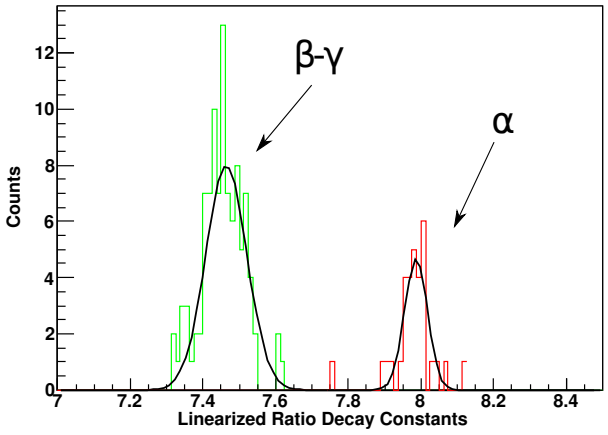

Figure 9.5: β/γ and α discrimination power in $ZnMoO_4$. Projection on the RDC^{lin} axis (after linearization of the scatter plot of Fig. 9.4, right panel) of events in the 2-4 MeV regions due to β/γ events (in green) and α events (in red).

9.5 $MgMoO_4$

Despite the problem with this crystal described in section 8.3.3, it was possible to observe in the scatter plot RDC vs. heat (fig. 9.6) a difference between events due to the interaction of α particles and events due to β/γ events.

The discrimination between the two populations provided by the RDC parameter can be evaluated with a gaussian fit of the two peaks obtained by projecting selected events after linearization. The discrimination power D_{RDC} is 1.8 σ. This discrimination is not as good as for the previous detectors but it is important to remember that this crystal had a very small signal because of problems with the thermistor gluing. A new and more detailed measurements to better study this promising crystal is therefore urged.

9.6 ZnSe

Also for this crystal I will report here the discrimination power on the RDC of the heat channel obtained with the Huge ZnSe crystal (h = 50mm, $\varnothing$ = 40mm, 337g). Characteristics of measurements are reported in detail in section 8.3.2.

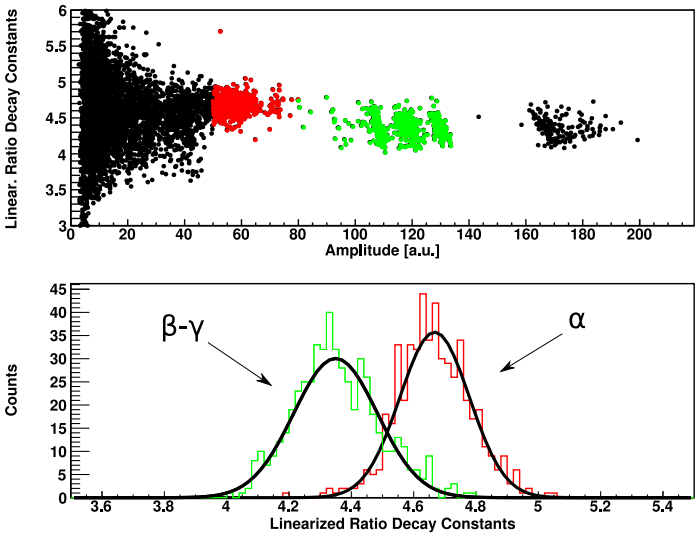

Figure 9.6: $MgMoO_4$ crystal: scatter plot of RDC^{lin} vs. Heat (top panel) and projection of 2-4 MeV events on the RDC^{lin} axis (bottom panel). In green events in the 2-4 MeV regions due to β/γ particles and in red those due to α's.

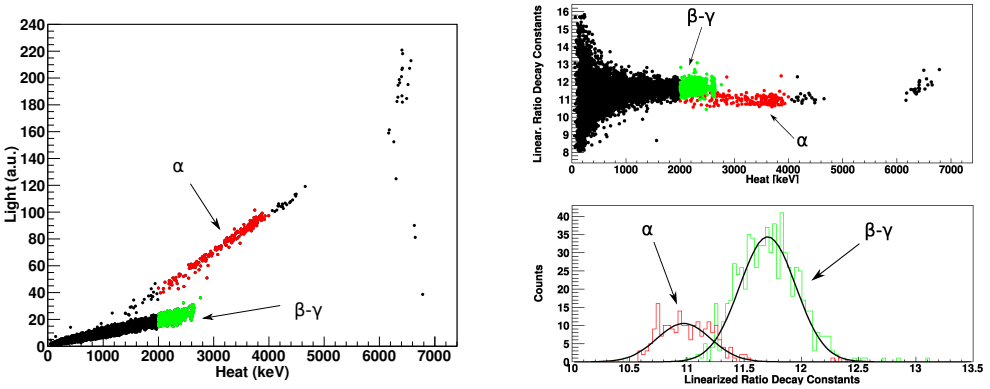

Figure 9.7: On the left: scatter plot of light vs. heat obtained with a ZnSe crystal. In green events in the 2-4 MeV regions due to β/γ particles and in red those due to α's. On the right: the scatter plot of RDC vs. heat (top panel) and projection of 2-4 MeV events on the RDC axis (bottom panel). In color the events selected in the light vs. heat scatter plot.

In Fig. 9.7, on the left, the light vs. heat scatter plot of a measurements of ∼70 h of live time is shown. In red are reported events due to α particles, in green β/γ events. The same events are reported in the scatter plot RDC^{lin} vs. heat on the right. Also in this

case it is possible to observe a difference between the events due to the interaction of α and β/γ particles. The discrimination power evaluated on the parameter (D_{RDC}) is 2.2 σ.

Again discrimination is not very good. On the other hand, it should be stressed that the discrimination of interacting particles by means of the shape of the signal looks very good on the light signal. Indeed it turns out to be much better than the one obtained by the difference in light yield.

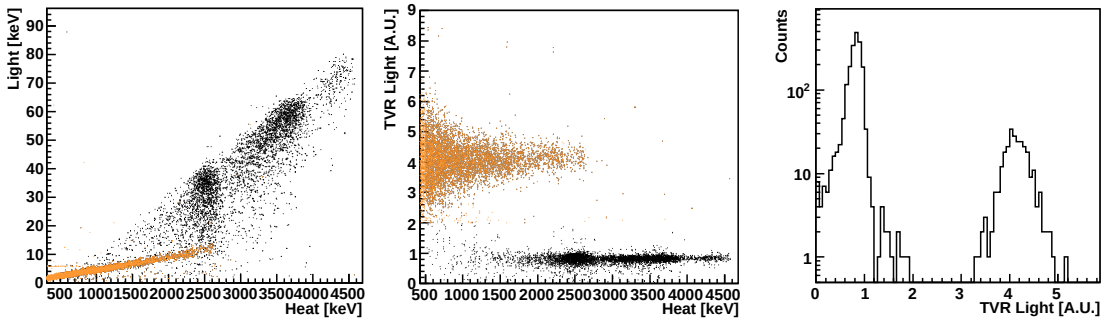

Figure 9.8: ZnSe Large exposed to source B and to a Sm source, both mounted at crystal bottom. Left panel: scatter plot of light vs. heat. Black spots are alpha particles, colored spots beta/gamma's. The distinction is based on a TVR cut applied to light pulses. Central panel: TVR distribution for light pulses vs. the amplitude of the corresponding heat pulse (*Heat*). The cut used to separate alphas from beta/gamma's is defined by the line TVR=2. Right panel: TVR distribution for light pulses between 2400 and 2600 keV.

This was proved in a dedicated run, in optimized measuring conditions, when it was possible to reach a quite high alpha rejection efficiency. The ZnSe Large crystal was mounted with, on its bottom, source B and a ^{147}Sm source. The LD was operated at a slightly higher temperature than usual, in order to have a faster response. The signal sampling was increased to 16384 points on a 4 sec window, to improve the resolution on the signal shape. The result is illustrated in Figure 9.8. The scatter plot (left panel) of light vs. heat shows clearly the alpha and beta bands. The alpha band has a quite important tail towards low light signals and, based on the heat/light ratio, the alpha discrimination looks quite poor. The LD clearly distinguishes alphas from betas on the basis of their pulse shape (central panel), here measured with the TVR parameter (i.e. the least square differences of the filtered signal with respect to the filtered response function, for more details 4.7). The projection of the TVR distribution (right panel) shows how efficient can be this kind of discrimination; for a better visualization of this efficiency all the signals with TVR lower than 2 appear in the scatter plot (left panel) in color. The alpha rejection efficiency was evaluated in the region 2400-2600 keV (the nearest region to the ^{82}Se $\beta\beta$ Q-value and populated enough by both beta/gamma's and alpha's) to be

about D= 15 σ.

The observed difference in pulse shapes open an important possibility for the use of ZnSe bolometers for 0νDBD search: the rejection of alpha particle background on the basis of the pulse shape with the light detector. In this case we would not have the advantages described at the beginning of the chapter because the light detector is still needed. However, while for ZnSe the use of the heat to light ratio seems to provide only a partial discrimination, the use of the pulse shape of light pulses appears much more efficient.

9.7 The energy partition and the PSA

Before concluding this chapter I would like to report on a possible interpretation of the pulse shape discrimination observed in some scintillating bolometers. This interpretation is based on the assumption that the processes of energy release by an interacting particle, of production of scintillation light and phonons and of their collection can not be considered as instantaneous even in slow detectors such as the bolometers. Indeed, it was widely demonstrated that by lowering the temperature the radiative decay time increases significantly. The scintillation decay time for some of the molybdates tested is between hundreds of μs and few ms [131, 132] at few kelvin and then comparable with the rise time of our bolometers of few ms.

I try here to analyze in more detail the production process of phonons and photons in scintillating bolometers. Let us assume that the interaction of a β particle with the crystal produces N_β electron/hole pairs. A fraction of these (ω_β) will recombine through radiative processes while the remaining (1-ω_β) will give rise to the thermal pulse (this holds in the case in which only two channels share the total energy). For an α particle the fraction that will recombine through radiative processes (ω_α) will be lower ($\omega_\alpha < \omega_\beta$) because of saturation effects [97]. In other words, most scintillating centers are occupied and a larger fraction of energy flow through the heat channel.

The time development of the recombination process for the N_α electron/hole pairs produced by an α particle could be then schematized as follow:

$$-\frac{dN_\alpha}{dt} = \lambda_L N_{L_\alpha} + \lambda_H N_{H_\alpha} = \lambda_L \omega_\alpha N_\alpha + \lambda_H (1-\omega_\alpha) N_\alpha \tag{9.4}$$

where λ_L and $N_{L_\alpha} = \omega_\alpha N_\alpha$ are, respectively, the light decay constant and the number of recombination through the light channel while λ_H and $N_{H_\alpha} = (1-\omega_\alpha)N_\alpha$ are the ones for the heat channel. If we define

$$\lambda_c = \lambda_L \omega_\alpha + \lambda_H (1-\omega_\alpha) \tag{9.5}$$

then

$$\begin{aligned} -\tfrac{dN_\alpha}{dt} &= \lambda_c N_\alpha \\ N_\alpha(t) &= N_0 e^{-\lambda_c t} \end{aligned} \tag{9.6}$$

However, in the main crystal, only the heat channel contributes to the signal formation (here I neglect the self-absorption effects since it is plausible that contribute only minimally) then

$$N_{H_\alpha}(t) = (1-\omega_\alpha) N_0 e^{-(\lambda_L \omega_\alpha + \lambda_H(1-\omega_\alpha))t} \tag{9.7}$$

The same can be done for β/γ particles. In this case

$$N_{H_\beta}(t) = (1-\omega_\beta) N_0 e^{-(\lambda_L \omega_\beta + \lambda_H(1-\omega_\beta))t} \tag{9.8}$$

Instead, for the light signal

$$\begin{aligned} N_{L_\alpha}(t) &= \omega_\alpha N_0 e^{-(\lambda_L \omega_\alpha + \lambda_H(1-\omega_\alpha))t} \qquad \text{for } \alpha \text{ particles} \\ N_{L_\beta}(t) &= \omega_\beta N_0 e^{-(\lambda_L \omega_\beta + \lambda_H(1-\omega_\beta))t} \qquad \text{for } \beta \text{ particles} \end{aligned} \tag{9.9}$$

It is then clear from equations 9.7 and 9.8 that the difference between ω_α and ω_β produces not only a different amount of energy flowing in the heat channel but also a different time evolution.

The processes described above relate to the energy subdivision and to the time evolution of the heat and light channels. The heat channel induces the temperature increase of the main crystal while the restoration of the equilibrium temperature is due to the thermal link to the heat bath.

Due to the recent discovery of this feature detailed studies are not yet been made to corroborate this model. Results from a preliminary analysis, carried out by combining the thermal model described in [135] and the energy partition model described above, seem to confirm it. However, a more detailed analysis is still in progress in order to have a quantitative evaluation of it.

Chapter 10

0νDBD experiments with scintillating bolometers

Great efforts have been made and are being made to improve the sensitivity of experiments for 0νDBD study. Of particular interest is the possibility to realize an experiment having a discovery potential in the Inverted Hierarchy region of the neutrino mass. The goal of the so called "second generation" experiments under construction (Chapter 3) is approach the IH region, while considerable R&D is devoted to new techniques which could bring to the full exclusion of the IH mass region.

In this chapter, after a brief reminder of the parameters that determine the sensitivity (for more details see Chapter 3), the sensitivity that could be reached by a $\sim$1 ton experiment with scintillating bolometers will be analyzed. This evaluation will be based on our current knowledge on the background composition in the 0νDBD region, obtained with TeO_2-based experiments and results on background reduction presented in Chapters 8 and 9.

10.1 A strategy for the future: bolometers

Before discussing the achievable sensitivity of an 0νDBD experiment it is useful to recall its definition: the half-life corresponding to the maximum signal that could be hidden by the background fluctuations at a given statistical Confidence Level (C.L.). At 1σ and for 'high' background counting rates it is:

$$S^{0\nu} = \ln 2 \; \epsilon \frac{x \; \eta \; N_A}{A} \sqrt{\frac{M \; T}{B \; \Delta}} \quad (68\% \; C.L.) \tag{10.1}$$

However, current techniques have led to background levels such that "zero background" experiments ($B \cdot M \cdot T \cdot \Delta \simeq 1$) could be performed. In such a case the sensitivity is defined as

$$S_{0B}^{0\nu} = \ln 2 \; \epsilon \frac{x \; \eta \; N_A}{A} \frac{M \; T}{n_L} \tag{10.2}$$

where n_L is a constant depending on the chosen C.L..

In both situations, bolometers play a primary role because, thanks to the wide choice for the absorber material, it is possible to maximize equations 10.1 and 10.2 through the optimization of all its terms. In particular:

- being solid state detectors bolometers allow easy to maximize the detection efficiency (ϵ) and mass (M)
- bolometers allow to search 0νDBD for isotopes with high natural isotopic abundance (as in the case of ^{130}Te for TeO_2) and also to maximize the isotopic abundance through enrichment
- the choice of the absorber material allows to select compounds with low molecular mass (A) and high stoichiometric multiplicity of the element containing the 0νDBD candidate (x)
- the energy resolution is among the best ever measured for massive solid state detectors (i.e. between 5 and 10 keV at 3 MeV)
- the background can be minimized with a proper choice of the isotope and by employing active rejection techniques as those provided by scintillating bolometers

In the following I will analyse the sensitivity issue on the basis of the results on the background and energy resolution obtained with scintillating bolometers and described in previous chapters. In particular I will analyze the sensitivity that could be achieved with a large mass array assembly inside the CUORE experimental set-up.

Among the tested crystals I will consider here three options for the scintillating compound: ZnSe, $ZnMoO_4$and $CdWO_4$. I assume the crystals to be cubic with the same size ($5\times5\times5$ cm^3) of those of the CUORE array and in the same number (988). In Table 10.1 I report the total mass of this scintillating array in the three configurations, the number of nuclei candidate to 0νDBD ($N_{\beta\beta}$) and the number of decays foreseen for a Majorana mass of 50 meV and 20 meV for the more and less favorable nuclear factors (F_N) among those discussed in section 2.1.1. The range 20-50 meV was chosen because it is the range for the inverse hierarchy if the values of oscillation parameters were confirmed [1]. An enrichment level of 90% for the $\beta\beta$ isotope is assumed. This kind of enrichment was already reached for these nuclei by the NEMO collaboration [49].

Isotope	Enrichment	Crystal	Total mass	$N_{\beta\beta}$	N of decays in 5 yr	
			[kg]		$m_{\beta\beta}$=50 meV	$m_{\beta\beta}$=20 meV
^{82}Se	90%	ZnSe	651	2.4×10^{27}	8-56	1-9
^{116}Cd	90%	$CdWO_4$	976	1.5×10^{27}	9-48	1-7
^{100}Mo	90%	$ZnMoO_4$	519	1.2×10^{27}	7-38	1-6
^{130}Te	34%	TeO_2	741	9.5×10^{26}	5-27	1-4

Table 10.1: Experiments characteristics for three different 0νDBD candidates. For each isotope are quoted the type of scintillating crystal, the total mass of a 988 5×5×5 cm^3 crystal array, the number of $\beta\beta$ candidates, the number of decays in 5 years foreseen for the more and the less favorable F_N assuming $m_{\beta\beta}$=50 meV and $m_{\beta\beta}$=20 meV. An enrichment level of 90% is assumed for scintillating bolometer but for TeO_2 crystals (reported here for a comparison) where natural isotopic abundance (a.i.=34%) is assumed.

In the following I will focus one the three parameters (mass M, background B and energy resolution Δ) that could allow to improve the sensitivity, once fixed the compound of the detector. For the live time (T) of the experiment I use what is commonly considered as a "standard" live-time for a 0νDBD experiment (i.e. 5 years). Small differences do not involve a significant change in sensitivity ($S^{0\nu} \propto \sqrt{t}$) and live time much higher than few years are unrealistic.

10.1.1 The background

In studying the background issues for an Experiment able to reach the Inverted Hierarchy of neutrino mass (IHE), I analyze separately three different types of sources:

- near sources, i.e. anything inside the internal Pb shield that will surround, as in CUORE, the array.
- far sources, i.e. those due to radioactive contaminations of the experimental apparatus (mainly the refrigerator and its external shields).
- external sources, i.e. environmental contribution present at the experiment location (Laboratori Nazionali del Gran Sasso) like muons, neutrons and γ rays.

The region of interest (ROI) for the evaluation of the background is few FWHM wide and centered at the 0νDBD Q-value for the three isotopes under discussion. The ROI is therefore located between 2.8 and 3 MeV. When quoting background rates, I assume to operate the detectors in anticoincidence, thus recording only single hit events. All the background levels quoted in the following have been defined with the aid of a dedicated

Monte Carlo simulation based on GEANT4. Except some small geometrical differences, the simulation is the same as that described in detail in Chapters 5 and 6.

For some background sources, simulations have not yet been carried out. In such a case the expected values for CUORE [138] will be reported. This will allows to have a very conservative idea of the expected background levels. Indeed the background expected for CUORE is evaluated in an energy region centered around the Q-value of ^{130}Te at 2528 keV while all the isotopes studied with scintillating bolometers have Q-values higher than 2615 keV and are therefore in a much lower background region.

10.1.2 Near sources

The design for the detector array is assumed to be as much as possible similar to the CUORE one: 19 towers structure based on a copper skeleton that hosts planes of 4 crystals each. In the case of discrimination based on scintillation light, the light detector will be a Ge or a Si hyper-pure wafer collecting the light emitted by 4 crystals in the same plane. The total amount of material involved for the light detector would be so low that its contamination could be considered negligible. Thus the only relevant sources of background, inside the lead shield, are radioactive contaminations of the copper mounting structure and of the scintillating crystals themselves. In both cases not only γ's, but also β's and α's, part-take to the formation of the counting rate in the 0νDBD region.

Crystal bulk contamination

In the case of crystal bulk contaminations the main contribution to the background rate in the region of interest (ROI) comes from the β/γ emissions of the natural chains. Indeed the kinetic energy of α's emitted by U and Th daughters are always far above the ROI. The β emitters that part-take to the background are ^{208}Tl (^{232}Th chain), ^{214}Bi and ^{210}Tl (^{238}U chain). However they could be tagged thanks to delayed coincidence (for a more detailed description see Chapter 3.4.1).

Crystals bulk contaminations that satisfy the background requirements are reported in Table 10.2 together with the width of the delayed coincidence window used for β tagging and with the value of the dead time introduced so far. The contribution to the background due to bulk contaminations is reported in the last column and it has been evaluated with a Monte Carlo simulation based on ZnSe crystals. According to Monte Carlo simulations, the inefficiency introduced by those fraction of events where the α decay occurs near the crystal surface and the α particle escapes the crystal is of about 0.1%. In this case I assume to loose any possibility of delayed coincidence, and I compute background as the sum of the fraction of β events untagged due to the α escapes and the fraction of β events untagged because they are out of the maximum allowed delayed coincidence window.

In the case of $ZnMoO_4$ the higher Q-value would lead the ROI nearer to the end point

source	position	contamination level	notes	background [counts/keV/kg/yr]
U chain	crystals bulk	0.5 mBq/kg	5 τ (0.2% dead time)	$5.8 \cdot 10^{-6}$
Th chain	crystals bulk	0.001 mBq/kg	5 τ (1.8% dead time)	$1.2 \cdot 10^{-5}$
U+Th chains	mounting Cu bulk	CUORE	CUORE Background	$<6 \cdot 10^{-4}$
U+Th chains	crystals surface	Cuoricino/4	99.9% α rejection efficiency	$3 \cdot 10^{-6}$
U+Th chains	mounting Cu surface	Cuoricino/2	99.9% α rejection efficiency	$2 \cdot 10^{-5}$
U+Th chains	experimental setup	CUORE	CUORE Background	$< 10^{-2}$
Gammas	environmental	hall A	CUORE Background	$<4 \cdot 10^{-4}$
Muons	environmental	hall A	CUORE Background (no veto)	$1.04 \cdot 10^{-4}$
Neutrons	environmental	hall A	CUORE Background	$8.6 \cdot 10^{-6}$

Table 10.2: Background projection for a CUORE-like experiment with scintillating bolometer. When 'CUORE Background' is reported in the fourth column this means that values in the fifth column are the ones evaluated for CUORE [138] in the ROI of ^{130}Te. Then, for what concern, isotope with a Q-value higher than 2615 keV the background due to γ particle is order of magnitude lower. More details in the text.

of the ^{210}Tl and ^{208}Tl β spectra, therefore resulting in lower background rates or in less stringent requirements for the bulk contamination. The opposite will be true for $CdWO_4$ that will require slightly better bulk contaminations.

For all the scintillating crystals under consideration, these contamination levels (see Chapter 8) have already been achieved.

In the case of $CdWO_4$ a further bulk contribution to the background rate could come from ^{113}Cd (natural isotopic abundance of 13%). This natural radioactive isotope beta decays with a half-life of $9{\cdot}10^{15}$ yrs. In natural $CdWO_4$ this results in a specific activity of 0.5 Bq/kg. The Q-value of ^{113}Cd is 316 keV, therefore this source does not give direct contributions to background rate in the ROI. However, given its high rate, it can contribute to the ROI through spurious pile-up with high energy γ's. Nonetheless a future 0νDBD experiment based on this compound should use isotopic enrichment to increase the mass of ^{116}Cd. As a result there will be a considerably reduction of the ^{113}Cd content that will significantly reduce the pile-up probability and, moreover, decrease (n,γ) reaction due to ^{113}Cd (see section 10.1.4).

Copper bulk contamination

Copper is the second material present in the cryostat in high mass. In the a CUORE-like structure the copper mass is about 200 kg. The most important contribution to the counting rate in the ROI come from the ^{214}Bi high energy γ lines (the total branching ratio of these γ lines is 0.09%) and from the ^{208}Tl γ's at 583 and 2615 keV that, being emitted in cascade, can sum at energies as high as 3.2 MeV. In any case the selection of a commercial high quality copper, as the one that will be used in CUORE, would be enough to guarantee a negligible contribution from this sources. Indeed the expected background in CUORE is $<6 \cdot 10^{-4}$ counts/keV/kg/yr near 2528 keV. Above the ^{208}Tl line the background is expected to be at least one order of magnitude lower.

Surface contaminations

Two mechanisms work to the reduction of this background: the α rejection based on the scintillation signal or pulse shape analysis and the use of anticoincidences among the detectors of the array. In table 10.3 I report the discrimination level obtained with scintillating crystals under consideration. However, in the following a conservative α rejection efficiency of 99.9% is assumed (i.e. a discrimination factor of 3.3 σ).

In table 10.2 I summarize the background contribution foreseen. For the surface contaminations levels I have scaled the Cuoricino counting rates in the 3-4 MeV region (table 3.4) to take into account the background achievement obtained during CUORE R&D (i.e. a reduction of crystal surface contamination by a factor 4 and a reduction of copper surface contamination by a factor 2) and the different geometry. The γ and β contribution coming

crystal	Discrimination technique	Discrimination level
ZnSe	PSA (light channel)	15 σ
$CdWO_4$	Light Yield	12.6 σ
$ZnMoO_4$	PSA	5.4 σ

Table 10.3: Alpha discrimination level for the scintillating crystals under consideration. The best discrimination technique (Light Yield or PSA) is chosen.

from these surface contaminations result negligible.

10.1.3 Far sources

Outside the internal lead shield background contribution come mainly from the refrigerator and its external lead and neutron shields. In this case only γ contributions from ^{214}Bi and ^{208}Tl have to be considered (since beta's and alpha's are shielded).

Presently we do not have a direct evaluation of the possible contribution due to these sources in the ROI. Such simulations have been done for CUORE and resulted in a upper limit to the rate in the ^{130}Te ROI of 10^{-2} counts/keV/kg/yr. In the case of the experiment here discussed the ROI lies in a region much higher that the one for ^{130}Te and the mechanisms by which ^{214}Bi and ^{208}Tl can contribute to the background are different. In the case of ^{130}Te the rate is dominated by multi-Compton events of the 2615 keV line of ^{208}Tl, while in the case of Se, Cd, and Mo the rate should be dominated by the contemporary interaction of two gamma lines emitted by ^{208}Tl: the 583 keV line and the 2615 keV line. In the case of contamination of the cryostat, they are relatively far from the detectors and therefore the probability that the two gamma interact with the same crystal is very low. We are therefore confident that the background due to this contribution is negligible. However, Monte Carlo simulations are planned to study in detail this contribution.

10.1.4 Environmental background

As discussed in Chapter 3 environmental background in the underground hall A of Laboratori Nazionali del Gran Sasso consists in muons (cosmic rays), neutrons (produced by spontaneous fission, (α,n) processes or induced by cosmic ray muons) and γ rays (environmental radioactivity or induced by cosmic ray muons). For CUORE it is expected a background due to this last source of $<4 \cdot 10^{-4}$ counts/keV/kg/yr. However it must be taken into account that in the case of external γ's the environmental spectrum of hall A is drastically reduced by crossing the 2.615 MeV line of ^{208}Tl (see Figure 3.2). This leads to a completely negligible contribution of environmental γ's in our ROI.

For what concern muons and neutrons the background evaluated for CUORE is, re-

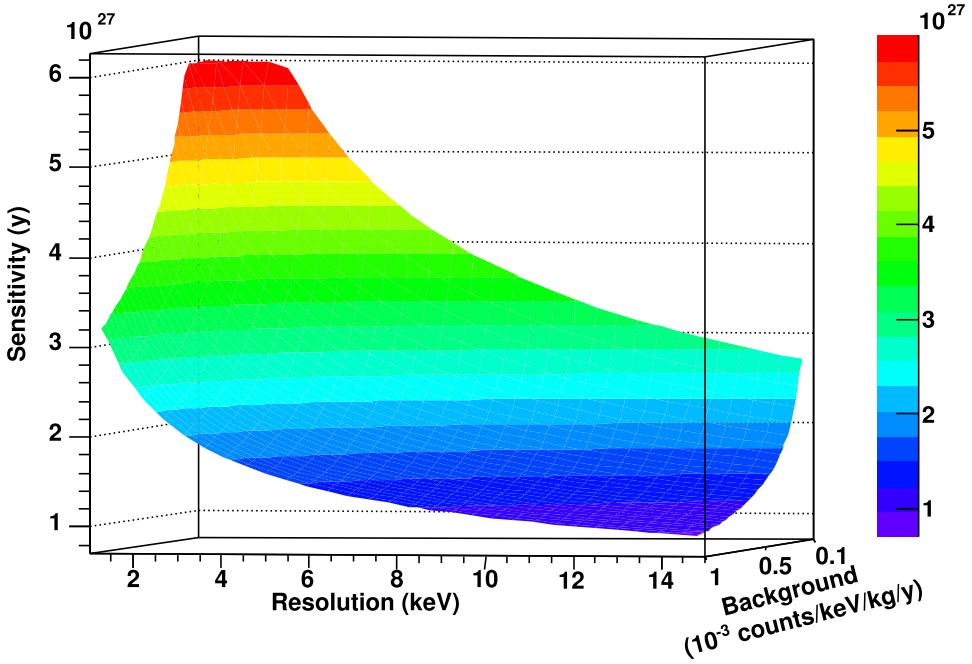

Figure 10.1: 0νDBD sensitivity as a function of energy resolution and background level.

spectively, about $1.04 \cdot 10^{-4}$ and $8.6 \cdot 10^{-6}$ counts/keV/kg/yr [53]. These values can be considered, in first approximation, also for experiments with scintillating bolometers but for $CdWO_4$. Indeed, with such a crystal, particular care must be paid because the high neutron cross section of ^{113}Cd. This source will be studied in the future with Monte Carlo dedicated simulations.

In conclusion, taking into account all the background sources described above, it is probable that with a $\sim$1 ton scintillating bolometers experiment it could be reached a background level of 10^{-3}-10^{-4} counts/keV/kg/y. Although this background level is fairly conservative, lower background levels are useless for $\sim$1 ton experiment with energy resolution of few keV because the 'mass cutoff' of the sensitivity that will be described in section 10.1.6.

10.1.5 Energy resolution

For experiments that search for a well defined peak in the energy spectrum good energy resolution is a very important requirement. Moreover, in experiments for 0νDBD this requirement is much more important because of the 2νDBD.

Both in experiments with a background different from zero (equation 10.1) than in the case of "zero background" experiments the energy resolution play a primary role in

Crystal	FWHM [keV]	FWHM$_\theta$ [keV]
ZnSe	28±1	9.5±0.4
$CdWO_4$	16.5±0.5	6.25±0.22
$ZnMoO_4$	5.6±2	
TeO_2	7±1	

Table 10.4: Energy resolution evaluated at 2615 keV. In the last column are reported values after the axis rotation. The energy resolution for TeO_2 crystals is the one measured by Cuoricino. Resolutions of about 5 keV were however already obtained in hall C tests.

evaluation of the sensitivity. In "zero background" experiments the resolution and the background do not fall within the sensitivity equation 10.2 but from their depend the cutoff between these two types of experiments ($B \cdot M \cdot T \cdot \Delta \simeq 1$).

To stress the importance of the energy resolution in experiments with a background different from zero ($B \cdot M \cdot T \cdot \Delta > 1$) I have reported in Figure 10.1 the sensitivity for 5 years of live time of a CUORE-like experiment realized with ZnSe crystals enriched in ^{82}Se at 90% as a function of the resolution and background. With color are reported iso-sensitivity level.

In table 10.4 are reported resolution values obtained with scintillating bolometers and with TeO_2 crystals. In the last column are reported also the values obtained after the axis rotation procedure (for details see section 8.3.1).

It is interesting to note that in the case of $ZnMoO_4$ and $CdWO_4$ (after axis rotation) it is already possible to reach energy resolution of ∼5 keV while for ZnSe crystals the best energy resolution obtained is 9.5 keV. Moreover the excellent energy resolution of the $ZnMoO_4$ crystals was obtained even without the axis rotation. This is very interesting because the possibility to realize an experiment with discrimination capabilities based on Pulse Shape Analysis. In such a case the light detectors are no more needed and then the axis rotation technique can't be used. The discrimination level of 5.4 σ obtained with the Pulse Shape Analysis and the energy resolution of 5.6±2 keV at 2615 keV make the $ZnMoO_4$ an excellent candidate for 0νDBD searches.

10.1.6 Mass

As mentioned above the mass not only plays an important role in determining the reachable sensitivity but also define the number of observable events. In other words, even if it is possible to realize a 'zero background' experiment with an excellent energy resolution but there is no enough mass, the sensitivity is limited because no events are expected for a live time of few years.

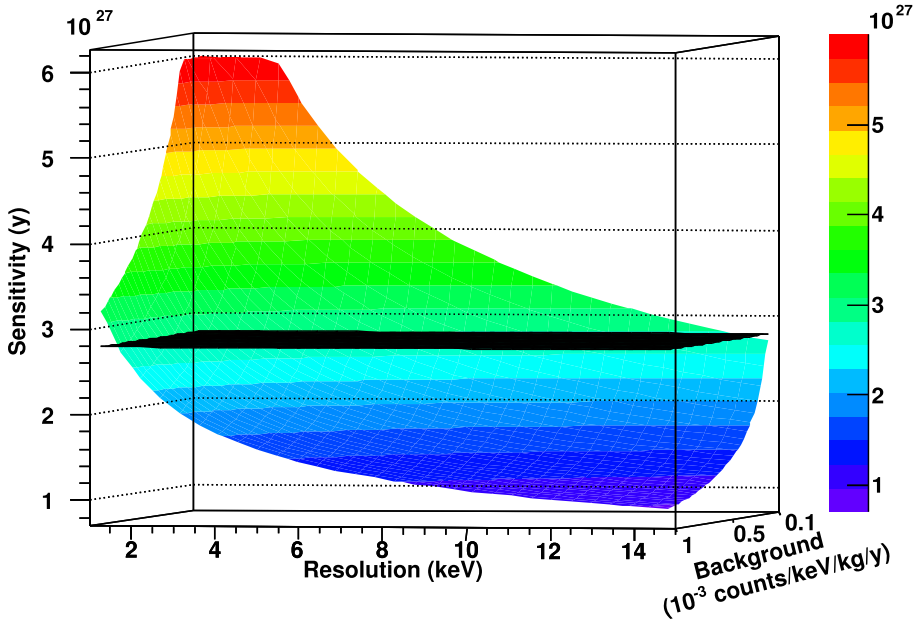

Figure 10.2: 0νDBD sensitivity as a function of energy resolution and background level with sensitivity cut-off due to the number of isotope candidates to 0νDBD, i.e. intersection of equation 10.1 and equation 10.2.

The minimum number of 0νDBD events could then be interpreted as a cutoff of the experimental sensitivity. This cutoff can be evaluated roughly as the intersection of equation 10.1 and equation 10.2.

$$B \cdot \Delta = \frac{n_L^2}{M \cdot T} \tag{10.3}$$

In Figure 10.2 is reported the plot already shown in Figure 10.1 but with the 'mass cutoff' plane evaluated at 90% C.L. (n_L=2.4). I have also reported in Figure 10.3 the projection of the sensitivity on the background-resolution plane. Colors represent iso-sensitivity levels and the black line is the 'mass cutoff'. This means that for a ∼1 ton experiment it is possible to scan only the top-right part of the plot while sensitivities in the bottom-left of the black line are prohibited. Then it is clear that it is useless to plan a CUORE-like experiment with, for example, ZnSe and an energy resolution of 5 keV with a background lower than $2{\cdot}10^{-4}$ counts/keV/kg/yr.

In table 10.5 I have reported the maximum sensitivity reachable by a Cuoricino-like (in the upper part) and by a CUORE-like (in the bottom part) experiment for different crystal. In the fifth column the minimum level of $B \cdot \Delta$ (the black hyperbola in the plot) is reported. In the last column is instead reported the minimum background level for a energy resolution of 5 keV.

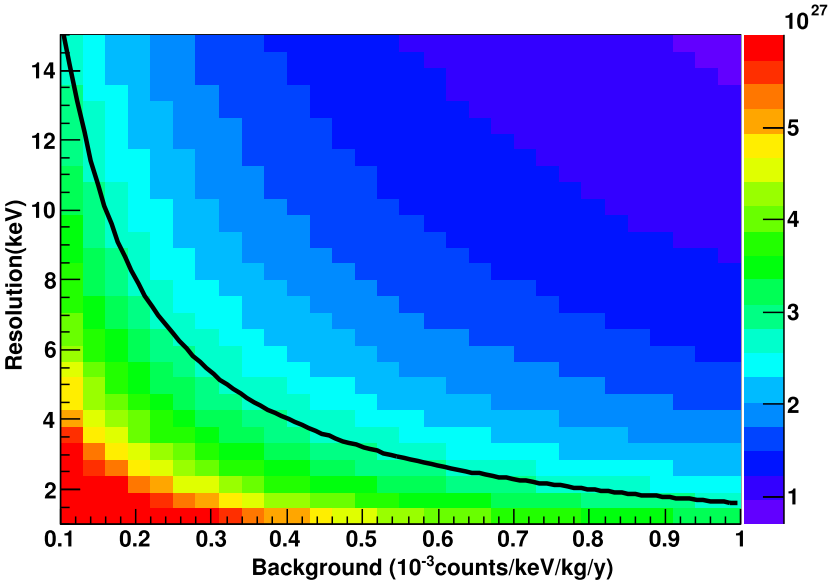

Figure 10.3: Projection of 0νDBD sensitivity.

Crystal	5 year sensitivity [yr]	Neutrino mass [meV]	$B \cdot \Delta$ [counts/kg/yr]	B (for Δ=5keV) [counts/keV/kg/yr]
TeO_2	5.8×10^{25}	65-154	2.9×10^{-2}	5.9×10^{-3}
ZnSe (90%)	1.3×10^{26}	45-122	3.3×10^{-2}	6.6×10^{-3}
$ZnMoO_4$(90%)	7.0×10^{25}	55-129	4.1×10^{-2}	8.2×10^{-3}
$CdWO_4$(90%)	9.3×10^{25}	50-116	2.2×10^{-2}	4.4×10^{-3}
TeO_2	1.2×10^{27}	14-34	1.4×10^{-3}	2.8×10^{-4}
ZnSe (90%)	2.8×10^{27}	10-27	1.6×10^{-3}	3.2×10^{-4}
$ZnMoO_4$(90%)	1.4×10^{27}	12-28	2.0×10^{-3}	4.0×10^{-4}
$CdWO_4$(90%)	1.9×10^{27}	11-26	1.1×10^{-3}	2.1×10^{-4}

Table 10.5: Maximum sensitivity reachable by 0νDBD experiments with 48 and 988 ($5\times5\times5$ cm^3) crystals and limits on B $\cdot$ Δ due to 'mass cutoff'.

Chapter 11

Conclusion

My Ph.D work was focused mainly on the study of the background in bolometric 0νDBD experiments and on the development of techniques to reduce it. The starting point of this work was the information obtained from the Cuoricino experiment and from some dedicated measurements performed with small bolometric arrays. The first step consisted in the use of this information to evaluate - on the basis of a Monte Carlo simulations - the background contributions in the CUORE experiment. An example of this work is the study of the background due to flux of underground muons at LNGS. This study was based on the comparison of Monte Carlo simulations and on a dedicated measurement performed with a muon veto installed above Cuoricino. Thanks to the good agreement between simulation and measurement was possible to estimate the background induced by muons in CUORE.

Although this activity allowed to find a way to optimize the CUORE apparatus in order to reduce to a minimum some of the identified background contributions, one background source resulted almost irreducible. The most likely identification of this source is in the surface contamination of the materials surrounding the bolometers. Such a source could in principle prevent bolometers to be important competitors in the far future with other 0νDBD experiments. Indeed it seems to fix the limit on achievable background to a level of 10^{-2} counts/keV/kg/y. The study of a possible way to get rid of this problem have been the main subject of my work. The solution was indeed found in scintillating bolometer, a novel class of hybrid devices that thanks to the double read out of light and heat allow to recognize the nature of the interacting particles. Since according to our model, most of the irreducible background in pure bolometers comes from degraded alpha particles emitted by the surfaces of the surrounding materials, the possibility to identify the interacting particle is of fundamental importance both for the development of an active technique to

reduce the background in 0νDBD experiments and as a diagnostic method for the study of very low levels of surface contaminations.

For what concerns the application of this technique to the active rejection of background, I have tested different scintillating bolometers candidate to 0νDBD studies. In this thesis I have reported in detail the results from the point of view of the discrimination levels and bolometric performances obtained with some of the tested crystals (ZnSe, $CdWO_4$ and some molybdates). Moreover some interesting aspects of the scintillating bolometer technique were discussed: the light/heat correlation in order to increase the energy resolution, the heat/energy correction and the 'inverse' Quenching Factor for ZnSe crystals just to give some examples.

During these tests I observed the possibility to recognize the interacting particles through the shape of the thermal signal (Pulse Shape Analysis). I then developed dedicated methods for improving the resolving power. This feature is very promising because it allows to obtain the same results of the hybrid detectors on the background reduction, but without requiring a complicated assembly of the experiment. In fact in the case of the double read-out of temperature and scintillation both the light detectors and the reflecting sheet (used to properly collect the scintillation light) are needed in addition to the pure bolometer.

It was demonstrated that discrimination levels better than 5σ can be obtained both with the light/heat and Pulse Shape Analysis. This allows to design 0νDBD experiments based on the bolometric technique able to reduce the background due to surface contamination to negligible levels. Taking into account also all the other possible sources of background it was demonstrated how it is possible to project an experiment able to reach background levels of 10^{-3}-10^{-4} counts/keV/kg/y. When combined with the excellent energy resolution of these detectors, it is possible to plan a $\sim$1-ton experiment able to probe the Inverse Hierarchy of neutrino mass.

Finally, the possibility to use scintillating bolometers as a diagnostic tool for the study of surface contamination was also demonstrated. Conventional techniques are not able to reach the sensitivity levels needed for rare events studies such as CUORE. Then the possibility to have a very sensitive tool to study surface contamination is very appealing.

Appendix

Cryogenic Setup

Cryostats installed in Hall A and Hall C of LNGS are two dilution refrigerator. Their working principle is based on ^{3}He/^{4}He mixture properties. In Figure 11.1 it is possible to observe that, at a temperature T higher than $T_\lambda \simeq$0,87 K the mixture can have properties of fluid or superfluid depending on the temperature and the relative concentration (n_3) of ^{3}He. For $T<T_\lambda$ the mixture separates into two phases, one rich in ^{3}He (concentrated phase) and the other rich in ^{4}He (dilute phase). Since the enthalpy of ^{3}He in the dilute phase is greater than in the concentrated phase, the transition of ^{3}He from the dilute phase to the concentrated one generate refrigeration. The passage of ^{3}He between the two phases can be treated as an ordinary evaporation process in which the liquid phase is the concentrated phase and the vapor is the dilute phase.

To better understand the operation of a dilution refrigerator look at the Figure 11.2. The coldest point of the cryostat, said mixing chamber, is at a temperature of 7-8 mK and inside it the two phases of the mixture coexist. From dilute phase, mixture flows to the distiller (Still) at 600 mK. At this temperature the vapor pressure of ^{3}He is about 1000 times higher than that of ^{4}He, and then from the diluted mixture evaporates practically pure ^{3}He. It is taken away from a pump that is at room temperature to ensure a constant osmotic pressure gradient between the still and the dilute phase in the mixing chamber. The ^{3}He pumped away from the still is returned into the cryostat. It has a first cooling in Main Bath, which contains liquid helium at a temperature of 4.2 K, and then it is condensed in 1KPot held at 1.2 K by pumping on liquid Helium. Going through other stages of thermalization the mixture back to temperatures low enough to be back into the mixing chamber.

To ensure isolation from the outside the apparatus is enclosed in a vacuum chamber, called Outer Vacuum Chamber (OVC). The outer wall is at 300 K, while the inner is maintained at 4K by the presence of liquid ^{4}He contained in an area called Main Bath.

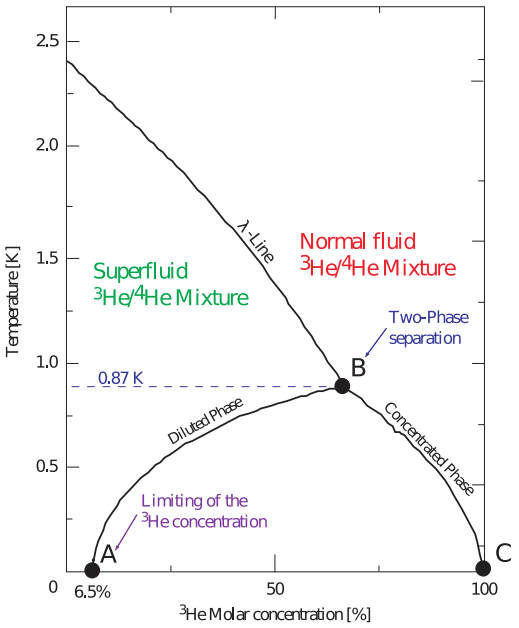

Figure 11.1: Phase diagram of ^{3}He/^{4}He mixture as function of the temperature in saturated vapor pressure. In the coexistence phase there is the separation of two phases, the upper rich on ^{3}He, the lower on ^{4}He.

Inside there is the Inner Vacuum Chamber (IVC), which contains other concentric screens that allow to protect the coldest part of the apparatus by the power input by radiation or by conduction from residual gases.

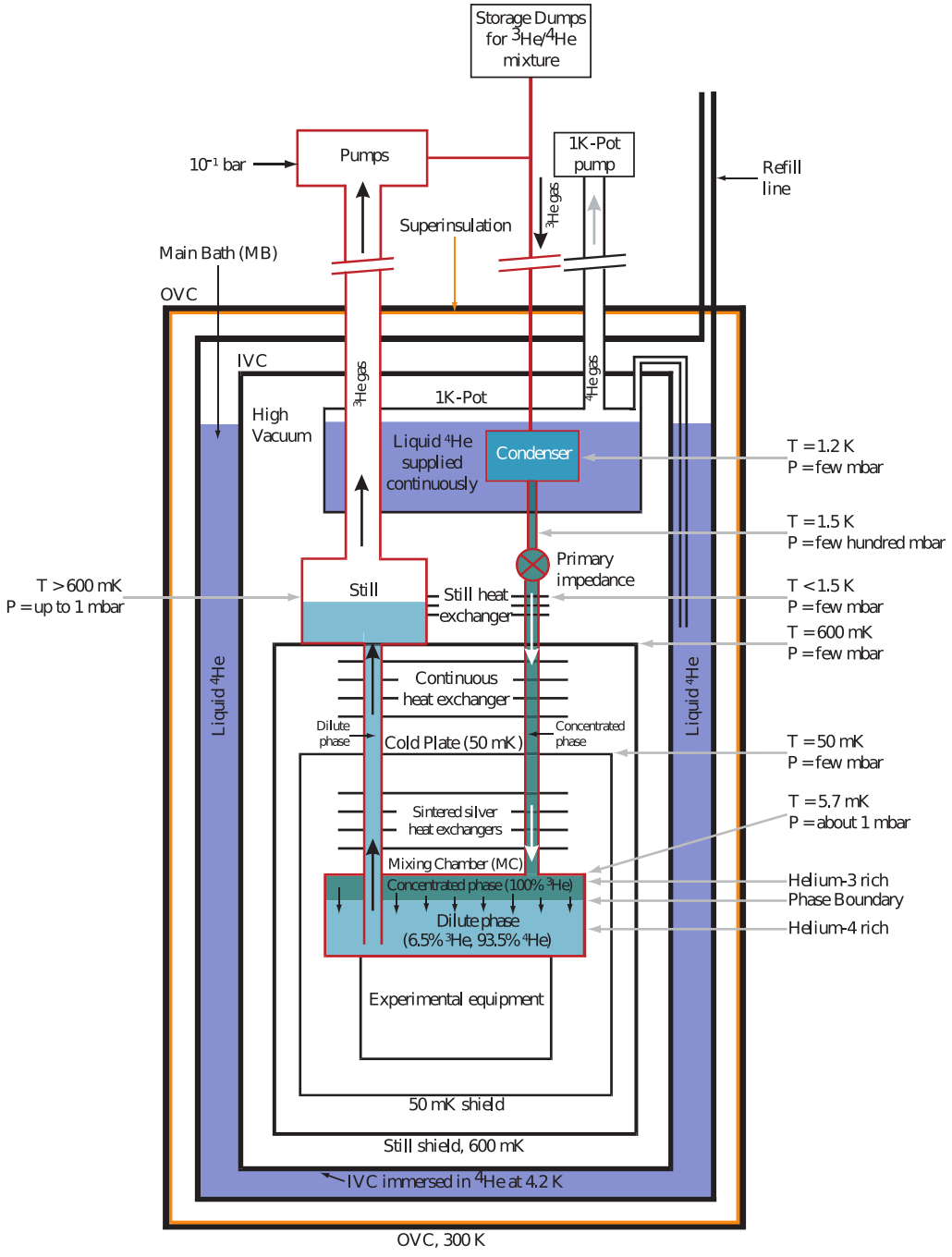

Figure 11.2: Schematic diagram of a conventional ^{3}He/^{4}He dilution refrigerator.

Bibliography

[1] A. Strumia, F. Vissani, hep-ph/0606054

[2] E. Fermi, Zeitschrift fur Physik A Hadrons and Nuclei **88** (1935) 161

[3] C. L. Cowan, F. Reines *et al.*, Science **124** (1956) 103

[4] L. M. Lederman, M. Schwartz *et al.*, Physical Review Letters **9** (1962) 36

[5] K. Kodama *et al.*, Physics Letters B **504** (2001) 218

[6] B. T. Cleveland *et al.*, Astrophys. J. **496** (1998) 505

[7] Z. Maki, M. Nakagawa, S. Sakata, Prog. Theor. Phys. **28** (1962) 870

[8] L.-L. Chau, W.-Y. Keung, Phys. Rev. Lett. **53**, 1802 (1984)

[9] Kamiokande-II, K. S. Hirata et al., Phys. Lett. B **205** (1988) 416

[10] IMB, R. M. Bioneta et al., Phys. Rev. D **38** (1988) 768

[11] Ch. Kraus. Eur. Phys. J. C **40** (2005) 447

[12] V. M. Lobashev. Nucl. Phys. B (Proc Suppl.) **9**1 (2001) 280

[13] KATRIN Design Report (2004) http://www.ik.fzk.de/katrin

[14] M. Sisti et al. NIM A **520** (2004) 125

[15] C. Arnaboldi et al. Phys. Rev. Lett. **91** (2003) 161802

[16] R. N. Mohapatra and G. Senjanovic, Review D **23** (1981) 165

[17] S.T..Petcov, H. Sugiyama, Y. Takanishi, arXiv:hep-ph/0904.0759v1

[18] E. Fiorini *et al.* Physics Letters B **25** (1967) 602

[19] M. Goeppert-Mayer, Phys. Rev. **48** (1935) 512

[20] J. Basdevant, J. Rich, and M. Michael, Fundamentals in Nuclear Physics: From Nuclear Structure to Cosmology. Springer, 2005

[21] S. R. Elliott, A. A. Hahn, and M. K. Moe, Physical Review Letter 59 (1987) 20202023

[22] Y. G. Zdesenko, F. A. Danevich, and V. I. Tretyak, Physics Letters B 456 (2002) 206215

[23] H. Ejiri, Progress in Particle and Nuclear Physics 48 (2002) 185200

[24] W. Furry, Phys. Rev. 56 (1939) 1184

[25] A. Strumia and F. Vissani, arxiv:hep-ph/0606054v3 (2010)

[26] F. Simkovic *et al.*, Phys. Rev. C 77 (2008) 045503

[27] O. Civitarese *et al.*, JoP:Conference series 173 (2009) 012012

[28] J. Menendez *et al.*, NPA 818 (2009) 139

[29] J. Barea and F. Iachello, Phys. Rev. C 79 (2009) 044301

[30] S. Cowell, Phys. Rev. C 73 (2006) 028501

[31] C.E. Aalseth *et al.*, Phys. Rev. D 65 (2002) 092007.

[32] H. V. Klapdor-Kleingrothaus *et al.*, Eur. Phys. J. A 12 (2001) 147

[33] H. V. Klapdor-Kleingrothaus *et al.*, Phys. Lett. B 586 (2004) 198

[34] H. V. Klapdor-Kleingrothaus *et al.*, Mod. Phys. Lett. A 21 (2006) 1547

[35] C. E. Aalseth *et al.*, Mod. Phys. Lett. A 17 (2002) 1475
F. Feruglio, A. Strumia and F. Vissani, Nucl. Phys. B 637 (2002) 345, and Addendum, Nucl. Phys. B 659 (2003) 359

[36] C. Arnaboldi *et al.*, Phys. Rev. C 78 (2008) 035502

[37] R. Arnold *et al.*, Phys. Rev. Lett. 95 (2005) 182302

[38] I. Abt *et al.*. Eur. Phys. J. C 52 (2007) 19

[39] C. E. Aalseth *et al.*, Nucl. Phys. B (Proc. Suppl.) 138 (2005) 217

[40] C. Arnaboldi *et al.*, NIM A 518 (2004) 775

[41] C.Arnaboldi *et al.*, Phys. Lett. B 557 (2003) 167

[42] A. Alessandrello *et al.*, Nucl. Phys. B 28 (1992) 233

[43] Research Proposal (B1) LUCIFER 2009 - ERC-2009-AdG 247115

[44] EXO collaboration, http://www-project.slac.stanford.edu/exo

[45] P. Novella, NEXT collaboration, J. Phys.:Conf. Ser. 203 (2010) 012068

[46] I. Ogawa *et al.*, J. Phys.:Conf. Ser. 203 (2010) 012073

[47] SNO+ collaboration, http://snoplus.phy.queensu.ca/

[48] M. Koga http://indico.cern.ch/conferenceOtherViews.py?view=standard&confId=66513

[49] F. Mauger, NEMO3 collaboration, J. Phys.:Conf. Ser. 203 (2010) 012065

[50] R. N. Mohapatra and P. B. Pal, 'Massive Neutrinos in Physics and Astrophysics' World Scientific, (2004)

[51] S. R. Elliott and P. Vogel, Ann. Rev. Nucl. Part. Sci. 52 (2002) 115

[52] C. Arnaboldi *et al.*, Journal of Crystal Growth 312 (2010) 2999

[53] C. Bucci *et al.*, Eur. Phys. J. A, 41 (2009) 155

[54] L. Pandola *et al.*, Nucl. Instrum. Meth. A 570 (2007) 149

[55] F. Arneodo *et al.*, Il Nuovo Cim. 112A (1999) 819

[56] P. Belli *et al.*, Il Nuovo Cim. 101A (1989) 959

[57] H. Wulandari *et al.*, Astropart. Phys. 22 (2004) 313

[58] H. Wulandari *et al.*, ArXiv:hep-ex/0401032

[59] D. Mei and A. Hime, Phys. Rev. D 73 (2006) 053004

[60] M. Aglietta *et al.*, Phys. Rev. D 58 (1998) 092005

[61] MACRO Coll., M. Ambrosio *et al.*, Astropart.Phys. 19 (2003) 313

[62] MACRO Coll., M. Ambrosio *et al.*, Phys. Rev. D 52 (1995) 3793

[63] MACRO Coll., S. Ahlen *et al.*, Astrophys. J. 412 (1993) 412

[64] S. Simon, Nature 135 (1935) 763

[65] D.H. Andrews *et al.*, Phys. Rev. 76 (1949) 154

[66] E. Fiorini and T. O. Niinikoski, Nucl. Instr. Meth. A224 (1984) 83

[67] E. E. Haller *et al.*, 'Neutron transmutation doping of semiconducting materials' edited by R. D. Larrabee (Plenum Press, 1984) 21

[68] N. F. Mott and J. H. Davies, Philosophical Magazine B 42 (1980) 845

[69] G. Hilton *et al.*, IEEE Trans. Appl. Supercond. 11 (2001) 739

[70] C. Arnaboldi *et al.*, IEEE Transaction on Nuclear Science 49 (2002) 2440
C. Arnaboldi *et al.*, Nucl. Instr. and Meth. A 559 (2006) 826
C. Arnaboldi *et al.*, Nucl. Instr. and Meth. A 520 (2004) 578

[71] C. Arnaboldi *et al.*, Nucl. Instrum. Meth. A 617 (2010) 327

[72] E. Gatti and P.F. Manfredi, Rivista del Nuovo Cimento 9 (1986) 1

[73] A. Alessandrello *et al.* Nucl. Instr. and Meth. A 412 (1998) 454

[74] E. Andreotti *et al.*, submitted to Astroparticle Physics, arxiv:1012.3266

[75] M. Pavan *et al.*, Eur. Phys. J. A 41 (2006) 155

[76] M. Redshaw *et al.*, Phys. Rev. Lett. 102 (2009) 212502

[77] A. Alessandrello *et al.*, Phys. Lett. B 433 (1998) 156

[78] E. Andreotti *et al.*, Astroparticle Physics 34 (2010) 18

[79] S. Agostinelli *et al.*, Nucl. Instrum. Methods Phys. Res. A 506 (2003) 250

[80] C. Amsler *et al.*, Phys. Lett. B 667 (2008) 1

[81] G. J. Feldman, R. D. Cousins, Phys. Rev. D 57 (1998) 3873

[82] CUORE Collaboration, LNGS Annual Report 2009

[83] C. Arnaboldi *et al.*, Journal of Crystal Growth 312 (2010), 2999

[84] H.M. Araujo and V.A.Kudryavtsev, Nucl. Instrum. Meth. A 545 (2005) 398

[85] V.A.Kudryavtsev *et al.*, Eur. Phys. J. A 36 (2008) 171

[86] C. Bobin *et al.*, Nucl. Instr. Meth. A 386 (1994) 453

[87] G. Angloher *et al.*, Astropart. Phys. 23 (2005) 325

[88] S. Cebrian *et al.*, Phys. Lett. B 563 (2003) 48

[89] S. Pirro, *et al.*, Nucl. Instr. and Meth. A 559 (2006) 361

[90] F.A. Danivich, *et al.*, Phys. Rev. C 68 (2003) 035501

[91] G. Bellini *et al.*, Phys. Lett. B 493 (2000) 216

[92] L. Gironi *et al.*, Opt. Mat. 31 2009 1388

[93] C. Arnaboldi *et al.*, Astrop. Phys. 34 (2010) 143

[94] E. Conti *et al.*, Phys Rev. B 68 (2003) 054201

[95] J. Amare *et al.*, Appl. Phys. Lett. 87 (2005) 264102

[96] V.I. Tretyak, Astropart. Phys. 33 (2010) 40

[97] J.B. Birks, Proc. Phys. Soc. A 64 (1951) 874

[98] C. Cozzini *et al.*, Phys Rev. C 70 (2004) 064606

[99] A. Alessandrello *et al.*,Phys Lett B 408 (1997) 465

[100] N. Coron *et al.*, Phys Lett B 659 (2008) 113

[101] A. Benoit *et al.*, Nucl. Instr. and Meth. A 577 (2007) 558

[102] S. Pirro *et al.*, Physics of Atomic Nuclei 69 (2006) 2109

[103] G. Audi and A. H. Wapstra, Nucl. Phys. A 729 (2003) 337

[104] R. Arnold *et al.*, Phys. Rev. Let. 95 (2005) 182302

[105] R. Arnold *et al.*, Nucl. Instr. Meth. A 536 (2005) 79

[106] I. Dafinei *et al.*, IEE Trans. Nucl. Sc. 57 (2010) 1

[107] O. Madelung, U. Rassler, M. Schulz, - The Landolt-Brnstein Database (http://www.springermaterials.com). DOI: 10.1007/10681719_480;

[108] E. Krause *et al.*, J. Crystal Growth 138 (1994) 75

[109] H.Krauss, V. B. Mikhailik and D. Wahl, Rad. Meas. 42 (2007) 921

[110] C. Arnaboldi *et al.*, Astrop. Phys. 34 (2011) 344

[111] L. Gironi *et al.*, Journal of Instrumentation 5 (2010) P11007

[112] S.H. Moseley, J.C. Mather, D. McCammon, J. Appl. Phys. 56 (1984) 1257

[113] E.V. Sysoeva *et al.*, Nucl. Instr. and Meth. A 414 (1997) 274

[114] W. Klamra *et al.*, Nucl. Instr. and Meth. A 484 (2002) 327

[115] F. A. Danevich *et al.*, Phys. Rev. C 67 (2003) 014310

[116] V.B.Mikhailik and H. Kraus, J. Phys. D: Appl. Phys. 39 (2006) 1181

[117] G. Audi, A.H. Wapstra, C. Thibault, Nucl. Phys. A 729 (2003) 337

[118] J.K. Bohlke *et al.*, J. Phys. Chem. Ref. Data 34 (2005) 57

[119] A. Senyshyn *et al.*, Phys. Rev. B 73 (2006) 014104

[120] H. J. Kim *et al.*, IEEE Trans. Nucl. Sci 57 (2010) 1475

[121] L.I. Ivleva *et al.*, Crystallography Reports 53 (2008) 1087

[122] L.L. Nagornaya *et al.*, IEEE Trans. Nucl. Sci. 56 (2009) 2513

[123] D.N. Grigoriev *et al.*, Nucl. Instr. and Meth. A (2010), doi:10.1016/j.nima.2010.07.067

[124] Tan *et al.*, Nuclear Physics A, 388 (1982) 498

[125] O. A. P. Tavares, E. L. Medeiros and M. L. Terranova, J.Phys. G: Nucl. Part. Phys. 31 (2005)

[126] P. de Marcillac *et al.*, Nature 422 (2003) 876

[127] H. Kraus *et al.*, Nuclear Physics B - Proceedings Supplements 173 (2007) 168

[128] CANBERRA (http://www.canberra.com) and ORTEC (http://www.ortec-online.com) catalogs for the specifics of commercial low background Si surface barrier alpha spectrometers

[129] A.N. Annenkov *et al.*, Nucl. Instr. Meth. A 584 (2008) 334

[130] H. Kraus *et al.*, Radiation Measurements 42 (2007) 921

[131] V. B. Mikhailik *et al.*, Journal of Phys.: Condens. Matter 17 (2005) 7209

[132] V. B. Mikhailik and H. Kraus, Phys. Status Solidi B (2010) 1

[133] J. B. Birks, The Theory and Practice of Scintillating Counting, Pergamon Press (1964)

[134] G. Bizarri, Journal of Crystal Growth 312, 8 (2010)

[135] M. Vignati, Model of the Response Function of CUORE Bolometers, PhD thesis

[136] A. Alessandrello *et al.*, Nucl. Instr. and Meth. A 409 (1998) 451

[137] N. Coron *et al.*, Nucl. Instr. and Meth. A 520 (2004) 159

[138] S.Capelli *et al.*, Beyond 2010 Conference Proceedings (2010)